ABSTRACT

A Search for Eclipsing Binaries in Galactic Globular Clusters

by
Kaspar von Braun

Chair: Mario L. Mateo

We report on the discovery and analysis of short-period (0.1 days $< P <$ 5 days), photometrically varying binary stars around and below the main-sequence turnoff of the globular clusters (GCs) NGC 3201, M10, & M12. These eclipsing binaries (EBs) may be used to determine directly the distances to GCs and constrain the Population II stellar main-sequence masses. During our search for binaries, we discovered the signature of differential reddening across the cluster fields which was especially strong for NGC 3201 and M10. We correct for this differential reddening by calculating average E_{V-I} values for stars in small subregions of the field with respect to a fiducial region, which significantly improves the appearance of the GC color-magnitude diagrams (CMDs). The reddening zero point to be added to the differential value is determined by isochrone fitting. The results of our differential dereddening are presented in the form of high-resolution extinction maps. Our search for EBs returned 14 variable stars (11 EBs) in the field of NGC 3201, 3 variables (1 EB) in M10, and 2 EBs in M12. Of these variables, only one EB in NGC 3201 (a blue straggler W Ursa Majoris contact system) is a definite GC-member, based

on spectroscopic observations. Another W UMa contact EB in M12 is most likely a member of M12, based on its location in the color-magnitude diagram (CMD) and its empirically calculated absolute magnitude. We present the phased lightcurves for all variables, estimate their distances and GC membership, and show their locations in the GC fields and CMDs, as well as the spectra of the NGC 3201 EBs. Finally, we discuss the implications of our results and outline future work.

A SEARCH FOR ECLIPSING BINARIES IN GALACTIC GLOBULAR CLUSTERS

by

Kaspar von Braun

A dissertation submitted in partial fulfillment
of the requirements for the degree of
Doctor of Philosophy
(Astronomy & Astrophysics)
in The University of Michigan
2002

Doctoral Committee:

Associate Professor Mario L. Mateo, Chair
Associate Professor Gary M. Bernstein
Dr. Patrick O. Seitzer
Associate Professor Fred C. Adams

Dedicated to my father Christoph von Braun, without whose love, support, and *interest* I probably would not have embarked on these studies in the first place, and to my mother Andrea von Braun, to whom I would have so much loved to show this work.

ACKNOWLEDGEMENTS

During the course of my career as a student in physics and astronomy, I have been deeply personally affected and influenced by countless people to whom I more grateful and indebted than I could ever hope to express in even 1000 pages. Since this dissertation is an academic work, however, I shall focus on the individuals with whom I had the privilege to work, cooperate and collaborate academically.

First and foremost, I would like to thank my advisor, Mario Mateo, for countless hours of advice and mentorship during my time at the University of Michigan. Without his insight and help, I would not have been able to produce the work presented here. I would furthermore like to express my gratitude to the other members of my committee, Gary Bernstein, Pat Seitzer, and Fred Adams, for their comments and suggestions about my dissertation.

Secondly, I would like to acknowledge the faculty of the Michigan Astronomy Department, past and present, particularly Guy Worthey. I am furthermore indebted to the great group of postdocs we have had over the years, in particular Phil Fischer, Chris Smith, Robbie Dohm-Palmer, Pat Knezek, and Andy Layden. Finally, I would express my gratitude to the staff at the Department, especially Dianna Smith, Tina Drews-Cole-Arabadjis, Carolyn Wery, and Angela Peters.

Most of all, however, I would like to thank my fellow graduate students, past and present, for the innumerable hours, days, nights, weeks, and months of comraderie, support, advice, counseling, and a wonderful time at Michigan. In particular, I would

like to thank John Arabadjis, Joel Parriott, Mike Jarvis, Patricia Hanlan, Jessica Krick, Todd Rigg, Jose Salgado, Carrie Swift, Deano Smith, Alex Athey, Eric Miller, Lynne Allen, Louis Strolger, Denise Hurley-Keller, and especially Kristin Chiboucas, for the help, support, advice, and insights you have given me during the past eight years.

It is out of gratitude and in dedication to the people mentioned above that is not "I", but "we" who present the work in this dissertation.

TABLE OF CONTENTS

LIST OF FIGURES

Figure

LIST OF TABLES

Table

CHAPTER I

Introduction

Among the numerous directions of research conducted in the field of modern astronomy, a substantial amount of time and money is dedicated to the determination of the Hubble constant H_0, the mass density parameter Ω_0, and the cosmological constant λ. The knowledge of these three cosmological parameters is vital to obtaining a value for the expansion age of the universe, one of the most sought-after numbers in astronomy. An independent lower limit to this expansion age can be provided by calculating the ages of the oldest stars in the Milky Way: the metal-poorest stars in the Milky Way halo.

1.1 Why Study Eclipsing Binary Stars in Globular Clusters?

Old globular clusters (GCs) in our Galaxy, which harbor some of these metal-poor stars of the Milky Way halo, represent the oldest known stellar associations and are thought to have formed in the very early stages of galaxy formation (Rosenberg 2000; Mould 2000), at a time $t_{formation} < 10^9$ years after the Big Bang. The discrepancy between calculated ages of the oldest GCs and the expansion age of the universe has recently become smaller. The "traditional" age of GCs of $\sim 15+$ Gyrs (Vandenberg et al. 1996; Sarajedini et al. 1997) has been revised to slightly younger ages (11-14 Gyrs) due to the improved precision in the direct determinations of stellar distances

from the Hipparcos mission (see Freedman 2000, and references therein). In parallel, the expansion age of the universe was revised upwards from $\sim$ 10 Gyrs to 11-12 Gyrs by reducing Ω_0 from 1.0 to about 0.3, and again increased by assuming a non-zero Ω_λ (vacuum energy density) to 13-14 Gyrs for $\Omega_\lambda \sim 0.7$ and $H_0 = 70$ km/s/Mpc (Mould 2000; Freedman 2000; Gnedin et al. 2001; Tammann et al. 2001). Thus, the two independently calculated values seem to agree to within error estimates, which, for GC ages, remain large (on the order of a few Gyrs, see for example Jimenez 1999; Mould 2000; Fukugita 2000; Gnedin et al. 2001; Tammann et al. 2001).

The true measure of a GC age is its intrinsic turnoff luminosity. Uncertainties in the observation of this quantity are produced by, e.g., uncertainties in the GC chemical composition (their metallicity [Fe/H] and the scaling of other metals with Fe), photometric errors in the determination of the magnitudes of main-sequence turnoff stars, reddening, the existence of a binary sequence in the color-magnitude diagram (CMD), and others. Stellar models are forced to incorporate these uncertainties into their calculations of the stellar masses and subsequent age estimates for stars. At the same time, these highly complex models must pay careful attention to countless details. Stellar rotation and magnetic fields are rarely included. Primary sources of uncertainties include mass loss, convection, opacities, and nuclear reaction rates (Vandenberg et al. 1996). Binary stars offer a unique tool to provide fundamental checks to these important stellar models as we describe below.

One of the primary goals of studying eclipsing binary stars in GCs is to constrain or even directly calculate the masses of the binary components. Using a combination of spectroscopic and photometric data, their binary nature can be exploited to return the present-day masses of the individual components. The present-day masses can be related to zero-age masses by either assuming a history of mass transfer between

the components, or by detecting a detached binary system without mass transfer. This calculation provides an estimate for stellar mass, the most critical parameter in any stellar model and thus stellar age estimate. These binary system component zero-age masses therefore constitute a vital, independent check of stellar models at low metallicities.

A second goal of the search for eclipsing binary stars in globular clusters is a *direct* estimate of the distance to the parent globular cluster, that is, without any calibration by other methods, as described below. Directly determined distances to clusters can aid in the calibration of the astronomical distance ladder. One well-known method to directly determine distances is trigonometric parallax which provides ground-based distances of up to 50 pc and Hipparcos-based parallax values of around 500 pc (Fukugita 2000). Based on these distances, other methods such as the Cepheid (Pop I) or RR Lyrae (Pop II) period-luminosity-metallicity relation can be calibrated and used for extragalactic distance determinations.[1] Typical GCs are a good order of magnitude more distant ($d \sim 5$ kpc or more). Directly determined distances to these clusters would significantly reduce the uncertainties in the calibration of the RR Lyrae M_V-[Fe/H] relation and, subsequently, the errors in methods based on RR Lyraes, such as the Tully-Fisher Relation, Surface Brightness Fluctuation Method, and others.

1.2 Using Binary Stars as Tools

Variable stars have historically served as important tools and "laboratories" in our understanding of star formation, the formation of stellar clusters, the calibration of distance determination methods, and a variety of other areas. As described above, in

[1]Since the dependence of luminosity of RR Lyraes upon period is essentially flat, more recently the relation $M_V(RR) = \alpha + \beta$[Fe/H] has been used for distance determinations to RR Lyrae stars and GCs (Sarajedini et al. 1997; Chaboyer 1999).

particular the study of eclipsing binary stars (EBs) in a globular cluster can provide a method to obtain a value for the cluster's distance and a constraint concerning turnoff masses of the GC stars (see, e.g., Paczyński 1996).

1.2.1 Number Statistics

Simply detecting EBs in the fields of GCs and confirming their cluster membership is a straightforward – though data-intensive – task. Such systems expand the relatively meager sample of EBs which are currently confirmed GC members (see for example Mateo 1996; McVean et al. 1997; Rubenstein 1997; Rucinski 2000; Clement et al. 2001, and references therein). A statistical evaluation of the number of known member EBs in GCs can help in the determination of quantities such as the binary frequency in GCs as a parameter in the study of dynamical evolution of GCs (Hut et al. 1992).

Member stars of the clusters interact with each other, primarily toward the core of the GC where the stellar density is much higher than in the GC halo. Due to consequent redistribution of stellar kinetic energies and orbits, the core stars gradually diffuse into the halo which, as a result, grows in size. At the same time, the cluster core itself shrinks, and its density will theoretically reach infinitely high values in a finite period of time (10-20 t_{relax}, according to simulations, see Binney & Tremaine 1987), a phenomenon known as core collapse. Binary stars will most likely be located toward the GC center due to the fact that a) they are more likely to form in regions of high stellar density, and b) they will sink toward the core due to their high masses after a few cluster relaxation times. Since the binding energy of one individual hard binary[2] can be as high as a few to ten percent of the binding energy

[2]Hard binaries are systems whose binding energies are higher than the kinetic energies of the system itself and of the field star with which it might interact. Consequently, hard binaries tend to not be disrupted by encounters with other stars, but actually turn part of their kinetic energy into additional binding energy of the system.

of the entire GC, they may act as an energy source (similar to the nuclear reaction inside the centers of stars) to halt core collapse. A binary fraction as low as 10% in the cluster core will suffice to cool the the central region of the GC by reversing the outward flow of energy toward the halo (Binney & Tremaine 1987; Hut et al. 1992) and arrest core collapse.

An additional use of simply detecting member-EBs in GC lies in the calibration of methods such as the calculation of the absolute magnitudes of and corresponding distances to W Ursa Majoris-type contact binary systems (Rucinski 1994, 1995, 2000, see also Chapters IV and V).

Moreover, the detection of blue straggler (BS) binary systems can shed light on the binary frequency among this subclass of stars, which, in turn, could help understand their formation and evolution. Some hypotheses for formation of blue stragglers are that they have formed by collisions between single stars, coalescence of binary systems, and/or interactions between binary systems. Getting a handle on the frequency of binary blue stragglers in a certain GC would therefore present a tool for probing into the dynamical past and even the star formation history of the GC itself (see for example Leonard & Linnell 1992; Hut 1993; Livio 1993; Sills & Bailyn 1999; Sills et al. 2000).

1.2.2 Direct Distance Determination

The simultaneous analysis of photometric and spectroscopic data for any individual EB systems can provide a direct estimate of the distance to the system (Andersen 1991; Paczyński 1996), and thus, if the EB is a GC member, to the GC itself. Since binary systems in GCs are too far away to be spatially resolved into two stars, the observables are fit to models of the photometric lightcurve (a plot of brightness vs phase of the data folded by the correct binary period; see Figs. 1.1 and 1.2) and the

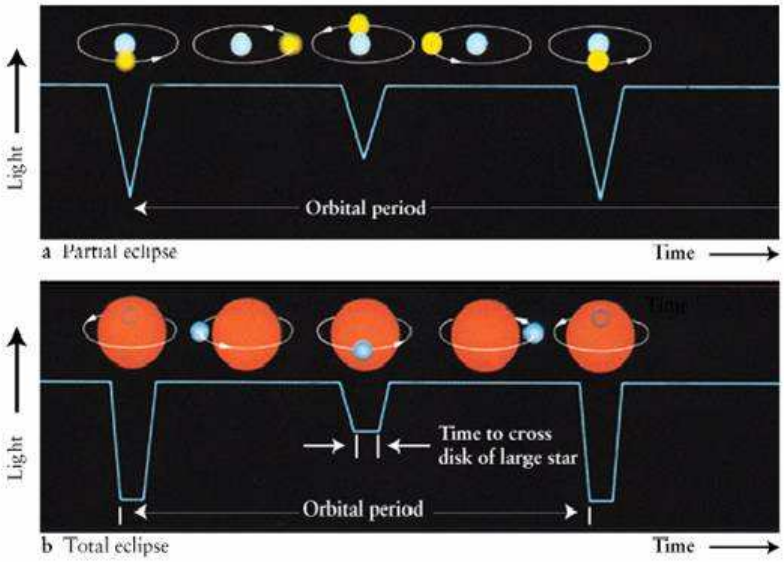

Figure 1.1 This figure, taken from Kaufmann & Freedman (1999) shows some photometric lightcurves of binary stars. In particular, it shows the shape of a lightcurve resulting from a partial eclipse – note the sharp minima, and an example of a total eclipse – note the periods of constant minimum light whose durations give insight into the relative sizes of the two stars in the system.

spectroscopic radial velocity curve (radial velocity vs phase; see Figure 1.3). The models are complex as they need to take into account (Kallrath & Milone 1999) the following aspects:

- System geometry: contact vs. detached system, angle of inclination, eccentricity of the orbits, shapes and sizes of the stars, etc.
- Stellar radiative properties: limb darkening, properties of stellar atmospheres, surface reflections, etc.
- Additional perturbations: star spots, surface activities, stellar winds, additional unresolved companion ("third light"), etc.

From the fit to the photometric lightcurve, one may constrain the period of the system, its inclination angle (from the eclipse depth), the orbital eccentricity (from

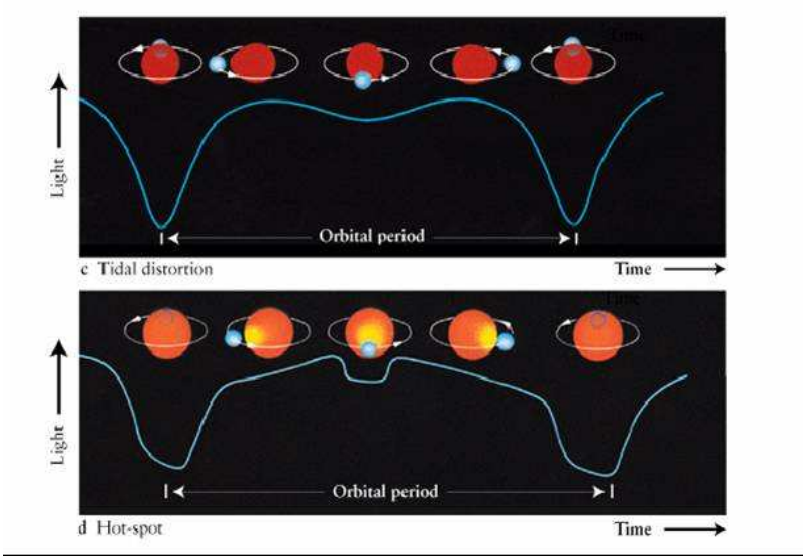

Figure 1.2 This figure, taken from Kaufmann & Freedman (1999) shows some photometric lightcurves of binary stars. Displayed are the effects due to tidal distortion of one of the components, and the effects of a so-called "hot spot" – the reflection of the hotter star (higher surface brightness) on the surface of the cooler star.

the phase angles of the eclipses), and the relative stellar radii (from the duration of the eclipses). See Figures 1.1 and 1.2 for some idealized examples of photometric lightcurves. An additional radial velocity curve, such as the ones shown in Figure 1.3, provides independent checks for the period and eccentricity of the system, and returns the velocity amplitudes K_1 and K_2 for the two components. Given these velocity amplitudes, the period, and the inclination angle, it is possible to obtain the linear sizes of the orbits and the stellar radii. Finally, the knowledge of the surface temperature and the observed flux provides a value for the distance to the system via the Stefan-Boltzmann Law and the inverse-square law:

$$d = R T^2 \sqrt{\frac{\sigma}{f}}, \tag{1.1}$$

where R is the linear radius of the star, σ is the Stefan-Boltzmann constant, f the observed flux (corrected for reddening), and T is the surface temperature of the star.

This surface temperature may obviously not be measured directly, but can be calculated from the intrinsic color of the binary. The knowledge of intrinsic colors

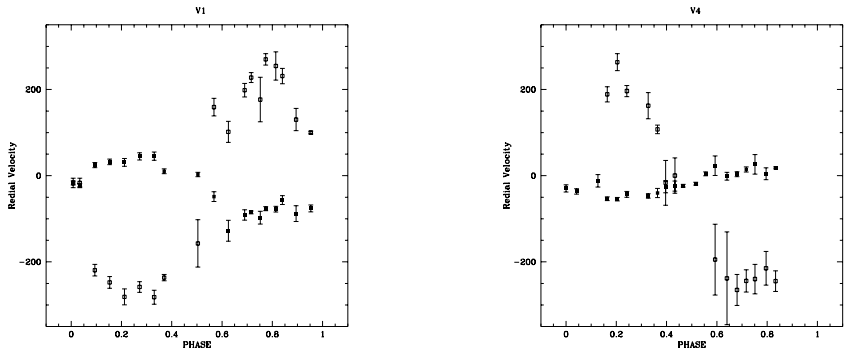

Figure 1.3 These figures are taken from von Braun et al. (1996) and represent the radial velocity curves of eclipsing binary stars V1 and V4 in the globular cluster M71 (Yan & Mateo 1994; McVean et al. 1997); they are used as examples for radial velocity curves here. Filled symbols represent the velocity amplitude for one of the binary components, the open symbols for the other component. For V1, one can see that $K1 \sim 75$ km/s and $K2 \sim 230$ km/s. For V4, the amplitudes are roughly 50 km/s and 220 km/s.

and magnitudes of the systems is therefore vital to the method. The main sources of error in the distance determination are a) uncertainties in the the relation between the surface brightness within a given bandpass and the surface temperature of the binary and b) the precise determination of the interstellar reddening along the line of sight to the EB which would not only dim the light of the star but also cause its color to appear redder. The method itself, however, is free of intermediate calibration steps and can provide direct distances out to tens of kpc. In turn, the knowledge of the distances to GCs can then be used to calibrate a variety of other methods, such as the relation between luminosity and metallicity for RR Lyrae stars.

1.2.3 Calculation of Stellar Masses

The very same analysis can, in principle, be used to obtain the Population II masses of the individual components of the EB system. Based on Keplerian/Newtonian Physics, the simplified case of a detached system in which the stars are not tidally distorted and have uniform surface brightness can be solved analytically by:

$$\frac{(M_1 \sin i)^3}{(M_1 + M_2)^2} = \frac{P_{orbital} K_2^3}{2\pi G}. \tag{1.2}$$

As long as the system is a double-lined spectroscopic binary (i.e., both components' spectral lines are visible in the spectrum), the individual present-day masses of the components may be calculated.

If the total mass is conserved, the evolution of any EB system may be expressed by $M_1 + M_2 = M_{1,0} + M_{2,0} + M_L$, where M_i are the present-day masses of the two components, $M_{i,0}$ are their initial masses, and M_L is the total mass loss from the system. If one assumes that $M_L = 0$ (no mass loss), then the difference between present day masses and initial masses of the components is only due to the mass transfer history between the two stars. This demonstrates the value of detecting *unevolved* EB systems. These are systems where the binary components are detached, thus no mass transfer has taken place, and the present day masses are therefore equal to the initial masses.

A direct determination of the ages of the systems, however, remains a challenging task. The reasons for this are described in Paczyński (1996); we will briefly repeat them here. Analysis of various theoretical isochrones (e.g., Bertelli et al. 1994; VandenBerg et al. 2000) readily shows that at the main-sequence turnoff (MSTO),

$$\text{age}_{MSTO} \sim \text{Lum}_{MSTO}^{-1} \sim \text{Mass}_{MSTO}^{-3.7}. \tag{1.3}$$

From equation 1.2 it is apparent that $M_1 \sim K_2^3$, where M_1 is the mass of the first component and K_2 is the radial velocity amplitude of the second component. Combining these two relations gives

$$\text{age}_{MSTO} \sim K^{-11}, \tag{1.4}$$

implying a 12% uncertainty in age for a 1% uncertainty in velocity amplitude, making direct age determinations all but impossible. A more rewarding approach would therefore be to use the MSTO masses to provide a fundamental check of the masses

predicted by stellar models at low metallicities. In order to do this, one needs to either detect detached EB systems (and assume no mass loss, in which case the zero-age masses equal the MSTO masses of the two components), or reconstruct the history of mass transfer between contact EBs to obtain zero-age masses for the two stars.

1.3 Differential Extinction: Using Globular Clusters as Tools

As mentioned above, it is essential for distance or mass determinations for binaries that the intrinsic magnitude and color, and thus the extinction along the line of the sight, be known. While GCs typically suffer an average extinction which is dependent upon their Galactic latitude, they may also display the effects of variable "differential" reddening on the scale of arcminutes or less across the face of the cluster. Typically, this differential extinction manifests itself by broadening and moving the features of the GC CMD as a function of the position on the sky. More specifically, the broadening is most significant in the regions where the vector along which reddening occurs is approximately perpendicular to a hypothetical isochrone fit through this region in the CMD. These regions are the subgiant branch (SGB), the red giant branch (RGB) and the MSTO (see Figure 1.4). The fainter regions ($V > 21$) of the main sequence, however, are almost parallel to the reddening vector. Thus, they are less affected and appear tight, even when differential reddening occurs.

GCs represent a unique tool to calculate the differential extinction. All stars in a GC have the same age, are at the same distance, and are thought (in most cases) to have a uniform metallicity, resulting in a CMD such as depicted in Figure 1.4. Furthermore, the GC-member stars significantly outnumber foreground or background stars when observing within the tidal radius of the GC. As a result, any spread in the

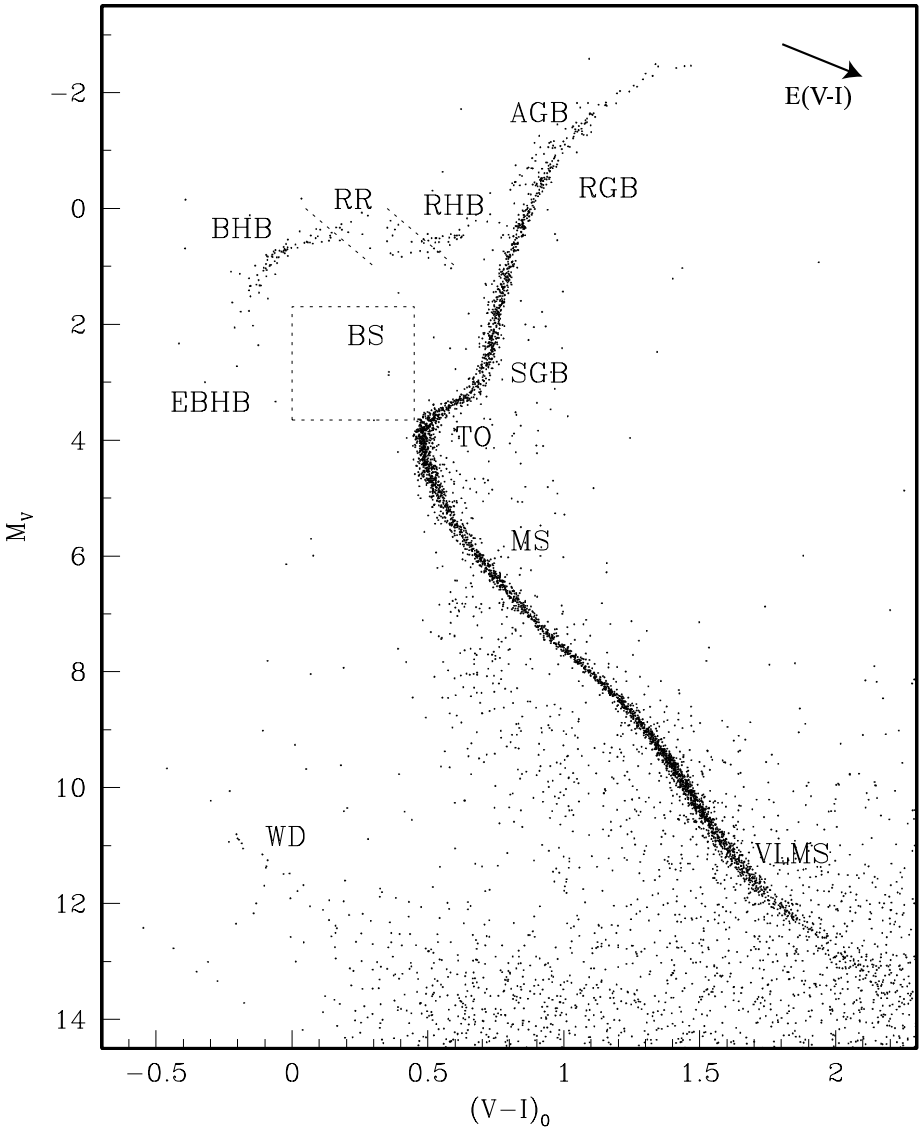

Figure 1.4 This figure, comprised of data for NGC 6397, M3, and M13, was provided by Alfred Rosenberg (private communication 2002 and Rosenberg 2000), and it illustrates the various areas in a GC CMD: the **VLMS** (very low main sequence), **MS** (main sequence), **TO** (turnoff, also referred to as **MSTO**), **SGB** (subgiant branch), **RGB** (red giant branch), **AGB** (asymptotic giant branch), **RHB** (red horizontal branch), **RR** (region where RR Lyrae pulsators are found), **BHB** (blue horizontal branch), **EBHB** (extremely blue horizontal branch), **BS** (blue straggler region), and **WD** (white dwarfs region). In addition, we show, in the top right corner, the approximate direction of the reddening vector.

shapes of the CMD features of a GC can be expected to be due to differential reddening. Since this reddening occurs along a well-defined vector with slope A_V/E_{V-I} (the value of this quantity depends the central wavelengths of the VI filters; see Cardelli et al. 1989; Schlegel et al. 1998), it is straightforward to reverse-engineer the differential extinction process and determine how much more extinction on average any region A suffers than any region B, provided both these regions contain a sufficiently high number of GC-member stars. GCs therefore offer the rare opportunity to correct for differential reddening by using the GC data themselves without having to rely on dust studies from the literature, plus they allow the use of isochrone fitting to determine the value for a reddening zero point to be added to the differential extinction.

Since it is essential to know the extinction along the line of sight to the binary system under investigation, we developed a method (described in Chapter III) which corrects for the effect of differential extinction across the face of the cluster by using our high-quality VI photometry. Our procedure is, in principle, similar to the ones used by Kaluzny & Krzeminski (1993) and Piotto et al. (1999). It aims to find the average ΔE_{V-I} for subregions of the cluster field of approximately 1-4 arcmin^2 in size with respect to a fiducial region in the cluster where little or no differential reddening is apparent and where the overall E_{V-I} is small compared to the rest of the cluster.

Some of our results indicate variations in E_{V-I} of up to ~ 0.2 mag on the scale of arcminutes across the field of a GC. Differential reddening this strong can wreak havoc with photometric and spectroscopic studies of cluster stars. The inherent uncertainties in the various parameters of the CMD (e.g., magnitude and color of the MSTO, HB features, etc.) are greatly amplified. Moreover, one may "detect" age or surface-temperature gradients where there are none in reality. To give an example of

the magnitude of the effect, using the recently published color-temperature relations by Houdashelt et al. (2000) the effective temperature of a solar-metallicity, main sequence star with $V - I \sim 0.8$ would vary by approximately $600K$ for a differential reddening effect of $E_{V-I} \sim 0.2$ mag. Since $d \sim T^2$ for a given stellar radius and observed flux, $\Delta T \sim 600K$ for a $5500K$ star would produce a 22% error in distance. Alternatively, analysis of isochrones by VandenBerg et al. (2000) shows that a $\Delta T \sim 600K$ produces a Δ [Fe/H] of around 0.8 dex for a main sequence star with –1 < [Fe/H] < 0 and $T \sim 6000K$.

One may further use the differential extinction results from the GC data to compare to independently calculated reddening estimates such as the reddening maps by Burstein & Heiles (1982) or Schlegel et al. (1998, SFD hereafter). Since the SFD maps are based on infrared emission from dust, our maps provide an independent check of whether, if at all, they tend to overestimate reddening, as was suggested by, e.g., Arce & Goodman (1999) for regions with $A_V > 0.5$ mag. Features detected by one method and not the other can give insight into properties of the interstellar medium (ISM) such as grain size and distribution as well as temperature.

1.4 The Globular Clusters NGC 3201, M10, & M12

We are currently undertaking a survey of 10 Galactic GCs (see Table 1.1) with the aim of identifying photometrically variable EBs around or below the MSTO. The results for first three GCs of this survey (NGC 3201, M10, & M12), with respect to differential extinction across their respective field of view and the existence of variable stars in their fields, are presented in this work. Our observing strategy for all GCs, aimed at detecting binaries with periods between approximately 0.1 and 5 days (see Hut et al. 1992) consists of repeated observations of a set of GCs during

each night. Multiple observing runs are usually helpful in detecting variables with a period of close to one day (or to a multiple thereof). The more valuable detached systems are generally much harder to detect because a) they will eclipse each other only within a small range of inclination angles due to the larger distances between the components, b) their duty cycle[3] is very low, and c) they vary less in brightness (if at all) inbetween eclipses than the more distorted components of contact systems. Fairly extensive coverage is therefore usually needed in order to detect detached EB systems.

By chance, NGC 3201 was the first cluster we examined and thus the one we used to establish our data reduction pipeline (von Braun & Mateo 2001, 2002). M10 & M12 were analyzed at the same time (von Braun et al. 2002). Therefore, much of the explanation of the methods and the description of the results here is done using NGC 3201 as an example. Results for M10 & M12 are presented separately from NGC 3201 wherever appropriate. The entire set of GCs of our sample is shown in Table 1.1.

1.4.1 NGC 3201

NGC 3201 is a low-latitude cluster located at $\alpha_{2000} = 10^h17^m36.8^s$ and $\delta_{2000} = 46°24'40''$ or $l = 277.2°$ and $b = 8.6°$ (Harris 1996) with a retrograde orbit around the center of the Milky Way. Its nearby location ($d = 5.2$ kpc) and low concentration ($c = 1.31$) make it an attractive target for photometric studies. Recent studies include Cacciari (1984); Brewer et al. (1993); Côté et al. (1994); Covino & Ortolani (1997); Gonzalez & Wallerstein (1998).

Due to its low-latitude position, the effects of differential reddening across the face of NGC 3201 are quite substantial. The existence of variable extinction was noted

[3]The duty cycle of an EB is defined as the fraction of the orbital period during which the system is experiencing an eclipse for an edge-on system (inclination angle $i = 90°$).

Table 1.1. GCs in our Survey

Cluster	RA_{2000}[a]	Dec_{2000}[b]	L	B	R_{sun}[c]	E_{B-V}	[Fe/H]	c[d]	r_{core}[e]	r_{tidal}[e]
NGC 288	00 52 47.5	-26 35 24	152.28	-89.38	8.3	0.03	-1.24	0.96	1.42	12.94
NGC 3201	10 17 36.8	-46 24 40	277.23	8.64	5.2	0.21	-1.58	1.30	1.43	28.45
M53 (NGC 5024)	13 12 55.3	18 10 09	332.96	79.76	18.3	0.02	-1.99	1.78	0.36	21.75
NGC 5053	13 16 27.0	17 41 53	335.69	78.94	16.4	0.04	-2.29	0.84	1.98	13.67
M12 (NGC 6218)	16 47 14.5	-1 56 52	15.72	26.31	4.9	0.19	-1.48	1.39	0.72	17.60
M10 (NGC 6254)	16 57 08.9	-4 05 58	15.14	23.08	4.4	0.28	-1.52	1.40	0.86	21.48
M92 (NGC 6341)	17 17 07.3	43 08 11	68.34	34.86	8.2	0.02	-2.29	1.81	0.23	15.17
M22 (NGC 6656)	18 36 24.2	-23 54 12	9.89	-7.55	3.2	0.34	-1.64	1.31	1.42	28.97
M15 (NGC 7078)	21 29 58.3	12 10 01	65.01	-27.31	10.3	0.10	-2.25	2.50[f]	0.07	21.50
M30 (NGC 7099)	21 40 22.0	-23 10 45	27.18	-46.83	8.0	0.03	-2.12	2.50[f]	0.06	18.34

[a]Units: hh mm ss

[b]Units: dd mm ss

[c]Distance from sun, in units of kpc.

[d]Central concentration $c = log\frac{r_{tidal}}{r_{core}}$.

[e]In units of arcmin.

[f]Core-collapsed cluster.

Note. — All data in this table are based on Harris (1996).

in practically all earlier studies of this cluster. Cacciari (1984), for instance, finds an irregular reddening distribution with a variation of $\Delta E_{B-V} = 0.03$ mag in addition to a mean value of $E_{B-V} = 0.21$. Gonzalez & Wallerstein (1998) report a range in E_{B-V} of as much as 0.1 mag across NGC 3201. Using spectroscopic data for 18 giants in NGC 3201, Gonzalez & Wallerstein (1998) correct for the color spread by modeling the reddening in E_{B-V} as a plane in α and δ as a low-resolution reddening map.

The recently published SFD dust infrared emission maps (Schlegel et al. 1998) seem to indicate, however, that the dust distribution in the region of NGC 3201 is too clumpy to be fitted by a linear function in position, even on the scale of arcminutes.

NGC 3201 has furthermore been probed for the existence of binary stars in the past, most recently in the spectroscopic study by Côté et al. (1994). The results of even earlier work on variables in NGC 3201 are summarized in Hogg (1973) and Clement et al. (2001), and references therein. As these studies concentrate on vari-

ables at least 1.5 mag brighter than the MSTO, their results do not overlap with the work presented here.

1.4.2 M10 & M12

M10 (NGC 6254) and M12 (NGC 6218) are two equatorial clusters in located at $\alpha_{2000} = 16^h57^m08.9^s$ and $\delta_{2000} = -4°05'58''$ ($l = 15.14°$; $b = 23.08°$), and at $\alpha_{2000} = 16^h47^m14.5^s$ and $\delta_{2000} = -1°56'52''$ ($l = 15.72°$; $b = 26.31°$), respectively (Harris 1996). They are nearby (M10: 4.4 kpc and M12: 4.9 kpc) which makes them attractive targets for monitoring studies. Although they are separated by only 3° in the sky, the existence of strong differential reddening was observed for M10 (Kennedy et al. 1996; Rosenberg et al. 2000a), but not for M12. In addition, both clusters have been analyzed for the existence of variable stars in the past (for a summary, see Clement et al. 2001). Previous studies searched for luminous variables on the RGB and/or HB of the clusters and therefore do not overlap with the magnitude range covered in this work.

1.5 Outline of Dissertation

Chapter II contains a description of our photometry observations for the three GCs NGC 3201, M10, & M12. In addition, we outline our photometric reductions of the data. In Chapter III, we explain how we correct for the differential reddening we discover across the fields of NGC 3201 and M10, and, to a lesser extent, of M12. Further, we calculate the reddening zero points for the three GCs to be added to the differential reddening values. Chapter IV describes how we detect the variable stars in the GC fields, calculate their periods and classify their types. We further explain how we determine distances to, and GC-membership of the detected variable systems. Chapter V lists our results concerning variables in the three clusters, including the

phased photometric lightcurves, the variables' locations in the field and CMD, and our estimates concerning distance and GC membership of the variables. We briefly summarize our results, discuss potential implications, and outline future work in Chapter VI.

CHAPTER II

Photometry Observations, Data Processing, and Basic Data Reduction

2.1 Photometry Observations

2.1.1 NGC 3201 – Initial Photometry Observations

The bulk of the photometry observations for NGC 3201 was conducted during three separate observing runs in June 1996, May 1997, and May 1998 at the Las Campanas Observatory (LCO) 1 m Swope Telescope. For all three runs Johnson-Cousins VI filters were used, and the number of images are approximately evenly divided between the two bands. Table 2.1 lists the details of the NGC 3201 photometry observations. During the May 1998 run we took additional shorter exposures (10s and 60s exposure time) of the cluster to complete the CMD in the brighter regions (these shorter exposures were not used to detect variable candidates).

2.1.2 M10 & M12

The observations for M10 and M12 were obtained during multiple runs between June 1995 and May 1999 at the Michigan-Dartmouth-MIT (MDM) Observatory's 1.3m and the LCO 1m Telescope. Table 2.1 lists the details. During all observing runs, we used 2048^2 pix CCDs with different field sizes and standard Johnson-Cousins VI filters. The number of epochs was about evenly divided between V and I. During two runs, we took additional shorter (10s) exposures to complete the CMDs in the

Table 2.1. Photometry Observations

Cluster	Date	Telescope	Field-of-View Size[a]	Number of Epochs[b]
NGC 3201	June 1996	LCO 1m	24	17
...	May 1997	LCO 1m	23.5	164
...	May 1998[d]	LCO 1m	23.5	89
M10	April 1996	MDM 1.3m	14.9	4
...	May 1997	LCO 1m	23.5	29
...	June 1997	MDM 1.3m	14.9	35
...	August 1997	LCO 1m	23.5	23
...	May 1998[d]	LCO 1m	23.5	25
...	August 1998	MDM 1.3m	17	16
...	August 1998	LCO 1m	23.5	14
...	May 1999	MDM 1.3m	17	12
M12	June 1995	MDM 1.3m	10.6	60
...	April 1996	MDM 1.3m	14.9	4
...	May 1997	LCO 1m	23.5	28
...	June 1997	MDM 1.3m	14.9	39
...	August 1997[d]	LCO 1m	23.5	18
...	May 1998	LCO 1m	23.5	22
...	August 1998	MDM 1.3m	17	16
...	August 1998	LCO 1m	23.5	8
...	May 1999	MDM 1.3m	17	10

[a]In units of arcminutes on the side.

[b]This number of 600s exposure time epochs is more or less evenly divided between V and I.

[c]We performed additional photometry observations of selected smaller fields of NGC 3201 as preparation for our spectroscopy follow-up observations. These additional observations are described in detail in Section 5.1.1.

[d]During this run, we took additional 10s exposures to complete the CMD in brighter regions. These shorter exposures were not used to look for variables.

brighter regions (see Table 2.1). As for NGC 3201 these shorter observations were not used to look for variable stars. All exposures are centered on the cluster center itself. The reason for the rather large number of observing runs with relatively few epochs per run (compared to NGC 3201 and the other clusters in our sample) is the equatorial location of both M10 and M12. Consequently, neither cluster is ever located closer to the zenith than 30° from MDM or from LCO. As a result, the two clusters were observed for only up to ~ 2 hours each per night when seeing conditions were good, with the rest of the time dedicated to other clusters in our sample.

2.2 Data Processing and Basic Data Reduction

2.2.1 NGC 3201

The initial processing of the raw CCD images of the May 1998 observing run was done with the routines in the IRAF[1] CCDPROC package. For each night, 10 bias frames were combined for the bias subtraction. The V band flats were produced by combining between 4 and 6 twilight flat images per night. All I band data were first flattened using an image comprised of 15 individual I band domeflats, and then divided by a normalized, dome-flattened dark-sky-flat which itself was created by median-averaging approximately 40 individual different blank sky fields. Finally, the I band images were corrected for fringing by subtracting a fringe image which was created by subtracting the mean pixel value of the dark-sky-flat from the dark-sky-flat image itself.

The processed data were reduced using DoPHOT (Schechter et al. 1993) in "fixed-position mode" where the positions of stars are fixed (after correcting for global frame-to-frame shifts as well as small distortions) to the positions measured on a deep-photometry template image obtained by co-adding the ~ 15 best-seeing frames.

The photometric results for every star were weighted by the inverse square of the photometric error (as returned by DoPHOT) and averaged over all frames with the same exposure time to obtain the final magnitude for the star under investigation. For the 600s exposures, our only requirement was that a star appear[2] in more than 75% of the epochs. The 60s images were taken to complete the CMD in the brighter regions; we only took magnitudes from these exposures of stars which were saturated in the 600s exposures. The same procedure was followed for the 10s frames. Aperture

[1]IRAF is distributed by the National Optical Astronomy Observatories, which are operated by the Association of Universities for Research in Astronomy, Inc., under cooperative agreement with the NSF.

[2]A detection of a star occurs when a subraster of pixels with a signal sufficiently high above the sky background is filtered through a DoPHOT stellar model profile (based on the parameters x, y, central intensity, and three shape parameters) and the object under investigation is classified as a star.

corrections were applied by calculating one constant value for the whole chip after we found little dependence upon position on the CCD. The data from the shorter exposures where shifted to the photometric system of the 600s exposures using non-saturated stars in common.

During our consecutive two photometric nights (May 2 & 3, 1998), we obtained a total of more than 140 observations of various Landolt (1992) standard stars which covered a range of $-0.2 < V - I < 2.2$ in color as well as $1.15 < X < 1.55$ in airmass. Using the IRAF PHOTCAL package, we applied one single standard star solution for data from both nights of the form

$$V = v + a_0 + b_0 X_v + c_0(v - i) \tag{2.1}$$

$$V - I = a_1 + b_1 X_i + c_1(v - i), \tag{2.2}$$

where the a_j, b_j, and c_j are the fitted constants, X_{filter} is the airmass of the exposure taken with the respective filter, the lowercase magnitudes are instrumental, and the uppercase ones are the known magnitudes of the standard stars. The root mean square error was 0.007 mag and 0.016 mag for V and $V - I$, respectively. We obtained exposures of all three clusters presented in this work during these nights, thus, no secondary calibration was necessary.

Astrometry was performed by identifying 59 United States Naval Observatory (USNO) reference stars (Monet et al. 1998) in NGC 3201 and using the IRAF IMAGES package for the coordinate transformation. A linear fit of the form ax + by + c produced errors around 0.2 arcsec, consistent with the USNO precision. The tangent point of the transformation is $(x, y) = (962.7, 934.2)$ and corresponds to $\alpha_{2000} = 10^h17^m31.2^s$ and $\delta_{2000} = -46°24'11''$. The rotation of x and y with respect to α and δ is 91.23°, and the pixel scale is 0.695 pix/arcsec.

The data obtained during the June 1996 and May 1997 data were processed and reduced in the same manner as the May 1998 data. All data were shifted to the coordinates and photometric system of the May 1998 600s exposures.

Our photometry results for NGC 3201 are presented in the form of a CMD in Figure 2.1; they are available online at `http://adc.gsfc.nasa.gov/adc-cgi/cat.pl?/journal_tables/AJ/123/279`. At this point in the data reduction, the main sequence of NGC 3201 in this fully calibrated CMD seemed exceptionally broad. After ruling out a number of possible instrumental causes for this effect, and after we noted a clear dependence of the appearance of the main sequence upon the positions of stars on the CCD (illustrated in Fig. 3.1 in the next chapter), we concluded that the underlying cause for the broadness of our main sequence was differential extinction across the field of view. This seemed especially sensible given the low-latitude location of NGC 3201 ($b \sim 8,5^\circ$).

2.2.2 M10 & M12

The IRAF processing of the M10 and M12 data was performed in basically the same way as described for NGC 3201. All data were reduced using DoPHOT in fixed position mode after aligning every image to a deep-photometry template image consisting of the best seeing frames for each filter from every run. Aperture corrections and variable PSF were fitted to the May 1998 data as second order polynomials in x and y. Our astrometric solutions for both cluster fields, based on approximately 120 USNO reference stars (Monet et al. 1998), respectively, produced linear fits in x and y with a random mean scatter (rms) of around 0.2 arcsec, again consistent with the USNO precision. For M10 the tangent point of the astrometric transformation is $(x, y) = (933.8, 1002.4)$, corresponding to $\alpha_{2000} = 17^h13^m10.3^s$ and $\delta_{2000} = -4^\circ04'47''$. The rotation of x and y with respect to α and δ is 91.21°. For

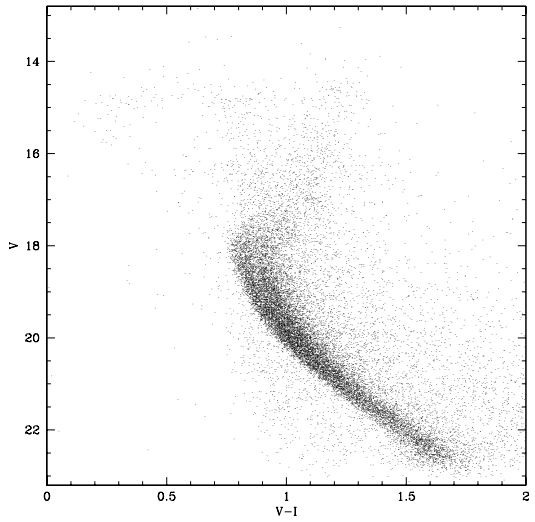

Figure 2.1 The CMD of NGC 3201 before applying any reddening correction. Strong differential reddening across the field of view along the reddening vector with slope 1.919 (Cardelli et al. 1989) causes the region around the main-sequence turnoff, the subgiant branch, and the red giant branch to appear exceptionally broad since the reddening vector is practically perpendicular to a hypothetical isochrone fit to these areas in the CMD. The division between the deep (600s) and shallow (10s & 60s) photometry data is located around $V \sim 17$. The data used to create this figure are available online at `http://adc.gsfc.nasa.gov/adc-cgi/cat.pl?/journal_tables/AJ/123/279`.

M12 these values are $(x, y) = (984.4, 1021.2)$, corresponding to $\alpha_{2000} = 17^h32^m09.7^s$ and $\delta_{2000} = -1°56'13''$, with a rotation of x and y with respect to α and δ of 91.22°. The Pixel scale is 0.695 pix/arcsec. Photometric calibration of the May 1998 data is described in Section 2.2.1.

All other M10 and M12 data were shifted to the coordinates and the photometric system of the May 1998 600s exposures, including the shorter exposures. In the process of combining the 10s exposures with the deep data, we fit for a zero point and color term to match the two sets, thereby effectively treating the deep data as photometric standards. Whenever we had two measurements for the same star, we kept the one with the lower photometric error associated with it (in most cases, this was the 600s measurement). The division between the two photometry sets occurs around $V \sim 17 - 17.5$. We note that we are sensitive to variable detection up to

$V \sim 16 - 16.5$ since the CCDs we used have different quantum efficiencies and some of the observations were taken through thin layers of clouds.

Photometric results for every star, weighted by the inverse square of the photometric error for the respective measurement, were averaged with the only requirement that a star appear in approximately 20% or more of the epochs. This condition is much less stringent than its corresponding counterpart in the analysis of NGC 3201 (see above) where we set this threshold to 75%. The reason for this difference lies in the varying field sizes of the CCDs used for M10 and M12 (see Table 2.1). A larger field (LCO data) will obviously include more stars than a smaller one, whereas a higher spatial resolution (MDM data) allows us to get closer to the GC center with our reductions.

Our photometry results for M10 and M12 are presented as observed CMDs in Figures 2.2 and 2.3, respectively. Based on similarities between the undereddened CMDs of NGC 3201 (Figure 2.1) and M10 it appears that M10 suffers from differential reddening across the field of view, as previously suggested by, e.g, Kennedy et al. (1996). M10's main sequence is broad, especially around the MSTO where the reddening vector (Cardelli et al. 1989) is approximately perpendicular to a hypothetical isochrone fit to this particular region. Its SGB, RGB, and HB display the same feature, whereas the fainter region of the main sequence ($V > 20$), where the reddening vector is almost parallel an isochrone fit to the region, appears tighter. This behavior clearly rules out any sort of photometric error as the reason for the broadness of the CMD features since, in that case, one would observe well defined MSTO and SGB regions and a main sequence which would flare up at fainter magnitudes. M12's CMD, does not display the signature of differential extinction as strongly as M10, indicating that the effects of differential reddening across its field

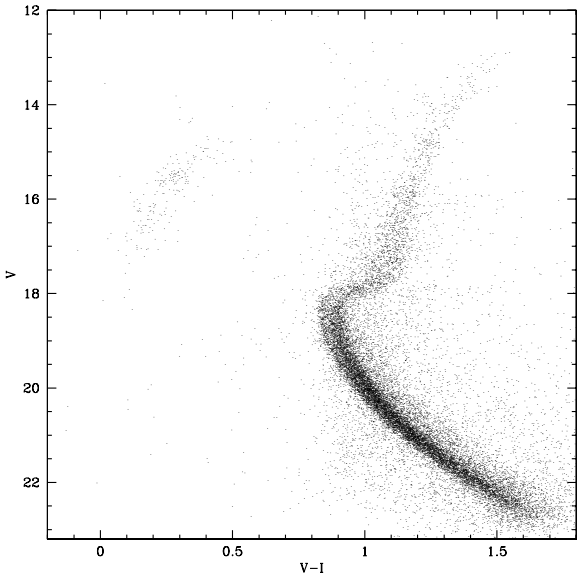

Figure 2.2 CMD of M10 before applying any extinction correction. The typical symptoms of differential extinction across the field are present: main sequence appears relatively tight where it is approximately parallel to the reddening vector (at V fainter than ~ 20), whereas regions more or less perpendicular to the reddening vector, such as the MSTO, the subgiant and giant branches as well as the blue HB, appear broad. As part of the process of combining 600s and 10s exposure data, we set the division at around $V \sim 17$ where saturation of the deep data sets in.

are small, despite the fact that the two clusters are separated by less than 3° in the sky.

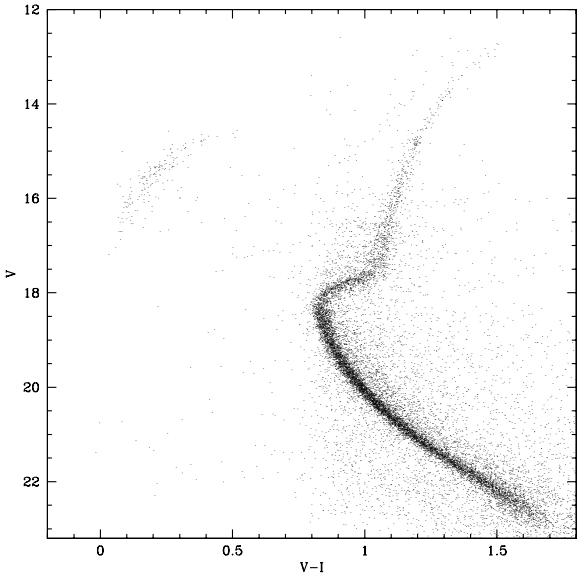

Figure 2.3 CMD of M12 before applying any extinction correction. The signatures of differential reddening are much less visible than in M10 (see Fig. 2.2). The division between the deep (600s) and shallow (10s) photometry data is located around $V \sim 17$.

CHAPTER III

Extinction Corrections

3.1 Mapping the Differential Reddening

3.1.1 NGC 3201

As described in Section 2.2.1 and illustrated in Figure 2.1, we discovered that NGC 3201 was suffering differential extinction across its field of view. Figure 3.1 shows how the main sequence varies in broadness and position as a function of x, y location on the CCD. We ruled out other causes for this effect such as charge transfer efficiency (which would only cause a dependence of main sequence broadening/location upon the readout direction on the CCD) and photometric error (which would result in main sequence broadening at fainter magnitudes). Since the metallicity of NGC 3201 is well constrained (Gonzalez & Wallerstein 1998), we also don't have any reason to believe that a range in [Fe/H] could be the cause for the broadening of NGC 3201's main sequence.

One of the main sources of error in the use of eclipsing binary stars for distance determination is the knowledge of intrinsic magnitudes and colors, i.e., the knowledge of interstellar extinction any binary system is suffering (Paczyński 1996). This motivated us to create a differential reddening map for NGC 3201 since any binary star data are not useful without this correction. In order to create such a map for NGC 3201, we developed the steps described below (see also Fig. 3.2):

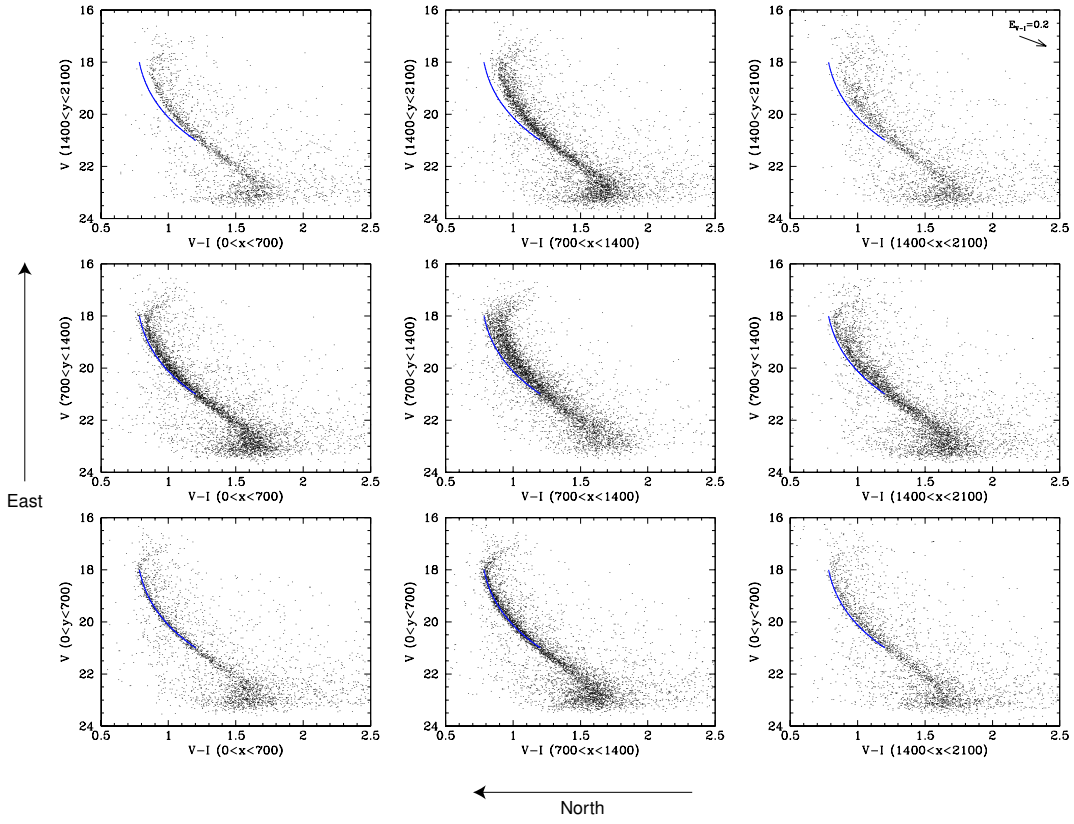

Figure 3.1 "Raw" (calibrated but before dereddening) CMDs of 9 subregions of the field of view of NGC 3201. The x and y ranges of the respective subregion are given on the axes of each individual CMD. $x = 0, 700, 1400, 2100$ approximately correspond to $\delta_{2000} = -46°13'03'', -46°21'09'', -46°29'16''$, and $-46°37'22''$, respectively; $y = 0, 700, 1400, 2100$ approximately correspond to $\alpha_{2000} = 10^h16^m27^s, 10^h17^m14^s, 10^h18^m01^s$, and $10^h18^m48^s$, respectively. The directional arrows on the bottom and the left of the image show the approximate orientation of the CCD. The varying appearance and broadness of the main sequence as a function of position clearly indicates the differential reddening across the field of view (although crowding certainly accounts for some of the broadening toward the cluster center). The line through the CMDs represents the best fit through the datapoints in the fiducial region $1200 < x < 1600$ and $0 < y < 400$ (described in Section 3.1.1, item 1). It is apparent that there is not only less differential reddening in that region (tight main sequence), but also that the overall E_{V-I} is low. The reddening vector for $E_{V-I} = 0.2$ is shown in the top right panel.

1. A fiducial region was chosen in which

   - very little or no differential reddening occurred, i.e., where the main sequence appeared narrow;
   - the overall E_{V-I} was small with respect to the rest of the field of view;
   - there were enough stars in the field to obtain a statistically reliable fit to their positions on the CMD.

   The coordinates of this fiducial region are approximately $10^h16^m26^s < \alpha_{2000} < 10^h16^m53^s$ and $-46°31'21'' < \delta_{2000} < -46°26'44''$ (it is located approximately 11 arcmin south-west of the cluster center; see Figures 3.3 through 3.7).

2. A high-order polynomial was fit to the main sequence stars with $18 < V < 21$ and $0.7 < V-I < 1.4$ in the fiducial region, using algorithms supplied by Robbie Dohm-Palmer (2000, private communication) which enabled us to separate the main sequence stars from background stars in the CMD, and by Press et al. (1992), which provided the least-squares fit to the data (see Fig. 3.2).

3. We divided the field of view into subregions of different sizes in order to have a sufficient number of stars in each region. Toward the outer parts of the field, the stellar density decreases. As a result, the sizes of the subregions increase. The inner subregions are all of the same size (100×100 pixel, corresponding to $70\times70\,\mathrm{arcsec}^2$) See Fig. 3.3.

4. For each of these regions, every star falling between $17.9 < V < 21.1$ and $0.65 < V - I < 1.45$ was incrementally moved along the reddening vector defined by the relations in Cardelli et al. (1989) until it intersected the fit (see Fig. 3.2).

5. The statistical biweight (see Beers et al. 1990) of all these incremental shifts of the stars in a given subregion provided the value of the total shift along the reddening vector for each star. Since the slope of the reddening vector for a standard extinction law is known (1.919; see Cardelli et al. 1989), the differential E_{V-I} for each star corresponds to the $(V-I)$-component of the vector described above (Fig. 3.2).

6. For six of the 100×100 pixel subregions as well as one 200×300 pixel subregion on the extinction map shown in Fig. 3.3, too few stars were present to calculate the average reddening. For these cases, we calculated E_{V-I} by simply averaging the reddening values of all the neighboring subregions[1].

7. Our error analysis for the shifts described above involved the following:

   - We created an error ellipse for every star defined by the values of the associated errors (as returned by DoPHOT) in color and magnitude.
   - Since the color and magnitude errors are correlated, the error ellipse is tilted, with the tilt angle and the lengths of the semi-major and semi-minor axes functions of σ_V and σ_{V-I}. In particular, the tilt angle α of the error ellipse is given by

     $$\alpha = \arctan \sqrt{\frac{1}{1 + (\frac{\sigma I}{\sigma V})^2}}, \tag{3.1}$$

     where σI and σV are the I and V DoPHOT photometric errors, respectively.
   - One average tilt angle was obtained for every subregion under investigation by averaging the results for the individual stars. For every subregion, this

[1] In this process, every 100 pixel ×100 pixel subregion was treated individually, even if it was a part of a larger one. That is, for the 200×300 region just south of the north-east corner of the field of view in which the number of stars was too low to obtain a reddening value, the above procedure was applied six times.

angle was approximately 35° for NGC 3201, 31° for M10, and 30° for M12. The semi-major and semi-minor axes for every subregion were obtained in the same way, so that every star in a given subregion has the same error ellipse associated with it in the center.

- This error ellipse was shifted along with its respective star during the dereddening process described above in items 4 and 5. The "point of first contact" (pfc), i.e, the point at which the error ellipse first touches the fit through the data in the fiducial region, as well as the "point of last contact" (plc), represent the respective one-sigma-deviation points (see Fig. 3.2).
- These two contact points are not necessarily symmetric about the reddening value of the star (center of error ellipse), but in order to increase the readability of this work, we calculated the mean pfc and plc for a given subregion, and then their average distance from the center of the ellipse, so that $\sigma_{ellipse} = 0.5\,(\mathrm{pfc} + \mathrm{plc}) - center$.
- The final error estimate for each subregion ($\sigma_{E_{V-I}}$) given as the lower number in each of the pixels in Fig. 3.4 is then obtained by adding in quadrature $\sigma_{ellipse}$ and the error in the mean of the shifts of all the stars in the subregion under investigation.

3.1.2 M10 & M12

In order to rid the CMDs for M10 (Fig. 2.2) and M12 (Fig. 2.3) of the differential reddening effects, we essentially followed the same procedure as for NGC 3021, described above. We will only briefly review the process here and point out differences between the approach for NGC 3201 and the one for M10 & M12. As for NGC 3201, we ruled out other effects as the cause for the main sequence broadening. Based on

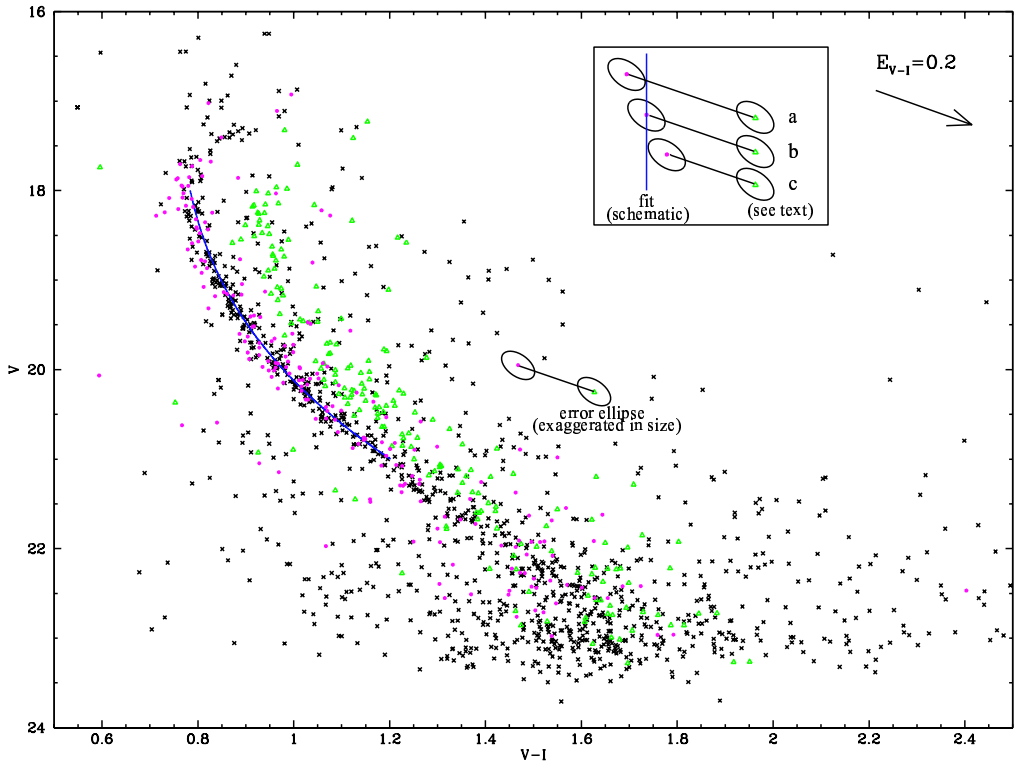

Figure 3.2 This figure illustrates the dereddening procedure which was used in for the GC. The triangles represent stars in the NGC 3201 subregion $700 < x < 800$ and $800 < y < 900$ (approximately $10^h17^m21^s < \alpha_{2000} < 10^h17^m28^s$, as well as $-46°21'07'' < \delta_{2000} < -46°22'16''$) before being dereddened; the filled circles represent the same stars after the dereddening along the reddening vector shown in the top right corner of the figure. The x-shaped symbols are the stars in the fiducial region (mentioned above) in which none or very little differential reddening is taking place. The fitted polynomial with range $18 < V < 21$ is visible as the curve through the fiducial region datapoints. The reddening for this region is close to $E_{V-I} = 0.2$ with respect to the average of the fiducial region. The tilted error ellipses, described in text and greatly exaggerated in size, are shown to illustrate our dereddening method which is schematically outlined in the box to the upper right. The straight line represents the fit through the datapoints in the fiducial region. Example **a** represents the "point of last contact" of the error ellipse with the fit, example **b** the shift from the original datapoint until it intersects the fit, and example **c** the "point of first contact" between the error ellipse and the fit.

previous studies, there is no reason to assume that the metallicities of M10 and M12 are variable within the respective GC (Sato et al. 1989; Kraft et al. 1995).

For each cluster, we chose a fiducial region in which little differential reddening occurred, whose overall extinction is low compared to the rest of the field, and which contained a sufficient number of stars to fit a polynomial to the main sequence for stars with $18.5 < V < 21$ and $0.7 < V - I < 1.4$. The field of view of each cluster was then divided into subregions of different sizes such that the number of stars in each of the subregions was large enough to produce a statistically significant result. For each of the subregions, an average offset between its stars and the polynomial fit along the reddening vector with slope 2.411 (Schlegel et al. 1998, table 6, column 4 for Landolt filters) was calculated after 1σ-outliers were deleted with an iteration. This calculated average offset corresponds to the differential E_{V-I} of each star in the subregion with respect to the fiducial region, i.e., how much more extinction the stars in the subregions suffer than the ones in the fiducial region.

The slope of the reddening vector for the analysis of NGC 3201 in Section 3.1.1 was 1.919, calculated using table 3 in Cardelli et al. (1989). The central wavelength of the I filter in Cardelli et al. (1989) is around 9000 Å, whereas the filter used during the May 1998 LCO observing run has a $\lambda_{central} \sim 8100$ Å, closer to the value given in table 6 of Schlegel et al. (1998) for Landolt filters. As a result, the conversion between E_{B-V} to E_{V-I} changes to $E_{V-I} = 1.375 \times E_{B-V}$, and the slope of the reddening vector changes to $A_V/E_{V-I} = 2.411$. This difference in slope does not affect our results for NGC 3201, neither qualitatively nor quantitatively, as we describe below.

3.2 Differential Extinction Maps

3.2.1 NGC 3201

Fig. 3.3 summarizes the results of our internal dereddening procedure for NGC 3201. Darker regions correspond to higher reddening with respect to the average reddening taking place in the fiducial region described in Section 3.1.1, item 1. For reference purposes, we included the approximate locations of this fiducial region and the core radius of NGC 3201, as well as a coordinate grid. The average E_{V-I} relative to the fiducial region (field – fiducial) is 86 millimagnitudes (mmag) with a standard deviation of 61 mmag. The individual subregions' E_{V-I} values in mmag (relative to the average reddening in the fiducial region) are shown as the top number in each of the pixels in the grid of Fig. 3.4. The bottom number in each pixel corresponds to the error in the mean for the corresponding E_{V-I} value; we discuss the derivation of the error estimate in Section 3.1.1. In addition, we included an image of NGC 3201 (Fig. 3.5) in order to indicate the locations of the fiducial region and the core radius of the globular cluster. This map represent the highest-resolution foreground dust map for any GC to date.

As we mentioned above, the slope for the reddening vector used for NGC 3201 (1.919) was different than the slope used for the analysis for M10 and M12 (2.411) A re-calculation of the reddening maps for M10 and M12 based on a slope of 1.919 (the value we used for NGC 3201), however, produced results which were identical to the ones calculated using a slope of 2.411 to within a few millimagnitudes. The values in the individual pixels of the extinction map grid (such as in Figure 3.4) changed by only a few mmag as a result of the change in the reddening vector slope. Similarly, refitted isochrones (see Section 3.3) produced an identical reddening zero point. We therefore conclude that our reddening results for NGC 3201 do not change as a result

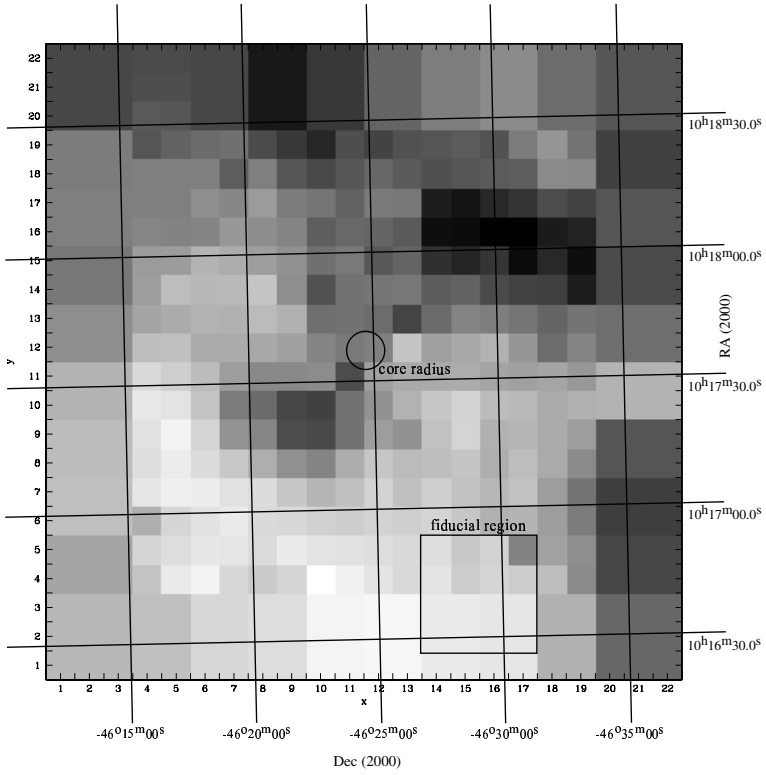

Figure 3.3 Extinction map for NGC 3201. East is up, north is to the left. The darker the color of a subregion, the more extinction is occurring in it (see Fig. 3.4). The range of differential extinction values in this Figure is approximately -30 mmag to 230 mmag (dark colored) relative to the fiducial region. Note the "ring" of larger subregions (with lower density of stars) around the center of the field of view. The size of every small subregion is approximately 70 arcsec on a side. For reference, we included an illustration of the core radius of NGC 3201 (Harris 1996) around the location of the cluster center on the extinction map as well as the location of the fiducial region described in Section 3.1.1. Furthermore, we overlaid a grid for coordinate reference. The coordinate axes x and y correspond to the ones used in Fig. 3.4. The average reddening with respect to the extinction occurring in the fiducial region is $E_{V-I} = 86 \pm 61$ mmag.

of this change in slope of the reddening vector.

At this point, these reddening values are all relative to our fiducial region which itself is suffering some mean interstellar extinction. The procedure described cannot determine the absolute reddening zero point. Thus, we had to introduce additional information, derived from previous studies, in order to calculate this zero point. The discussion of this process is given in Section 3.3.

As a first step, we subtracted our extinction map from the SFD map of the region of NGC 3201 which we observed. The SFD map of the cluster region is shown in Fig.

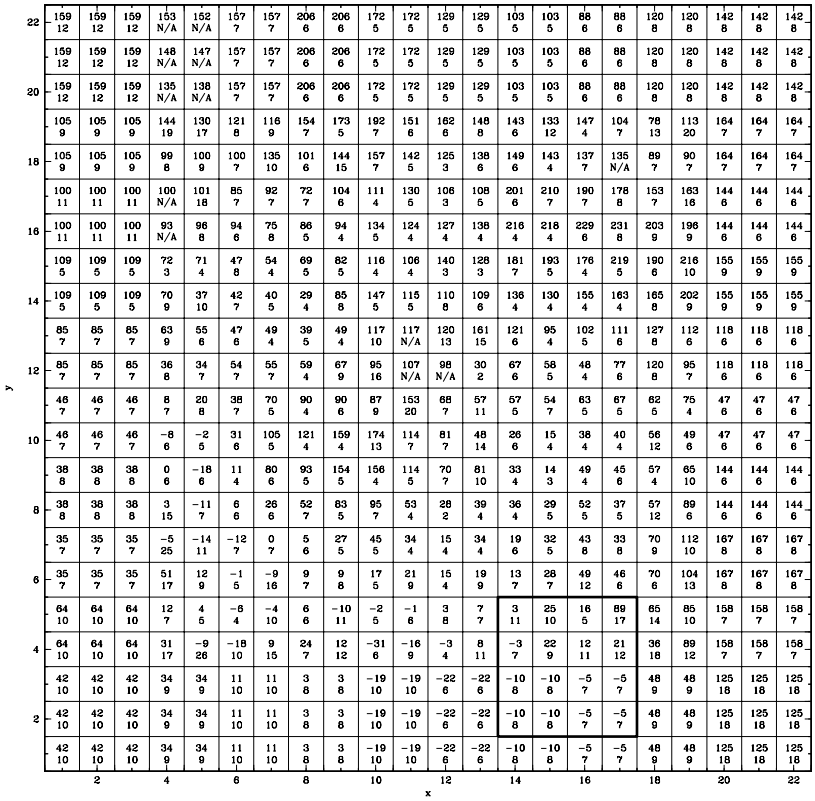

Figure 3.4 The E_{V-I} values with respect to the fiducial region for the individual pixels of our reddening map in millimagnitudes. The pixels correspond to the subregions in Fig. 3.3 with the respective values for x and y coordinates. The top number in every pixel is the value for E_{V-I} obtained with the method outlined in Section 3.1.1. The bottom number is the associated error, as described in Section 3.1.1, item 7. The pixels where the error value is N/A are the ones with an insufficient number of stars, so the reddening results were obtained by interpolation from neighboring values (see Section 3.1.1, item 6). For reference to figures 3.3, 3.5, 3.6, and 3.7 (same orientation), the location of the fiducial region is indicated in the lower right part of the figure. The average reddening with respect to the mean reddening occurring in the fiducial region is $E_{V-I} = 86 \pm 61$ mmag. In order to obtain a map of absolute reddening values, an E_{V-I} zero point has to be added to the data. We discuss the various zero points we examined in Section 3.3.2. Finally, to obtain an absolute value for E_{B-V}, one needs to multiply the absolute (i.e., including the zero point) E_{V-I} value by 0.7273 (Schlegel et al. 1998).

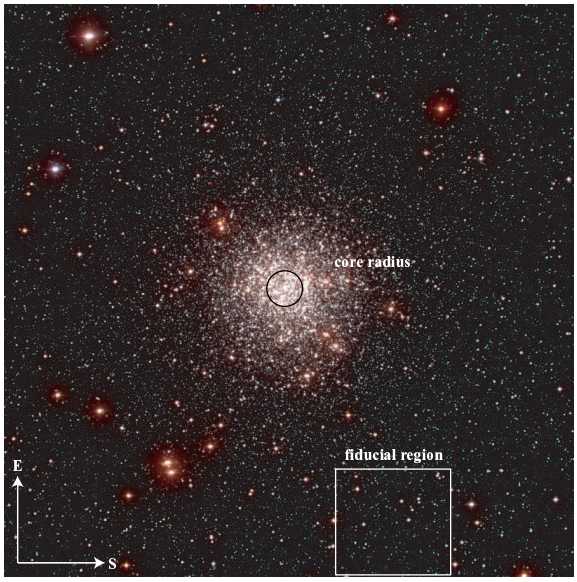

Figure 3.5 An image of NGC 3201 with illustration of core radius and location of fiducial region for purposes of comparison with Figures 3.3, 3.4, 3.6, and 3.7. The size of the field of view shown in this Figure is about 81% (area) that of the field of view of the Figures mentioned above.

3.6 with the same orientation and size as Fig. 3.3. Once again, dark corresponds to higher extinction. We added the location of the fiducial region for reference. The average E_{V-I} of the SFD map is 336 mmag with a standard deviation of 59 mmag.

A first comparison indicates that, while the larger-scale structure is the same for both extinction maps (in particular the obscuration ridge extending from the top left part of the image to the right center part of it), our map shows smaller-scale features which are not present in the SFD maps. These features are visible in the difference image in Fig. 3.7 whose orientation and size is once again identical to the other Figures. Darker regions correspond to places where our data indicate the presence of dust which does not show up in the SFD map; lighter regions show good agreement between the two maps. The average E_{V-I} of this difference map is 250 mmag with a standard deviation of 46 mmag (significantly smaller than the standard deviation of both our extinction map and the SFD map). This lower standard deviation is an indication that both our map and the SFD map of the region of NGC 3201 are

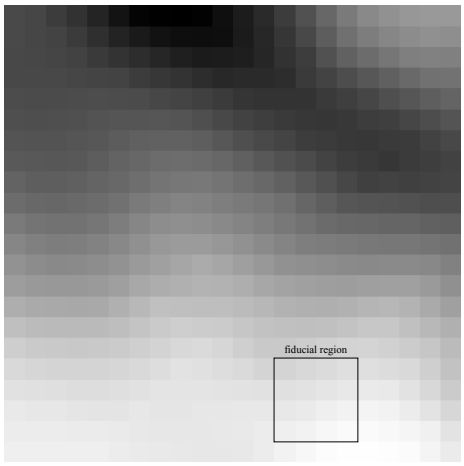

Figure 3.6 A graphical representation of the SFD data in the region of NGC 3201 that we observed. The location of our fiducial region is given for reference; the orientation of the map is the same as in Figures 3.3, 3.4, 3.5, and 3.7. Common features are easily recognizable such as the ridge of obscuring material extending from the top left part of the map to the right center. A number of smaller-scale features, however, do not show up on the SFD map (see Fig. 3.7). The average reddening is $E_{V-I} = 336 \pm 59$ mmag.

tracing many of the same features in the foreground extinction along the line of sight to the globular cluster.

The smaller-scale features present in only our map but absent in the SFD map are certainly worth further attention. At this point, we are not entirely confident that we can give a definite reason for the discrepancies, but some potential reasons could be the following:

- The smaller-scale features which are not in the SFD maps might have been smoothed out by the lower resolution of the IR observations used to create the maps.

- The temperature of the dust producing the smaller-scale features was below the detection range of the instrument used to collect the data for the SFD maps (evidenced by the "cold", clumpy structure). This way, the features would nevertheless still show up in our analysis since our method is designed to detect extinction and is independent of the temperature of the dust. We discuss the

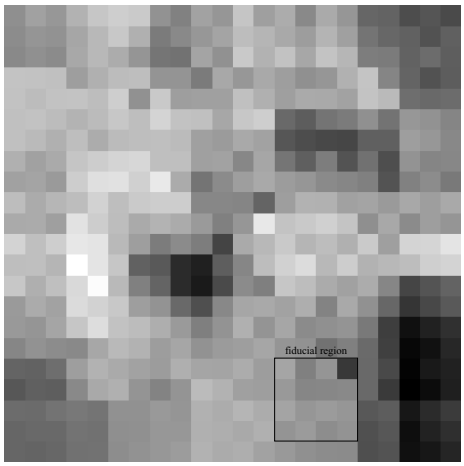

Figure 3.7 A difference plot between our extinction map (Fig. 3.3) and the SFD map (Fig. 3.6) with the same orientation. Darker regions correspond to areas where our map indicates more obscuration relative to the average value than the SFD data; lighter regions are places where the two maps agree very well. The average reddening is $E_{V-I} = 250 \pm 46$ mmag, which corresponds to the SFD-map-zero point (see Section 3.3.2). Note that the standard deviation is lower than the one of the SFD map and the one of our extinction map.

implications of this possibility in Section 6.2.1.

- The dust we are seeing is part of the globular cluster itself[2].

Fig. 3.8 illustrates the effects of applying our dereddening method to the GC's CMD. We show the CMD of NGC 3201 before and after applying the extinction map to the data. The differentially dereddened datapoints are now all shifted to the CMD-location of the stars in the fiducial region, that is, no absolute reddening zero point has been applied. The improvement is stunning. The width of the main sequence has, by applying the differential reddening map, decreased to a fraction of its former value. The SGB which was hardly visible at all in the raw CMD is now well traced out by the datapoints. Even the HB, though sparsely populated in both CMDs due to saturation effects of the bright stars in the field, is narrower in the differentially dereddened CMD.

[2]The phenomenon of cold dust ($T \sim 20K$) inside globular clusters was discussed by, e.g., Forte et al. (1992).

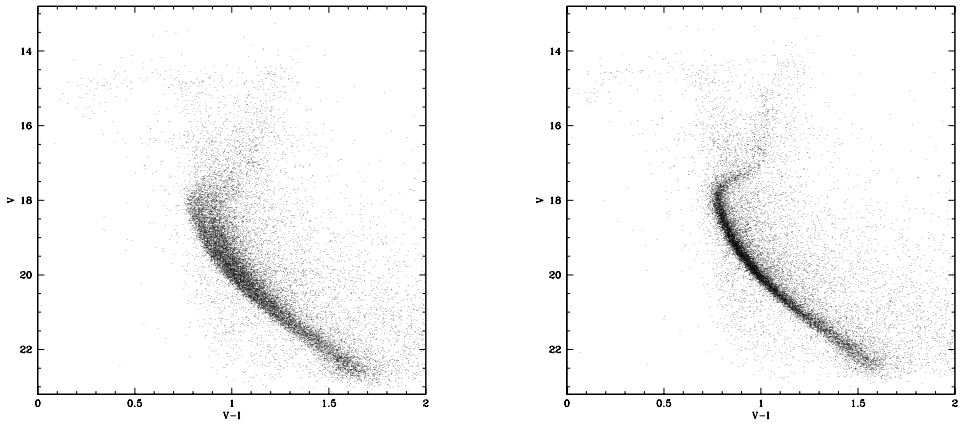

Figure 3.8 The "raw" and internally dereddened CMDs of NGC 3201. In the latter, V and $V-I$ indicate the location of the datapoints after the differential reddening with respect to the fiducial region was corrected for, i.e., after the inverse values of Fig. 3.4 were applied to the data. No reddening zero point is applied to the data in these plots. Note the improvement in CMD appearance as a results of the dereddening.

3.2.2 M10 & M12

We present our differential extinction maps in Figures 3.9 (M10) and 3.10 (M12). North is up and East is to the left (see coordinate grid on the figure included for reference). Dark corresponds to regions of higher extinction relative to the fiducial region. For reference we show the approximate locations of the cluster center and core radii (from Harris 1996) as well as the fiducial regions of the clusters[3]. The sizes of the pixels in these maps vary with stellar density from $\sim$ 140 arcsec on the side toward the center of the field to $\sim$ 280 arcsec on the side in the outer regions of the CCD. Compared to our analysis of NGC 3201, the resolution of these extinction maps is lower by a factor of four (in area) due to the lower number of reduced GC member stars in the pixels.

The average E_{V-I} relative to the fiducial region (field – fiducial) is 68 ± 41 mmag for M10 and 40 $\pm$ 58 mmag for M12; the errors represent the standard deviation about the mean. The individual subregions' average E_{V-I} values in mmag, ranging

[3]In Chapter V we show, in Figures 5.16 (M10) and 5.17 (M12), the locations of the fiducial regions within the fields of these clusters

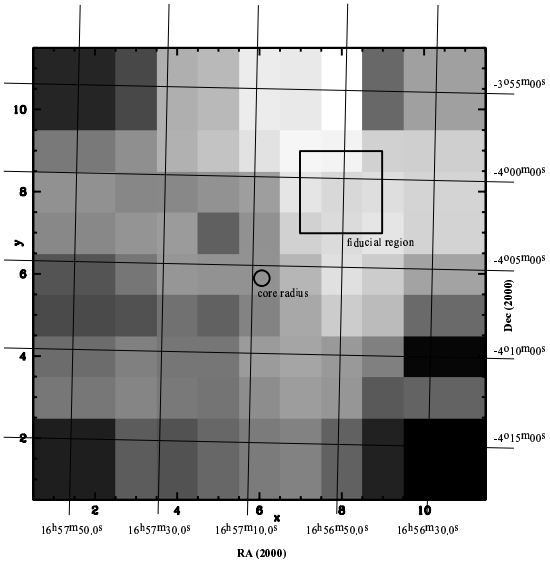

Figure 3.9 Extinction Map for M10. North is up, east is to the left. The size of the entire field is 25.9 arcmin on the side. The darker the color of a subregion, the more extinction is occurring in it (see Figure 3.11) relative to the fiducial region whose position is shown on the map along with the core radius around the location of the center of the cluster. The differential extinction in this Figure ranges from approximately -10 mmag to 150 mmag (dark colored region) relative to the fiducial region.The coordinate axes x and y correspond to the ones in Figure 3.11. The average reddening with respect to the fiducial region is $E_{V-I} = 68 \pm 41$ mmag for the entire field and $E_{V-I} = 49 \pm 28$ mmag for the inner part of the field (see Figure 3.11). The size of one pixel in this map ($\Delta x = 1$ or $\Delta y = 1$) is ~ 140 arcsec.

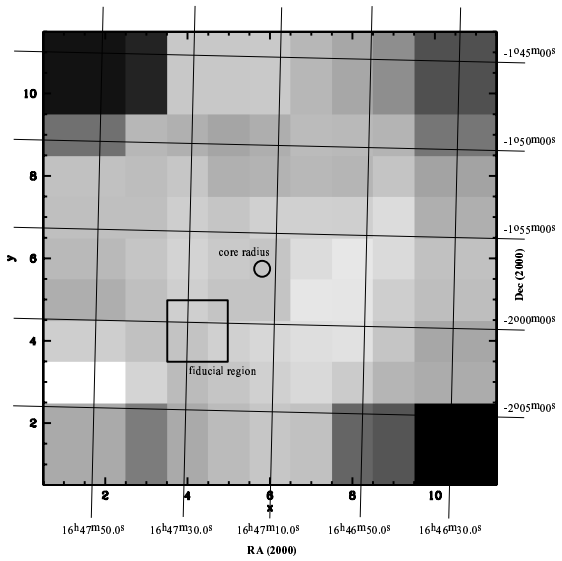

Figure 3.10 Extinction Map for M12. North is up, east is to the left. The size of the entire field is 25.9 arcmin on the side. The darker the color of a subregion, the more extinction is occurring in it (see Figure 3.12) relative to the fiducial region whose position is shown on the map along with the core radius around the location of the center of the cluster. The coordinate axes x and y correspond to the ones in Figure 3.12. The average reddening with respect to the fiducial region is $E_{V-I} = 40 \pm 58$ mmag for the entire field and $E_{V-I} = 9 \pm 15$ mmag for the inner part of the field where the errors are considerably smaller (see Figure 3.12) due to the higher stellar density. The size of one pixel in this map ($\Delta x = 1$ or $\Delta y = 1$) is ~ 140 arcsec.

from $\sim$ -20 to 190 mmag, relative to the fiducial region are shown as the top number in each of the pixels in the grids of Figures 3.11 and 3.12. The bottom number in each of the pixels corresponds to our error estimate for the corresponding E_{V-I} value (see Section 3.1.1 for a description of our error analysis). The location of the fiducial region is shown in grey in each of the two Figures. We further show the division between an outer "ring" of subregions and the inner part of the field. The inner subregions in each of the fields typically contain higher numbers of stars and have lower errors associated with them. The stellar density is especially low towards the corners of the fields. The average E_{V-I} for only the inner part of the field compared to the fiducial region is 49 ± 28 mmag for M10 and 9 ± 15 mmag for M12.

To illustrate the effects of our internal dereddening method, we show, in Figures 3.13 and 3.14, the CMDs before and after applying the extinction maps (differential

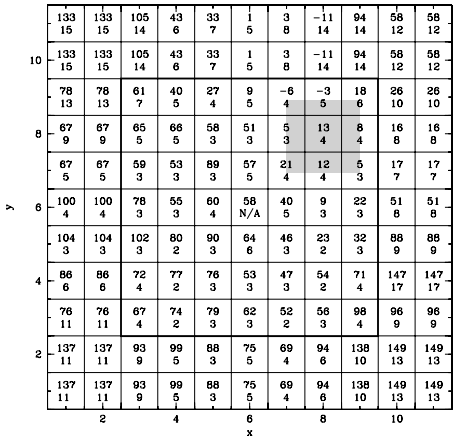

Figure 3.11 M10 – Differential E_{V-I} values (top number) with associated errors (bottom number) relative to the average E_{V-I} of the fiducial region (shown in grey for reference). Each pixel is about 140 arcsec on the side. The size and orientation of the field is the same as in Figure 3.9. The pixel in the map with an error value listed as N/A did not contain enough stars for a fit, due to saturation and crowding in the cluster center. Its E_{V-I} was obtained by interpolation from neighboring pixels. The average reddening with respect to the fiducial region is $E_{V-I} = 68 \pm 41$ mmag for the entire field and $E_{V-I} = 49 \pm 28$ mmag for the inner part, shown in the image. The subregions in this inner part carry higher significance due to the higher number of cluster stars they contain. To obtain a map of absolute E_{V-I} values, a reddening zero point has to be added to the pixel values. We discuss this zero point in Section 3.3.3. Finally, in order to get absolute values for E_{B-V}, one needs to multiply the absolute E_{V-I} value (i.e., including zero point) by 0.7273 (Schlegel et al. 1998).

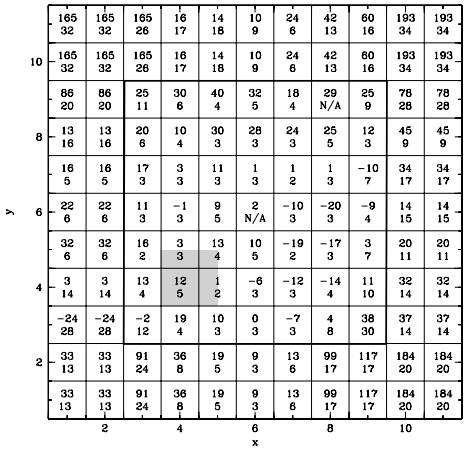

Figure 3.12 M12 – Differential E_{V-I} values (top number) with associated errors (bottom number) relative to the average E_{V-I} of the fiducial region (shown in grey for reference). Each pixel is about 140 arcsec on the side. The size and orientation of the field is the same as in Figure 3.10. The pixel in the map with an error value listed as N/A did not contain enough stars for a fit, due to saturation and crowding in the cluster center. Its E_{V-I} was obtained by interpolation from neighboring pixels. The average reddening with respect to the fiducial region is $E_{V-I} = 40 \pm 58$ mmag for the entire field and $E_{V-I} = 9 \pm 15$ mmag for the inner part (shown) of the field where the errors are smaller. To obtain a map of absolute E_{V-I} values, a reddening zero point has to be added to the pixel values. We discuss this zero point in Section 3.3.4. Finally, in order to get absolute values for E_{B-V}, one needs to multiply the absolute E_{V-I} value (i.e., including zero point) by 0.7273 (Schlegel et al. 1998).

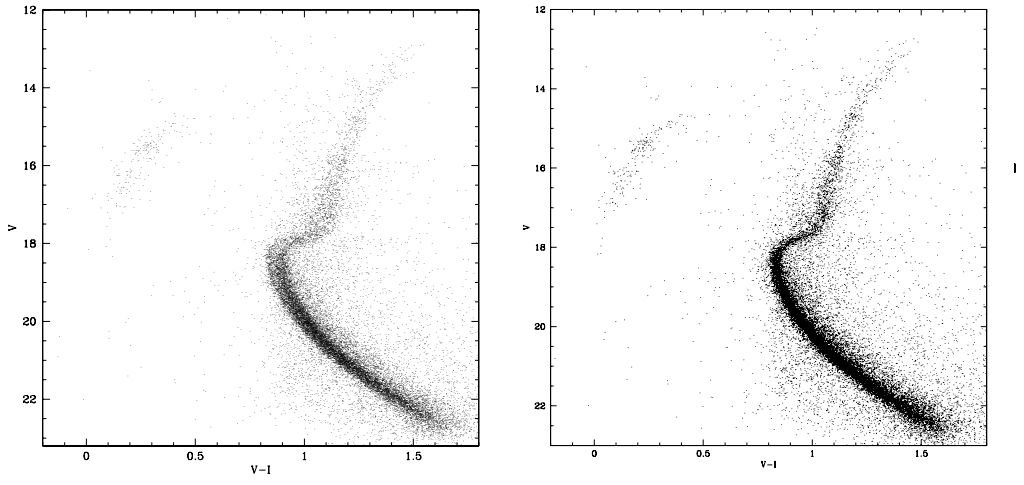

Figure 3.13 The raw and internally dereddened CMDs of M10. V and $V-I$ in the left plot indicate the location of the data points after the differential reddening with respect to the fiducial region was corrected for, i.e., after the inverse values of Fig. 3.11 were applied to the data of the right plot. No reddening zero point is applied to the data in this plot. The improvement of the appearance of the CMD is immediately obvious. The flaring of the data at $V \sim 17$ is most likely due to the low signal-to-noise of the 10s exposures at these magnitudes.

reddening correction) to the data. The data points are now all shifted to the CMD-location of the stars in the respective fiducial region, that is, no absolute reddening zero point has been applied. The improvement is clearly visible in both cases and especially obvious for M10. The width of its main sequence has, by applying the differential reddening map, decreased to a fraction of its former value. The SGB, RGB, and HB have become much more defined. Even M12's main sequence is significantly tighter after dereddening, and the scatter of the stars about its SGB and HB is much lower. In both differentially dereddened CMDs the small flaring of the data points at the faint end of the giant branch is most likely due to the low signal-to-noise of the 10s exposures at these magnitudes.

3.3 Determining the Reddening Zero Point

Thus far, our extinction values for the GCs are differential, that is, they show E_{V-I} with respect to a fiducial region in the respective cluster field. This fiducial region

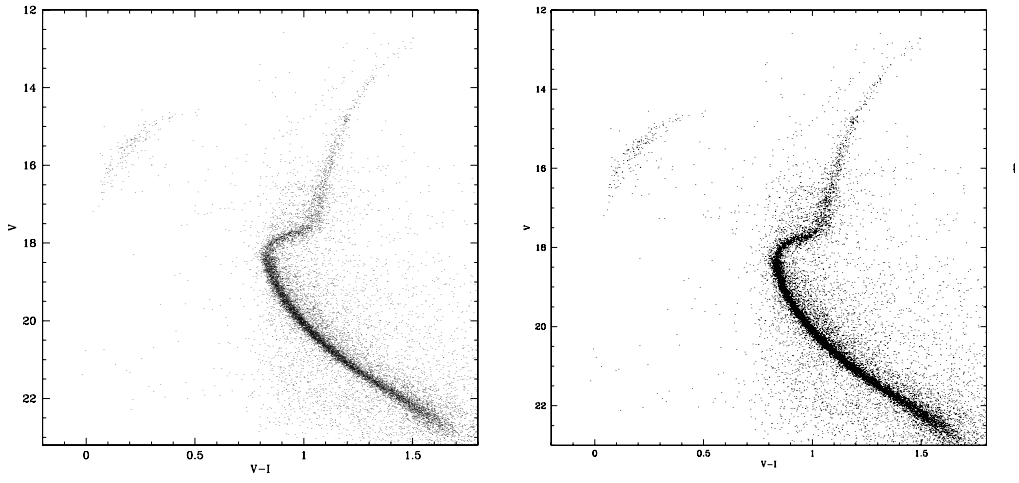

Figure 3.14 The raw and internally dereddened CMDs of M12. V and $V-I$ in the left plot indicate the location of the data points after the differential reddening with respect to the fiducial region was corrected for, i.e., after the inverse values of Fig. 3.12 were applied to the data in the right plot. No reddening zero point is applied to the data in this plot. Note the improvement of the appearance of the CMD. The flaring of the data at $V \sim 17$ is most likely due to the low signal-to-noise of the 10s exposures at these magnitudes.

itself suffers some mean interstellar extinction. In order to a) make our reddening maps useful tools, and b) determine intrinsic magnitudes and colors for binary system GC-member candidates, we need to determine this reddening zero point to add to our differential E_{V-I} values. This cannot be done using our data alone. We therefore had to use results from previous studies, as we describe below. We note that a direct comparison with literature values should be taken with caution since usually only a single numerical value for an average E_{V-I} is given whereas our result is a map of extinction across the field of the cluster.

3.3.1 Comparison to Previous Photometry Studies

To be able to use results from previous works for the calculation of our reddening zero points, an agreement between our photometry results and corresponding literature values is necessary. When comparing MSTO colors and magnitudes, however, one needs to consider that different parts of the GC fields are reddened by different amounts, as we show in our extinction maps (Figures 3.3, 3.9, and 3.10).

NGC 3201

For NGC 3201, we estimated our main-sequence turnoff V_{MSTO} magnitude to be 18.2 and the MSTO color $(V-I)_{MSTO}$ to be around 0.88 mag; both were determined by eye from the raw photometry CMD (Fig. 2.1).

These values were compared to the results of Rosenberg et al. (2000b, RB00b hereafter) and Covino & Ortolani (1997). RB00b find $V_{MSTO} \sim 18.2$ and $(V-I)_{MSTO} \sim 0.92$; both values are again determined by eye. Covino & Ortolani (1997) report $V_{MSTO} \sim 18.15$ and $(B-V)_{MSTO} \sim 0.65$ (tabulated). Using their reddening estimate of $E_{B-V} \sim 0.22$, the relations in Cardelli et al. (1989), and a set of isochrones provided by Don VandenBerg for $[Fe/H] = -1.41$ (VandenBerg 2000, private communication, based on evolutionary models by VandenBerg et al. 2000, hereafter VDB) the Covino & Ortolani (1997) value for $(V-I)_{MSTO}$ can be calculated to be approximately 0.93.

One discrepancy between our results and these literature values is therefore that our value for $(V-I)_{MSTO}$ is approximately 0.05 mag bluer than what is quoted by the authors mentioned above. The existence of variable reddening may be a likely explanation for this discrepancy, especially when one considers which part of the cluster was observed.

RB00b concentrate on the southern and eastern parts of the cluster for their longer exposures and the center of NGC 3201 for their shorter exposures. All of these three regions are, according to our reddening map (Fig. 3.3), regions of higher extinction with respect to our fiducial region.

Covino & Ortolani (1997) observe regions just to the north and west of the cluster center and the cluster center itself. While the north and west regions suffer only low reddening (Fig. 3.3), the area within ~ 7 arcmin to the north and west of the cluster

center is obscured by a smaller feature not visible in the SFD map (see Fig. 3.6). At least five of seven Covino & Ortolani (1997) fields are very likely affected by this dense obscuration feature.

While a quantitative (star-by-star) magnitude comparison between our data and the data obtained by RB00b and Covino & Ortolani (1997) is not possible, we conclude that their estimates for the MSTO color could very well be influenced by the fact that the regions they observed were subject to extinction somewhat higher than the average value over our field of view.

We note that these comparisons focus on the MSTO colors; the vertical nature of the MSTO makes it difficult to compare the V mag of the MSTO at sufficiently high precision.

M10 & M12

In our photometry we estimate the MSTO of M10 to be around $(V-I)_{MSTO} \sim 0.88$ & $V_{MSTO} \sim 18.5$ (Figure 2.2), and the one of M12 to be at $(V-I)_{MSTO} \sim 0.84$ & $V_{MSTO} \sim 18.35$ (Figure 2.3). Two recent VI studies present themselves as a means for photometry comparison: the extensive VI GC-CMD catalog of Rosenberg et al. (2000a, RB00a hereafter) and the HST study of M10, M22, and M55 of Piotto & Zoccali (1999, PZ99 hereafter). For M12, we find excellent agreement with RB00a for our photometry for both $(V-I)_{MSTO}$ and V_{MSTO}. For M10 our MSTO is slightly bluer and brighter than that of RB00a ($(V-I)_{MSTO} \sim 0.92$ & $V_{MSTO} \sim 18.6$). We attribute this to the fact that the region of M10 observed by RB00a lies to the East of the cluster center where we find higher differential extinction compared to the rest of the cluster field (see Section 3.2.2, and Figs. 3.9 and 3.11). Plotting our data which fall into the R00a field results in a location of the MSTO within 0.02 mags of the R00a MSTO, which approaches the limits of the rms of the photometry.

The agreement between our M10 results and the HST photometry of PZ99, however, is not as good since their MSTO is at $(V-I)_{MSTO} > 1$. As one can see in Figure 2.2, the range in our data does not extend to values redder than $(V-I)_{MSTO} \sim 0.95$. Since a direct star-by-star comparison between our data and PZ99 is not possible, we cannot give a good explanation for this discrepancy. One possible reason, however, might be a zero point drift in the HST photometry which has been noticed in studies such as Gallart et al. (1999), especially since PZ99's photometry zero point is based on HST data.

In addition, we compared our MSTO magnitude to two BV studies of M10 (Hurley et al. 1989) and M12 (Sato et al. 1989). The V_{MSTO} for both M10 and M12 is estimated to be at 18.4, in good agreement with our results.

3.3.2 NGC 3201

Isochrone Fitting

The most straightforward method of determining the extinction zero point is fitting isochrones to our differentially dereddened data. Thus, the obtained E_{V-I} corresponds to the reddening zero point to add to the differential E_{V-I}-values (von Braun & Mateo 2001). Simultaneously fitting age, distance, and reddening to the aforementioned set of VDB isochrones for NGC 3201 produced the fit shown in Fig. 3.15. It should be noted that since the point of this work is outlining our dereddening method as well as creating an extinction map for NGC 3201, we only performed some basic isochrone fitting here. For an estimate of [Fe/H], we adopted the isochrone with metallicity closest to the Gonzalez & Wallerstein (1998) value of –1.42.

For the fit of Fig. 3.15, [Fe/H] = –1.41, $d \sim 4.5$ kpc, age = 18 Gyrs, and the E_{V-I} zero point to be added to the values in Fig. 3.4 is 0.15 mag. The value for the distance is slightly below the one quoted by Harris (1996), but fairly close to

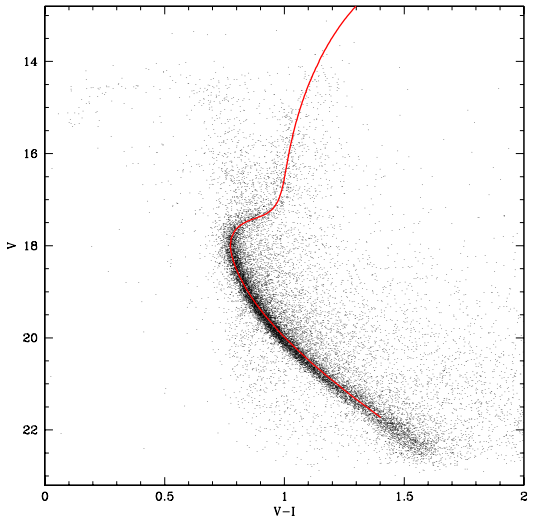

Figure 3.15 The best fit to our differentially dereddened NGC 3201 data produced by the VDB isochrones. For this fit, [Fe/H] = –1.41, $d \sim 4.5$ kpc, age = 18 Gyrs, and the reddening zero point $E_{V-I} \sim 0.15$ to be added to the values in Fig. 3.4. The average E_{V-I} for the cluster is approximately 0.24 in this plot.

the two values derived using slightly different methods by Covino & Ortolani (1997). When adding the mean E_{V-I} of our reddening map (86 mmag) to the zero point, the average E_{V-I} for the cluster is approximately 0.24, which is slightly below the estimates of, e.g., Cacciari (1984), Harris (1996) and RB00b whose $E_{V-I} \sim 0.285$.

The age is higher than some other calculated GC ages (Vandenberg et al. 1996, see also Chapter I) and the commonly accepted expansion age of the universe (14 Gyrs, see Chapter I), but the 18 Gyr isochrones produced by far the best fits, even when [Fe/H] and the distance were modified. The strongest effect on the shape of the isochrone when varying the age is a decrease in color-distance (i.e., distance along the horizontal color axis) between the MSTO and the base of the RGB for higher ages. Since none of the other variable parameters (distance, metallicity, and reddening) has any influence on this color-distance, any VDB isochrone of younger ages simply does not trace out the loci of the datapoints as well as the 18 Gyrs one (we show an example of 12 Gyrs and 14 Gyrs isochrones in Figure 3.16).

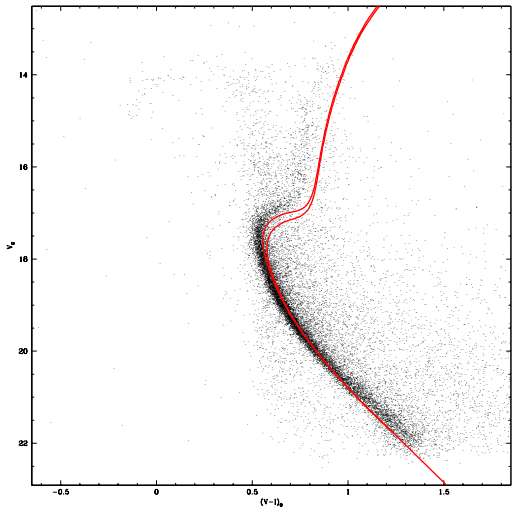

Figure 3.16 The NGC 3201 data, dereddened to the value of $E_{V-I} = 0.285$ (Harris 1996) (with differential reddening correction), plus the isochrones for ages of 12 (top) and 14 (bottom) Gyrs with values of [Fe/H] = –1.54 (closest value to Harris' –1.58) and d = 5.2 kpc. The agreement between data and fit is better in Fig. 3.15.

In order to justify our choice of isochrone parameters and to eliminate the possibility of multiple factors conspiring against us in the attempt to find a good isochrone fit to the data, we illustrate in Fig. 3.16 what the CMD would look like if we were to strictly adopt literature values from Harris (1996) ([Fe/H]=–1.58, $E_{V-I} = 0.289$, d = 5.2 kpc). Plotted are a pair of isochrones with respective ages 12 and 14 Gyrs on top of the data[4]. The agreement between data and fit is not as good as in Fig. 3.15.

Using SFD Maps

A second option in the determination of the reddening zero point is to simply calculate the average offset between our maps and the SFD dust maps. If the two maps trace out similar dust features, the offset between the maps should approximately be constant everywhere in the field. This average offset then corresponds

[4]In order to have a valid basis for comparison, we needed to apply an E_{V-I} zero point of $0.289 - 0.086 = 0.203$ to the differentially dereddened data, where 0.289 is the Harris (1996) E_{V-I} value and 0.086 is the mean E_{V-I} value of our extinction map.

to the estimate of the reddening zero point based on the comparison between our extinction maps and the SFD maps (based on dust emissivity).

As stated in Section 3.2.1, the mean E_{V-I} of the difference map between the SFD and our data is 250 ± 46 mmag. The average E_{V-I} value for this difference map corresponds to the E_{V-I} zero point to add to our data to obtain absolute reddening values.

Calculating the total reddening in this fashion gives $E_{V-I} \sim 0.34$ which is significantly higher than the literature values. We show a fit to the NGC 3201 data using a VDB isochrone with [Fe/H] = –2.31 (isochrones with higher metallicities failed to reach the MSTO color which is, as a results of the dereddening, too blue). The age of the isochrone shown is 16 Gyrs (younger isochrones were even farther away from the SGB as this 16 Gyr one, and the 18 Gyr isochrone was too red to reach the MSTO color), $V_0 - M_V = 13.3$, and the E_{V-I} zero point is 0.25. The isochrone does not reproduce the data as well the one shown in Figure 3.15.

Using RR Lyrae Stars

Another method of attempting to find a reddening zero point is to simply adopt one from the literature and model the resulting dereddened data with a set of isochrones. Here, we took the Cacciari (1984) value of $E_{V-I} \sim 0.285$ which she calculated using RR Lyrae stars. Since this corresponds to the average reddening for the whole cluster, we had to subtract the mean E_{V-I} of her RR Lyrae stars (in our field of view) with respect to our fiducial region. This value turned out to be 70 mmag.

We failed, however, to find a good isochrone fit to the thus dereddened data, as is shown in Fig. 3.18. In order to get the MSTO points of the data and the isochrone to agree, we had to lower [Fe/H] to –2.01, a value quite a bit below literature values

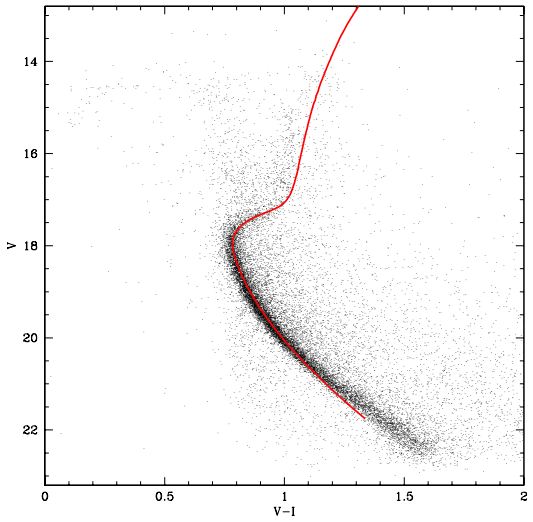

Figure 3.17 The NGC 3201 data when assuming a zero point of E_{V-I} = 0.24 mag, obtained by calculating the average offset between our extinction map (Figure 3.3) and the corresponding SFD map (Figure 3.6). For this isochrone, age = 16 Gyrs, $V_0 - M_V$ = 13.3, and [Fe/H] = –2.31 (significantly below literature values for this cluster, see Gonzalez & Wallerstein 1998). The isochrone fails to provide a fit better than in the one in Figure 3.15.

such as –1.41 (Gonzalez & Wallerstein 1998) or –1.58 (Harris 1996). The distance modulus here is 13.4, and the age 14 Gyrs. As one can easily see, the fit fails to hit the SGB due to the "young" isochrone age of 14 Gyrs. Older age isochrones could not be shifted far enough toward the dereddened MSTO location to produce a fit, even when the metallicity was lowered to the lowest available value of –2.31.

3.3.3 M10

Isochrone Fitting

The VDB isochrone fit for M10, shown in Figure 3.19, was obtained using the following parameters: [Fe/H] = –1.54[5], age = 16 Gyrs, d = 5.1 kpc ($V_0 - M_V$ = 13.55), and the E_{V-I} zero point, to which any differential extinction has to be added, is 230 mmag. All shapes of the CMD features are well traced out by the VDB isochrone. The 16 Gyr isochrone produced a slightly better fit than the 18 Gyr one, but from

[5]For an estimate of [Fe/H], we used isochrones with values of [Fe/H] ranging from –1.14 to –2.31, straddling M10's [Fe/H] value of –1.52 (Harris 1996).

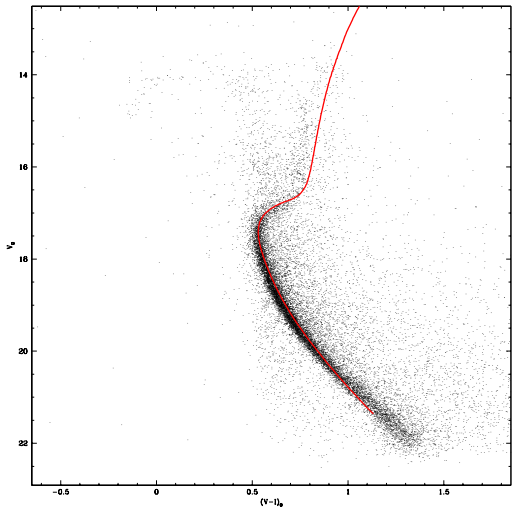

Figure 3.18 The fit to the differentially dereddened data using a E_{V-I} zero point of 0.21 from Cacciari's (1984) RR Lyraes, and applying our reddening map. [Fe/H]=-2.01 (much lower than literature values), age = 14 Gyrs, and $V_0 - M_V = 13.4$. As one can see, the fit fails to reproduce the loci of the datapoints. We therefore conclude that the reddening zero point of Fig. 3.15 is correct.

the appearance of the CMD, it seems that perhaps a 17 Gyr VDB isochrone, if it were available, would produce an even better fit than the one shown here. The value for [Fe/H] is similar to the Harris (1996) one of –1.52, whereas our distance estimate of 5.1 kpc is slightly higher (4.4 kpc; Harris 1996).

Using SFD Maps

We show the pixel-interpolated SFD maps of our field of view of M10 in Figure 3.20. The orientation and field size of Figure 3.20 are identical to Figure 3.9. As before, darker regions correspond to regions of higher extinction. We added the location of the fiducial region for reference. For M10, the average reddening of the SFD map is $E_{V-I} = 387 \pm 17$ mmag for the whole field and 389 ± 16 mmag for the inner region (see Figure 3.11). Note that these numbers are estimates for the full extinction along the line of sight, i.e., they contain a reddening zero point. The SFD estimates agree well with Harris (1996) who quotes an average $E_{V-I} = 382$ mmag

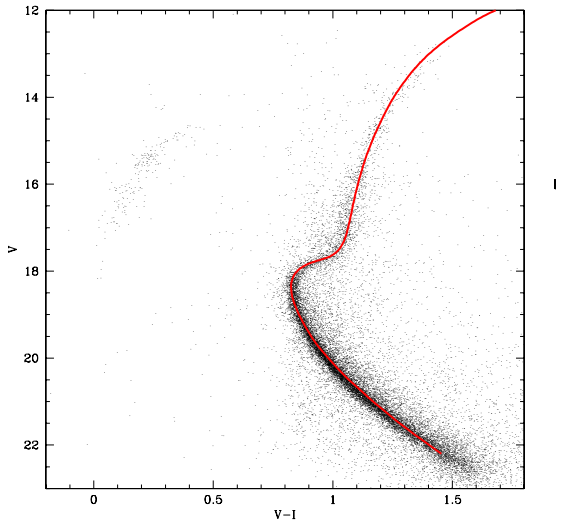

Figure 3.19 Differentially dereddened CMD of M10 with overlain VDB best-fit isochrone. For this fit: [Fe/H] = –1.54, age = 16 Gyrs, d = 5.1 kpc ($V_0 - M_V = 13.55$), and the E_{V-I} zero point, to which any differential extinction has to be added, is 0.23. All CMD features are well traced out by the VDB isochrone. The 16 Gyr isochrone produced the better fit than the 18 Gyr one, but from the appearance of the CMD, it seems that perhaps a 17 Gyr VDB isochrone, if it were available, would produce an even better fit than the one shown here.

for M10.

As a first step in the calculation of the average offset between the two independent reddening estimates, we subtracted our extinction maps from the SFD maps of the corresponding regions. The resulting image is shown in Figure 3.21. Again, darker regions correspond to areas where our map indicate more differential extinction (relative to the fiducial region) than the corresponding SFD map. We show the locations of the fiducial regions as well as the border between inner and outer regions (see above) for reference.

The difference map for M10 (Figure 3.21) indicates that our extinction map and the SFD map for M10 spatially agree quite well, particularly in the inner region of the image which basically shows no residual features at all. The determination of the differential extinction towards the edges of the map is less precise due to the lower number of cluster stars in these regions (see Figure 3.11) and thus appears more

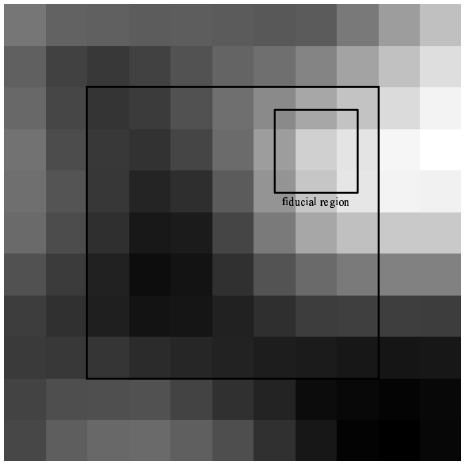

Figure 3.20 Graphical Representation of the SFD Map in the region of M10. The location of the fiducial region is given for reference. Orientation, size, and pixel sizes are the same as in Figures 3.9 and 3.11. Darker regions correspond to higher extinction. The extinction ranges from $E_{V-I} = 344$ to 411 mmag. The average reddening is $E_{V-I} = 387 \pm 17$ mmag for the entire field and $E_{V-I} = 389 \pm 16$ mmag for the inner part of the field.

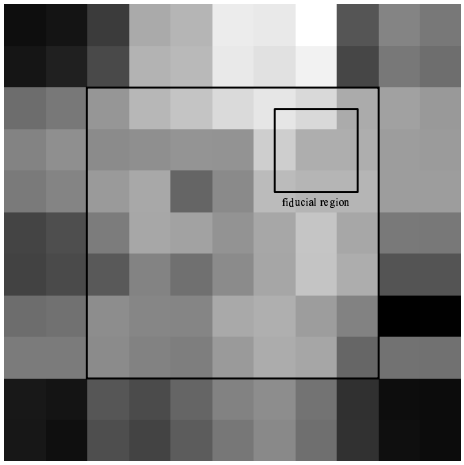

Figure 3.21 Graphical Representation of the difference between our extinction map for M10 (Fig. 3.9) and the SFD Map of the same region (Fig. 3.20) . The location of the fiducial region is given for reference; the orientation, size, and pixel sizes are the same as in Figures 3.9 and 3.11. Darker regions correspond to areas where our maps indicate more differential extinction (relative to the fiducial region) than the SFD map. It is obvious that the especially the inner region is featureless, indicating good spatial agreement between the two maps. The pixels toward the edges of the map contain fewer cluster stars causing any calculated differential reddening to have a higher associated rms error which results in the "noisy" appearance of the ring around the inner region. The average reddening of the whole field is $E_{V-I} = 319 \pm 35$ mmag and $E_{V-I} = 340 \pm 14$ mmag for the inner region.

noisy. The average reddening of the whole field of Figure 3.21 (the difference map) is $E_{V-I} = 319 \pm 35$ mmag, whereas for only its inner region, it is $E_{V-I} = 340 \pm 14$ mmag. It is worth noting that for the inner region, the rms of this difference map of 14 mmag is smaller than the rms of both our extinction map (28 mmag; see Figure 3.9) and the SFD map for M10 (16 mmag; see Figure 3.20), indicating that the features traced out by both maps are correlated. 340 mmag thus corresponds to our estimate for the reddening zero point as determined by using the SFD maps. We were unable, however, to produce an isochrone which produced a fit to our data using this estimate of E_{V-I}, even when widely varying the values for distance, age, and [Fe/H] (see Section 3.3.5 for discussion; we also show the equivalent of this attempt for NGC 3201 in Figure 3.17). We therefore adopt our estimate of 230 mmag, as determined by the VDB isochrones, as the reddening zero point for M10 (see above).

3.3.4 M12

Isochrone Fitting

Since the features of M12's undereddened CMD (Fig. 3.14) are very similar to the ones found in the CMD of M10 (Fig. 3.13), apart from the much smaller effects of differential reddening, it is no surprise that the parameters for the VDB isochrone fit shown in Figure 3.22 are almost identical to the ones used for M10: [Fe/H] = –1.54[6], age = 16 Gyrs, d = 4.9 kpc ($V_0 - M_V = 13.46$), and the E_{V-I} zero point is 240 mmag. Again all features of the CMD, including the SGB and the RGB, are very well traced out. The only minor deviation between the loci of the data points and the isochrone fit occurs at $V \sim 21.5$. The above isochrone parameters agree very well with the values for M12 in Harris (1996).

[6]We used the same range of [Fe/H] as for M10.

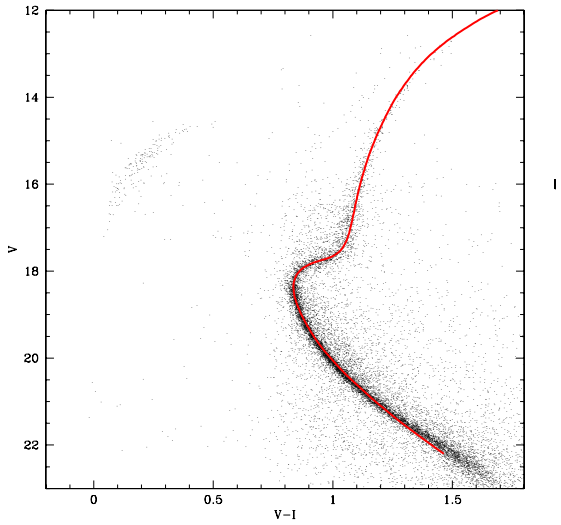

Figure 3.22 Differentially dereddened CMD of M12 with overlain VDB best-fit isochrone. For this fit: [Fe/H] = –1.54, age = 16 Gyrs, d = 4.9 kpc ($V_0 - M_V = 13.46$), and the E_{V-I} zero point is 0.24. All features of the CMD, including the SGB and the RGB, are very well traced out. The only minor deviation between the loci of the data points and the isochrone fit occurs at $V \sim 21.5$. The above isochrone parameters agree very well with the values for M12 in Harris (1996) and the SFD E_{V-I} estimates for this region.

Using SFD Maps

The pixel-interpolated SFD maps of our field of view of M12 is shown in Figure 3.23. Its orientation and field size are the same as in Figure 3.10. Darker regions correspond to regions of higher extinction. We added the location of the fiducial region for reference. The average reddening for M12, according to the SFD maps, is $E_{V-I} = 254 \pm 8$ mmag for the whole field and 250 ± 7 mmag for the inner region, including the reddening zero point. These SFD numbers agree well with the Harris (1996) average $E_{V-I} = 258$ mmag for M12.

Similar to M10, the two maps for M12 (Figures 3.10 and 3.23) agree well, resulting in a difference image (Figure 3.24) which is featureless except in the regions towards the corner of the image. The average reddening of the entire difference map (Figure 3.24) is $E_{V-I} = 214 \pm 53$ mmag, whereas for only its inner region, it is $E_{V-I} = 241 \pm 11$ mmag. 11 mmag as the rms is comparable to the rms of the SFD map (7 mmag;

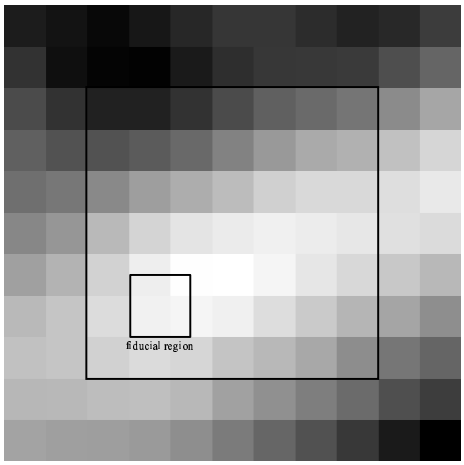

Figure 3.23 Graphical Representation of the SFD Map in the region of M12. The location of the fiducial region is given for reference. Orientation, size, and pixel sizes are the same as in Figures 3.10 and 3.12. Darker regions correspond to higher extinction. The extinction ranges from $E_{V-I} = 241$ to 271 mmag. The average reddening is $E_{V-I} = 254 \pm 8$ mmag for the entire field and $E_{V-I} = 250 \pm 7$ mmag for the inner part of the field.

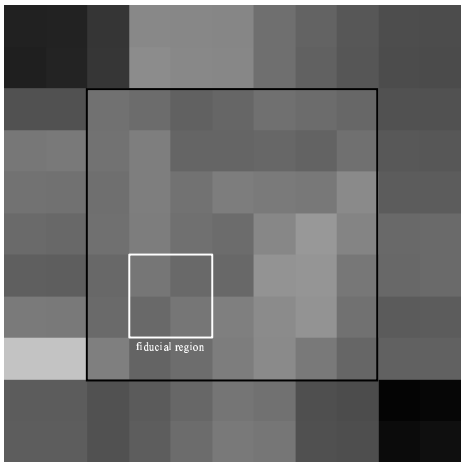

Figure 3.24 Graphical Representation of the difference between our extinction map for M12 (Fig. 3.10) and the SFD Map of the same region (Fig. 3.23 . The location of the fiducial region is given for reference, the orientation, size, and pixel sizes are the same as in Figures 3.10 and 3.12. Darker regions correspond to areas where our map indicates more differential extinction (relative to the fiducial region) than the SFD map. The difference map is featureless except in the regions towards the corner of the image which is evidence for the good spatial agreement between the two maps. The average reddening of the whole field is $E_{V-I} = 214 \pm 53$ mmag, whereas for only the inner region, it is $E_{V-I} = 241 \pm 11$ mmag.

Table 3.1. Selected Recent Average E_{V-I} Estimates for NGC 3201

E_{V-I}	Reference	Method
285 mmag	Cacciari (1984)	RR Lyrae colors
285 mmag	Harris (1996)	compilation of selected previous results
336 mmag[a]	Schlegel et al. (1998)	dust IR emissivity maps
240 mmag	this work & von Braun & Mateo (2001)	VDB isochrone fitting

[a]This value also corresponds to our estimate using the SFD maps.

Note. — All listed literature reddening estimates were obtained by converting E_{B-V} values to E_{V-I} by using $E_{B-V} = 0.7273 \times E_{V-I}$ and a $R_V = 3.1$ reddening law (Schlegel et al. 1998, $\lambda_{central} \sim 8100$ Å). They represent the updated values from BM01 where we calculated $E_{B-V} = 0.6468 \times E_{V-I}$, based on Cardelli et al. (1989, $\lambda_{central} \sim 9000$ Å).

see Figure 3.23) and lower than the rms for our extinction map (13 mmag; see Figure 3.10), again indicating positive correlation between the features present in both maps. We calculate 241 mmag to be our estimate for the reddening zero point as determined by using the SFD maps. This value agrees very well with our results from the VDB isochrone fitting method (240 mmag; see above).

3.3.5 Comments on the Adopted Reddening Zero Points

NGC 3201

Given that we were not able to produce a fit to our NGC 3201 data using the VDB isochrones when we calculated the reddening zero point using either the SFD maps or the Cacciari (1984) RR Lyrae stars, we conclude that our best estimate for the E_{V-I} zero point is 0.15 mag, giving an average $E_{V-I} \sim 0.24$ for the cluster as a whole. This value falls approximately 1σ below the estimate by Cacciari (1984) and the value tabulated by Harris (1996). We show our results, along with some literature estimates for E_{V-I} for NGC 3201, in Table 3.1. All E_{V-I} values in Table 3.1 are calculated by multiplying E_{B-V} by 0.7273 to obtain E_{V-I} (Schlegel et al. 1998).

We could force our reddening zero point to agree with these past results by applying a systematic shift to our I magnitudes of 0.08 to brighter values which would

give a distance to NGC 3201 of 4.8 kpc. We have, however, no reason to adopt such a shift. The transformations to standard magnitudes as well as the application of the aperture corrections underwent repeated thorough examinations and appear to be correct. Since no other indication throughout our data reduction and analysis suggests a systematic error in the I band magnitudes, either, we simply cannot justify adjusting our I magnitudes in order to compensate for the 1σ effect described above.

As we mentioned in Section 3.1.2, we changed the value for the slope of the reddening vector from $A_V/E_{V-I} = 1.919$ for NGC 3201, based on Cardelli et al. (1989), to 2.411 for M10 and M12, based on Schlegel et al. (1998). The central wavelength for the I filter used to establish the Cardelli et al. (1989) conversions is 9000 Å, whereas the filter used for the SFD conversions peaks closer to 8100 Å. Any instrumental I magnitude will suffer higher extinction with shorter I filter central wavelengths. Since reddening is not calculated until after the transformation to standard magnitudes is performed, the slope of the reddening vector has to be chosen according to the characteristics of the I filter. The I filter used during the LCO 1998 observing run has a central wavelength around 8200 Å, closer to the one used in SFD.

A re-calculation of the reddening maps based on this "new" slope, however, produced results which were identical to the previously calculated ones. The values in the individual pixels of the extinction map grid (such as in figure 3.11 and 3.12) changed by only a few mmag as a results of the change in slope. Similarly, refitted isochrones produced an identical reddening zero point. We therefore conclude that our reddening results for NGC 3201 do not change as a result of this change in slope of the reddening vector.

Table 3.2. Selected Recent Average E_{V-I} Estimates for M10

E_{V-I}	Reference	Method
214 mmag	Burstein & Heiles (1982)	HI/galaxy count maps
426 mmag	Reed et al. (1988)	integrated light
371 mmag	Hurley et al. (1989)	UBV 2-color diagram
234 mmag	Arribas et al. (1990)	infrared photometry
382 mmag	Harris (1996)	compilation of selected previous results
389 mmag[a]	Schlegel et al. (1998)	dust IR emissivity maps
279 mmag	this work & von Braun et al. (2002)	VDB isochrone fitting

[a]This value also corresponds to our estimate using the SFD maps.

Note. — All listed literature reddening estimates were obtained by converting E_{B-V} values to E_{V-I} by using $E_{B-V} = 0.7273 \times E_{V-I}$ and a $R_V = 3.1$ reddening law (Schlegel et al. 1998).

Table 3.3. Selected Recent Average E_{V-I} Estimates for M12

E_{V-I}	Reference	Method
127 mmag	Burstein & Heiles (1982)	HI/galaxy count maps
317 mmag	Sato et al. (1989)	UBV 2-color diagram
258 mmag	Harris (1996)	compilation of selected previous results
250 mmag[a]	Schlegel et al. (1998)	dust IR emissivity maps
249 mmag	this work & von Braun et al. (2002)	VDB isochrone fitting

[a]This value also corresponds to our estimate using the SFD maps.

Note. — All listed literature reddening estimates were obtained by converting E_{B-V} values to E_{V-I} by using $E_{B-V} = 0.7273 \times E_{V-I}$ and a $R_V = 3.1$ reddening law (Schlegel et al. 1998).

M10 & M12

The two independent estimates we obtain for an average E_{V-I} (zero point plus differential) for each cluster are 389 mmag (by adding the SFD zero point to the average level of our extinction map) and 279 mmag (by using the VDB isochrone) for M10, as well as 250 mmag (using SFD zero point) and 249 mmag (VDB isochrone) for M12. The reddening estimates in the literature for the two clusters vary more for M10 than for M12. These result, along with some recent literature E_{V-I} values for M10 are presented in Table 3.2, and for M12 in Table 3.3. As for NGC 3201, it should be noted that all the literature values in Table 3.2 & 3.3 were obtained by converting their cited E_{B-V} values to E_{V-I} by using $E_{B-V} = 0.7273 \times E_{V-I}$ and an $R_V = 3.1$ reddening law (Schlegel et al. 1998).

As mentioned above we were not able to fit an isochrone to our data using the SFD reddening zero point for M10, even when lowering the metallicity to –2.31 (limit of the isochrones) and changing the values for the age of the isochrone or the distance of the cluster. In order to avoid the possibility of multiple factors conspiring against us (such as incorrect aperture corrections and/or calibration zero points), we compared our DoPHOT photometry results for 10 isolated stars (no close neighbors) with IRAF's qphot magnitudes for the same stars. Within rms photometry errors, the results were identical, such that we found an average offset between $I_{DoPHOT} - I_{qphot} \sim 0.034$ and $V_{DoPHOT} - V_{qphot} \sim 0.005$.

We will therefore adopt 230 mmag as the reddening zero point for M10. Compared to literature values, we are thus below the SFD, Hurley et al. (1989), and Harris (1996) estimates, and slightly above the values in Burstein & Heiles (1982) and Arribas et al. (1990). For M12, our reddening estimate agrees very well with the SFD and Harris (1996) values, but is slighter higher than the Burstein & Heiles (1982) and slightly lower than the Sato et al. (1989) estimates.

The similarity in E_{V-I} between the clusters may be somewhat unexpected due to the strong presence of differential reddening across the field of M10 but not M12. On the other hand, the morphologies of the two observed (undereddened) CMDs of the clusters are extremely similar to each other (confirmed also in Hurley et al. 1989; Sato et al. 1989, and RB00a). Given the small difference between the values of [Fe/H] for M10 and M12, it therefore appears quite sensible that the estimates for age, distance, and reddening should be very similar for the two GCs.

CHAPTER IV

The Search for Variable Stars

The contents of the databases containing the photometry data for the detection of binary stars in the three clusters as well as determining their periods is summarized in Table 4.1 (von Braun & Mateo 2002; von Braun et al. 2002). They represent the starting point in our search for binary stars in these clusters. Our data are sensitive to variables as bright as $V \sim 16.5$, slightly brighter than the previously mentioned division between 600s and 10s data in the CMDs, since observing conditions and CCD quantum efficiencies may vary between epochs or observing runs. Finally, we note that the variability detection and the period determination of variable stars are entirely independent of the differential dereddening described in Chapter III.

4.1 Variability Detection

The criteria we set in order to extract variable star candidates from the list of stars in our database were the following:

Table 4.1. Epochs Used for Binary Detection and Period Determination

Cluster	Total Epochs in Each Filter	Average Number of Stars per Image
NGC 3201	130	27000
M10	70	20000
M12	100	14000

1. χ^2 per degree of freedom, calculated based on the assumption that every star is a non-variable, has to be greater than 3.0. We furthermore set a $\sigma > 0.05$ mag threshold for a star to be taken into consideration as a variable candidate, where σ represents the variability in the lightcurve.

2. The star under investigation must appear in at least 75% of the epochs for NGC 3201, and in at least 40% of the epochs in M10 and M12. The reason why this number is considerably lower for M10 and M12 is that the MDM data, which comprise a large fraction of the total epochs (see Table 2.1) were taken with CCDs with smaller fields than the LCO data.

3. The detected variability should not be due to only a few outliers (3-5% of the datapoints) causing the high χ^2. Care was taken to avoid deleting possible eclipsing systems at this stage (see below).

4. The star under investigation should display a brightness variation in both filters, and the variability signal should be correlated in both filters (this algorithm is very similar to the one described in Welch & Stetson 1993; Stetson 1996).

Any measurement of stellar magnitude was weighted by the square of the inverse photometric error associated with it.

One type of binary star system, however, might be prone to being deleted during step 3. A detached system with a period long enough so that eclipses are not very well sampled might show up as a system whose χ^2 is based solely on a few outliers. In order to ensure that we would not miss such a system, we developed a slightly modified set of criteria specifically aimed at detecting detached binary star systems with the basic idea to identify faint "outliers" which fall next to each other in time.

1. As a first step, the mean magnitude plus standard deviation of the brightest

75% of the datapoints are calculated.

2. We now try to detect successive (in time) datapoints which are nσ fainter than this mean magnitude. The choice of n depends on the quality of the photometry of the star in question and the number of datapoints for the star.

3. If the i-th datapoint falls within Δt of datapoint $i-1$ (where i indicates succession in time), a merit function is calculated whose value would be $\delta_i \times \delta_{i-1}$. δ_i is defined as the magnitude difference between the i-th datapoint and the average magnitude of the 75% of the brightest stars, divided by the standard deviation (see step 1). Δt is dependent on the observing strategy followed to detect the binaries (i.e., it would be shorter, perhaps up to an hour, for a strategy where the cluster is observed many times in succession, and longer, perhaps several hours, if the cluster is observed only once every so often). It is obvious that for more than two neighboring faint outliers, the merit function would rapidly increase in value.

4. Candidates for detached systems are selected based on the value of their merit functions.

The application of this algorithm to our data revealed the existence of one detached system in our field-of-view of NGC 3201 (V12; see Section 5.1 and Figure 5.6) which had been eliminated by application of criteria described at the beginning of this Section.

We note that we did not systematically address the issue of completeness in our analysis. The choice of parameters for the steps outlined above was made mainly based on hindsight (e.g., all of our candidates' χ^2 values are well in excess of 100[1])

[1]Reasons for high χ^2 values of non-variable stars are very low signal and crowding.

or trial and error (e.g., the analysis of a set of phased lightcurves before and after a reduction criterion was applied). Any assessment of incompleteness due to other effects, such as period, phase, or duty cycle, is difficult to make as it sensitively depends on the windowing function created by the times of the observational epochs. If the period of a variable star is less than about an hour or higher than 5 days, we will most likely not detect the system since our exposure times are 600s long and observing runs generally last between one and two weeks. If the phase is such that the variable will only undergo changes in its brightness during the daytime, we will obviously also not find it. Very low duty cycles make it hard to detect the variable since it spends so little time in an eclipse and otherwise appears as a non-variable star. The lower the duty cycle, the more likely it is that a combination between the windowing function and the phasing of the binary would cause us to not detect it. However, the timing of our observing should enable us to find all variables with a period of up to around a day with fairly high duty cycles (30% or higher) since we perform repeated observations of the same cluster over the course of hours throughout many nights (especially for NGC 3201).

4.2 Period Determination

The final decision as to whether a star is a true variable candidate (and if so, what kind of variable star it is) was based on the inspection of the data phased by the correct period (the photometry lightcurve). A variety of algorithms to determine periods are used in astronomy, many of which are based on similar principles. Generally, a test statistic is defined as a function of the observations (random variables), and of a trial period (parameter of the statistic) by which the real-time observations are folded. For each trial period and a given set of observations the test statis-

tic returns a single number. One may therefore plot the value of the test statistic against trial period (or its corresponding frequency) in what is called a periodogram (Schwarzenberg-Czerny 1989). Periodic oscillations in the observations will show up as features (resembling spectral lines) in the periodogram.

The initial estimates of the periods of all our variable star candidates which survived the steps outlined in the previous Subsection were determined by two independent algorithms:

- the minimum-string-length (MSL) method, based on a technique by Lafler & Kinman (1965) and described in Stetson (1996). The test statistic in this method is the length of a hypothetical piece of string connecting consecutive data points in a magnitude vs phase plot. For an incorrect period estimate, the data points will most likely be scattered, resulting in a long string length. When the trial period is very close to the true period, however, the string length will be short since any two data points consecutive in phase will be very close to each other in magnitude.

- the Analysis of Variance (AoV) method, described in detail in Schwarzenberg-Czerny (1989)[2]. The basic code for this algorithm was supplied to us by Andrzej Udalski (private communication, 1998). For this method, the entire dataset is folded by a test period and then divided into bins in phase. The test statistic is the ratio of two variances. The numerator is the variance of the averages of the bins about the mean of the entire dataset, which obviously is high if a star is a variable. The denominator is the sum of variances within the individual bins, which is small if the test period is the correct period. For a pure noise signal, this ratio (the AoV statistic) is 1. For a periodic signal its value is small for

[2]This method is quite similar to the Phase Dispersion Minimization (PDM) method

incorrect trial periods and large for the correct trial period.

A final tweaking of the precision in the period for a candidate was then done by hand whenever necessary, based on the appearance of the lightcurve.

4.3 Distance Determination

As explained in Chapter I, distances to binary systems can generally only be determined by using a combination of photometric and spectroscopic data. There is, however, one kind of binary system, the so-called W Ursa Majoris (W UMa) system, whose physical properties allow its distance to be determined. The only empirically fitted parameter in the determination of the absolute magnitude (and thus distance) of the binary system under investigation is the zero point of the relation. We discuss this distance determination method in the following Subsection.

The pulsating variables we detect in the cluster fields allow the use of empirically determined methods to determine their distances based on their periods and metallicities. We note that our observations are not sensitive to GC-member pulsating variables (such as RR Lyrae stars) as they are all saturated in our data.

4.3.1 Rucinski Absolute Magnitudes for W UMa Binaries

W Ursa Majoris binaries are systems in which the two components are in physical contact with their Roche equipotential lobes and at their inner Langrangian Point (see Mateo 1993; Rucinski 1985, for more detailed descriptions of W UMa systems). The fact that the total brightness of the system is constantly changing by up to $\sim$0.75 magnitudes makes them easy to detect. Due to the good thermal contact between the two components, the two stars have similar surface temperatures. The total luminosity of the system can therefore be defined as (Rucinski 1995; Mateo

1996)

$$L = K\,T^4\,S(q,P,f)\,M_p^{\frac{2}{3}}\,(1+q)^{\frac{2}{3}}\,P^{\frac{4}{3}}, \tag{4.1}$$

where K consists of well-known constants, T is the common surface temperature, M_p and M_s are the masses of the primary and secondary component, respectively, $q = M_s/M_p$, and P is the orbital period of the system. S represents the total stellar surface area as defined by the Roche geometry, dynamical properties of the binary, and the fill-out factor f by which the stellar surfaces extend beyond the inner critical Roche surface.

Rucinski (1994, 1995, 2000) converted the above equation into the more convenient form

$$M_V^{color} = a_0 + a_1 \log P + a_2\,\mathrm{color}, \tag{4.2}$$

where M_V is the absolute V magnitude, P is the period in days, and the color is reddening-free. For $V-I$ color, this equation is (Rucinski 2000)

$$M_V^{VI} = -4.43 \log P + 3.63\,(V-I)_0 - 0.31. \tag{4.3}$$

The empirically determined standard deviation in this relation is $\sigma \sim 0.29$, corresponding to about 13% in distance. See Rucinski (2000) for a more detailed derivation of the above equation.

4.3.2 Distances to Pulsating Variables

The only two types of pulsating variables we detected in the fields of NGC 3201, M10, and M12 were RR Lyraes (ab type) and an SX Phoenicis (SX Phe) star. GC-member RR Lyraes (c type) are typically located in the HB of a GC (see Figure 1.4) which is saturated in our dataset. The detected RR Lyrae are therefore background

stars. The rapidly pulsating Pop II SX variables or their Pop I counterpart, the δ Scuti stars, are located toward the faint end of the instability strip in the CMD (Rodríguez et al. 2000). If a GC member, the SX Phe variable would thus fall into the blue straggler region of the CMD (see Figure 1.4). All pulsating variables we find in the fields of NGC 3201, M10, & M12 are at around or below the MSTO and are thus not members of the respective GC.

Nemec et al. (1994) give a P-L-[Fe/H] for RR Lyrae (ab type):

$$M_V(\mathrm{RRab}) = 1.08 - 0.52 \log P + 0.32\,[Fe/H]. \tag{4.4}$$

For SX Phe stars, the P-L-[Fe/H] in Nemec et al. (1994) is

$$M_V(\mathrm{SXPhe}) = 0.36 - 2.56 \log P + 0.32\,[Fe/H]. \tag{4.5}$$

We use equations 4.4 and 4.5 in Sections 5.1.5 and 5.2.3 to calculate the distances to the pulsating variables we find and to show that they are not associated with any of the GCs.

4.4 Cluster Membership Determination

A first indication of whether an eclipsing binary star system in the field of a globular cluster is associated with that cluster is, of course, its location with respect to the cluster center (we note that we cannot study the very center of our clusters due to crowding). The tidal radii of NGC 3201, M10, and M12 are 28.45 arcmin, 21.5 arcmin, and 17.6 arcmin, respectively (Harris 1996). Since our LCO field of view subtends 23.5 arcmin on the side (see Table 2.1), all the binary systems we find are well within the tidal radii of the GCs.

A more powerful membership criterion is a binary's location in the CMD. Since binaries are unresolved, they will typically lie above the main sequence by up to 0.75

magnitudes which corresponds to twice the brightness of one of the components. A special case are the blue stragglers. They are typically found in the extension of the main sequence blueward of the MSTO (see Figure 1.4). Hypotheses for formation of these systems include collision of single stars, coalescence of binary stars, or other gravitational interaction between binary systems which would increase their main sequence lifetime by, e.g., mixing "fresh" hydrogen into the partially H-depleted core of the star (Leonard & Linnell 1992; Hut 1993; Livio 1993; Sills & Bailyn 1999; Sills et al. 2000). If a binary star falls elsewhere in the CMD of a GC, it is most likely not a member of the cluster.

The pulsating GC-member variables would be located in the instability strip in the CMD. As mentioned before, these variables, if GC-members, would be saturated in our data. Thus, we are only able to detect background pulsating variables.

The final verdict on cluster membership of any variable in the GC field, however, can only be provided by spectroscopic observations. Typically, the systemic radial velocity of the variable star is compared to the one of the GC and considered a member if they are identical. Associated uncertainties arise from the motion of binary components about their common center of mass. For typical W UMa (0.7 $M_{\odot}$, $P \sim 0.4$ days) binaries, this velocity is on the order of 160 km/s (see equation 5.1). For detached binary systems, it is typically lower ($\sim$ 100 km/s) due to their longer orbital periods.

Spectroscopic observations of binaries in GCs with systemic velocities such as M10 (76 km/s) and M12 (–42 km/s), would need to be timed such that the spectra are taken when the binary components' motions have no radial components (90° phase difference from quadrature). Obviously, this requires precise knowledge of the period and the phase of the binary system under investigation.

NGC 3201, on the other hand, has a much more distinct systemic (retrograde) velocity of approximately 500 km/s (Harris 1996; Côté et al. 1994), so a single spectrum of a binary system with sufficient resolution and signal-to-noise ratio can be used to establish cluster membership for this particular cluster.

CHAPTER V

Results

In this chapter, we describe our results concerning the variables we detect in the GCs NGC 3201, M10, and M12. For NGC 3201, we show the variables' locations in the cluster field and the CMD as well as the phased photometry lightcurves. In addition, we discuss our spectroscopy results for these variables. Based on a comparison between the systemic velocities of the EB systems and that of NGC 3201, we conclude that, of the 14 detected variables, only one of the EBs – a blue straggler with a low variability amplitude – is physically associated with NGC 3201. For M10 and M12, we show, again, the locations of the variable candidates in the cluster fields and CMDs as well as their phased photometry lightcurves. Since we do not have spectroscopy data for these two clusters, we base our estimate of cluster membership of the variables on location in the CMD and the calculation of absolute magnitudes and corresponding distance of W UMa contact EBs. Of the five variables we find in M10 and M12, only one W UMa EB-system is most likely a member of M12, whereas all the other variables are either foreground or background stars.

5.1 NGC 3201

5.1.1 Additional Photometry of NGC 3201

In order to precisely determine the times of quadrature (maximum radial velocity) and accordingly phase our spectroscopic follow-up observations for two of the variable stars we discovered in the NGC 3201 dataset (V11, the Algol, and V12, the detached system; see Section 5.1.2 and Figure 5.6), we performed additional VI 600s photometry observations at the Cerro Tololo Inter-American Observatory (CTIO) 0.9m Telescope during the nights of February 25 – 28, 2001, just prior to our spectroscopy follow-up CTIO 4m run (see Section 5.1.5). The 0.9m telescope setup included a TEK2048 CCD which provided a field-of-view of approximately 13.5 arcmin on the side (Figure 5.2). Initial data processing was done with the IRAF QUADPROC package. For each night, 10 bias frames were combined for the bias subtraction. Flat-field images were produced by combining five twilight flats per filter per night. The fields we observed were centered on the approximate locations of the detached candidate (Field D: $\alpha_{2000} = 10^h17^m25.72^s$ and $\delta_{2000} = -46°20'12.4''$) and the Algol candidate (Field A: $\alpha_{2000} = 10^h18^m32.74^s$ and $\delta_{2000} = -46°30'42.5''$). Field D fell entirely within our original field-of-view which was centered at $\alpha_{2000} = 10^h17^m36.8^s$ and $\delta_{2000} = -46°20'40.0''$, whereas Field A contained stars which we had not observed previously (see Fig. 5.2). We secured 31 I and 27 V observations of Field A as well as 33 I and 35 V observations of Field D.

Field A and Field D provided additional phasing information for the two binaries, enabling us to improve our period estimates for both of these systems. In the case of the detached system (V12), this correction was on the order of five seconds, whereas the previously calculated period for the Algol system (V11) proved to be off by less 0.2 seconds. This illustrates quite well how accurate our period estimates based on

AoV or MSL are.

As mentioned above, Field A contained stars we had not observed in our previous monitoring program, giving us the chance to mine additional data of NGC 3201 for the existence of variable stars. Using the algorithms described in Chapter 2.2 we detected three additional W UMa systems outside our previous field of view (V7-9; see Figures 5.1 and 5.2). We made use of the fact that we had repeated V and I observations of the same system (the Algol star) in both the CTIO and the LCO datasets to photometrically shift the CTIO data to the system of the LCO data. The differential dereddening of the CTIO dataset W UMa variables (V7-9) was performed as described in Chapter III.

5.1.2 Locations of Variable Stars in Field and in CMD of NGC 3201

Table 5.1 gives the basic information about the variable stars we detected in the field of NGC 3201. V_{bright} and I_{bright} are the V and I magnitudes at maximum light, respectively. Figure 5.1 shows the locations of the variable stars in the LCO dataset[1]. Figure 5.2 shows the locations of V11 (the Algol) and the three additional W UMa systems we found in the CTIO photometry data. Finally, Figure 5.3 indicates where the variables fall within the CMD of NGC 3201. The data shown in Figure 5.3 are differentially dereddened to the fiducial region within the cluster. No reddening zero point is applied.

As may be seen in Table 5.1, most of the binary systems (V1-V9) we find in the field of NGC 3201 are of the contact W UMa type. Their periods range from 0.3 to about 1 day. V10 is an RR Lyrae pulsator, located behind the cluster. V11 is a semi-detached binary system, the so-called Algol type EB. V12 is one of the very valuable, rare detached EBs, as may easily be seen from its lightcurve (right hand

[1]We note that we cannot resolve stars in the cluster center due to crowding. In Section 6.2.2 and Fig. 6.1 we show the resulting loss of effective area within the field of more more quantitatively.

Table 5.1. Variable Stars in the Field of NGC 3201

Var. No.	type	RA (2000)	Dec (2000)	period (days)	V_{bright}	I_{bright}
V1	W UMa	10:16:36.92	–46:22:29.3	0.303587(28)	18.054(17)	17.258(20)
V2	W UMa	10:17:07.73	–46:30:18.2	0.345095(42)	18.237(14)	17.319(19)
V3	W UMa	10:17:13.75	–46:27:54.7	0.377114(43)	17.189(21)	16.352(21)
V4	W UMa	10:17:17.18	–46:27:37.5	0.44179(55)*	16.850(17)	15.965(22)
V5	W UMa	10:17:52.93	–46:34:06.7	0.276216(31)	19.847(21)	18.380(32)
V6	W UMa	10:17:59.08	–46:33:25.7	0.37307(39)*	17.270(13)	16.599(19)
V7	W UMa	10:18:56.03	–46:36:10.4	1.0800(90)	18.658(15)	17.064(19)
V8	W UMa	10:18:46.01	–46:30:13.8	0.30642(75)	18.824(14)	17.577(19)
V9	W UMa	10:18:31.97	–46:37:32.9	0.33248(61)	19.609(22)	18.483(27)
V10	RR Lyrae	10:18:03.86	–46:17:48.7	0.592920(53)	17.088(12)	16.446(22)
V11	Algol	10:18:32.74	–46:30:42.5	0.702127(99)	17.728(13)	16.932(19)
V12	Detached	10:17:25.72	–46:20:12.4	2.84810(98)	17.225(14)	16.301(22)
V13	Unclass. 1	10:17:04.83	–46:26:39.7	1.2080(44)*	20.203(35)	18.529(29)
V14	Unclass. 2	10:18:36.28	–46:22:06.2	2.160(13)*	18.915(16)	17.108(21)

Note. —

- Errors in parentheses indicate the uncertainty in last two digits, i.e., $0.303587(28) = 0.303587 \pm 0.000028$ and $2.160(13) = 2.160 \pm 0.013$.
- Photometry errors are the result of adding in quadrature the DoPHOT photometry error for the instrumental magnitude and the rms of the standard star solution.
- The error in the period corresponds to the full width at half maximum (fwhm) of the peak in the AoV power spectrum corresponding to the correct frequency. For the determination of this error, only V data were used, except for the cases of V7, V8 and V13 where we used I data. In some instances, the peak in the power spectrum corresponding to the correct period was assigned essentially the same power as directly neighboring peaks (i.e., it would be hard to pick "by eye" which one is the correct one). In these cases, we estimated the period error to be the distance between the two neighboring peaks (with the peak corresponding to the correct period in the middle). These cases are marked by an asterisk.

panel in Figure 5.6 and the fact that there are periods of constant maximum light in its cycle. This type of binary system is very hard to detect due to its long period (2.8 days) and very low duty cycle (the system only spends 10% of its phase in an eclipse and appears non-variable the rest of the time). Finally, V13 and V14 are thus far unclassified systems. Their lightcurves resemble the W UMa ones, but their periods are very long and their colors are extremely red. Of all the variables listed in Table 5.1 only V6, a BS W UMa binary, is actually associated with NGC 3201 itself as we show in Section 5.1.5.

5.1.3 Phased Photometry Lightcurves of the NGC 3201 Variables

The phased lightcurves for the W UMa systems V1 through V5, detected in the LCO dataset, are presented in the left panel of Figure 5.4. The three additional

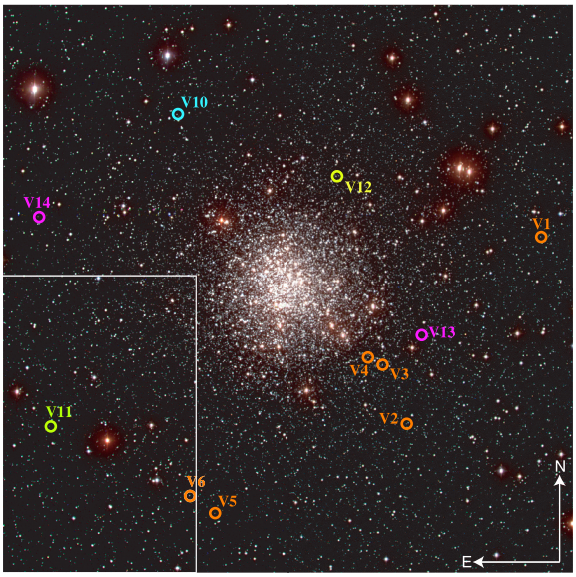

Figure 5.1 The locations of the variable stars in the LCO data. The field-of-view is 23.5 arcmin on the side. North is up and east is to the left. The rectangle toward the bottom left part of the figure represents the the approximate boundaries of the overlap region of this Figure and Figure 5.2, i.e., the north-west part of Figure 5.2. V1–V6 are W UMa binary systems, V7–V9 are located in the field of Figure 5.2, and are also W UMa systems, V10 is an RR Lyrae, V11 an Algol binary, V12 a detached binary system, and V13 & V14 are thus far unclassified variables.

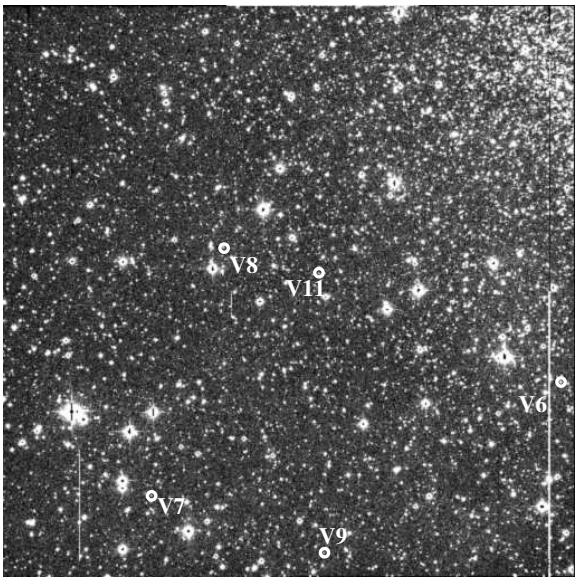

Figure 5.2 The locations of the variables extracted from the CTIO 0.9m data. The field-of-view has the same orientation as the one in Figure 5.1, but is smaller (13.5 arcmin on the side in this figure). V11, toward the center of this image, and V6, toward the right edge of the image, are present in both fields-of-view. V7-9 are located outside (south-east of) the field of Figure 5.1.

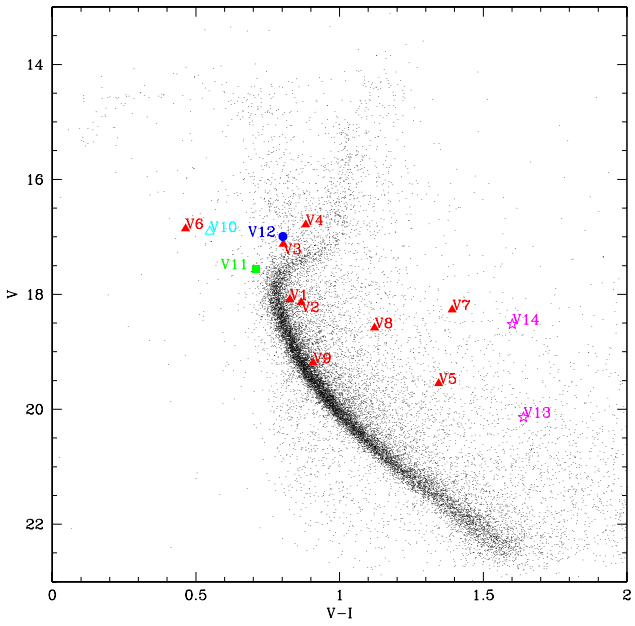

Figure 5.3 The locations of all our variable stars in the field of NGC 3201 in its CMD. The data presented are differentially dereddened to the fiducial region but no reddening zero point is applied. In Section 3.3.2, we calculate the E_{V-I} zero point to be 0.15. The variable stars are plotted at maximum brightness and are also differentially dereddened. Filled triangles represent W UMa types, the open triangle the RR Lyrae, the square the Algol system, the filled circle the detached system, and the open star-shaped symbols the unclassified systems.

W UMa lightcurves, V7 through V9, extracted from the CTIO photometry data (note the difference in sampling due to the lower number of observational epochs for these stars), are in the right panel, along with the lightcurves of V10, the RR Lyrae, and V13 and V14, the two unclassified systems, from the LCO dataset. Figure 5.5 contains the lightcurve of V6, the only member of NGC 3201 among our set of variable stars. V11, the semi-detached Algol system, and V12, the detached binary system, are presented in Figure 5.6. In all of these three Figures, V data are in the bottom panel, I data in the top panel. The error bars represent the photometric errors associated with that particular measurement of the star's magnitude. Since the reddening zero point we calculate for NGC 3201 falls slightly below literature values (see Section 3.3.2), we chose to display the lightcurves in their undereddened form, that is, no reddening correction was applied to the lightcurves. To apply the differential reddening correction for the lightcurve, one needs to simply locate the variable under investigation on the extinction map (Figure 3.3) and read off the differential E_{V-I} from the grid of Fig. 3.4.

All phased data for the photometry lightcurves presented here is available online at `http://adc.gsfc.nasa.gov/adc-cgi/cat.pl?/journal_tables/AJ/123/279/`.

5.1.4 Rucinski Magnitudes for W UMa Variables in NGC 3201

In Section 4.3.1 we describe how to determine distances for the W UMa contact binary systems. Table 5.2 shows the calculated absolute magnitudes and distance moduli for the W UMa binaries in the field of NGC 3201. The distance to NGC 3201 was calculated in BM01 to be 4.5 ± 0.03 kpc; the value found in Harris (1996) is 5.2 kpc. The corresponding true distance moduli are $V_0 - M_V = 13.58$ and 13.26, respectively[2]. We note that the absolute magnitudes and distance moduli

[2]These values represent the apparent distance moduli corrected for extinction.

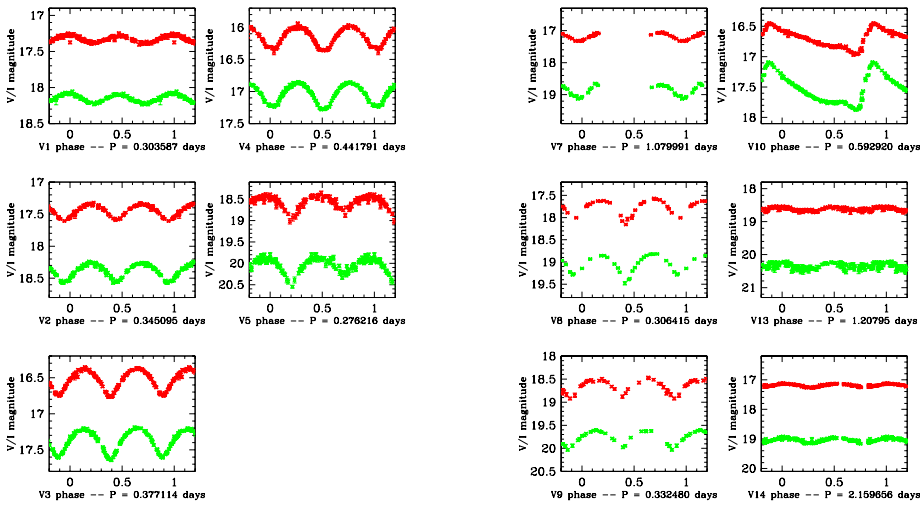

Figure 5.4 The V and I lightcurves of V1 through V9 (all W UMa type binaries), V10, V13, and V14. V7-V9 are the W UMa systems discovered in the CTIO dataset. Note the much sparser sampling of the lightcurves. V10 is the background RR Lyrae star. Finally, V13 and V14 are the two unclassified systems. Their lightcurves look similar to the W UMa types, but their periods are much longer and their colors much redder. In each panel, the I magnitude is plotted above the V magnitude; no extinction correction is applied. None of these variables is associated with NGC 3201 itself.

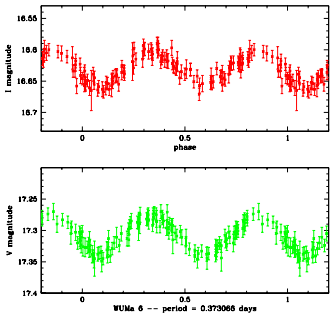

Figure 5.5 The lightcurve of V6, a blue straggler candidate and the only variable star in our sample which is a member of NGC 3201. No extinction correction is applied.

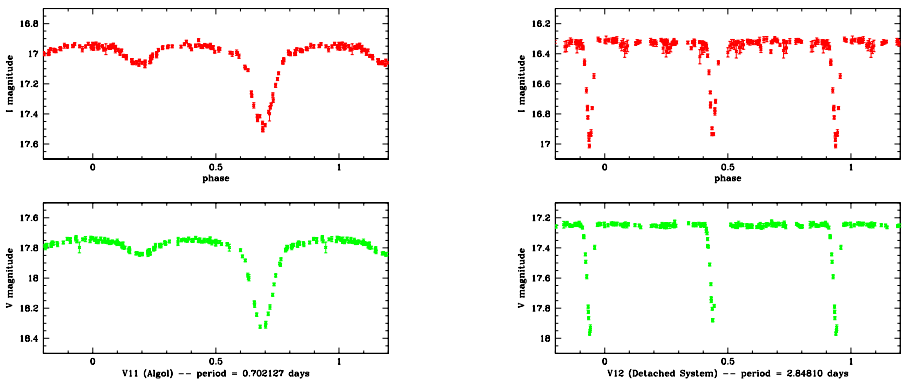

Figure 5.6 The lightcurves of V11, the Algol system, and V12, a detached binary star system. The data for this lightcurve were taken both at LCO and CTIO. No reddening correction is applied to the data. V11 and V12 are not members of the globular cluster.

in Table 5.2 were calculated under the assumption that the W UMa system under investigation is suffering the full extinction between us and the cluster. Since the spectroscopy results indicated that no W UMa system except V6 is associated with NGC 3201 (see following Subsection), and the absolute magnitudes for some of the variables indicate that they are foreground stars (Table 5.2), this assumption might be incorrect in some cases. That is, for some of the non-members, the color might not be the correct, reddening-free value.

The distance modulus of the GC member V6 calculated in Table 5.2 is 13.873, larger than the NGC 3201 distance moduli in both Section 3.3.2 (by $\sim 2\sigma$) and Harris (1996, by $\sim 1\sigma$). One way to "force" V6 to be at the correct distance would be to change the reddening zero point to the cluster and thus change the variable's intrinsic color. Since this correction would force the distance to go down, the reddening zero point obtained this way would decrease to $E_{V-I} \sim 0.02$, significantly below the previously calculated value of 0.15 (Section 3.3.2). At this point, we can therefore not offer any conclusive reason why V6's distance modulus is slightly too high, other than the possibility that this one particular binary would represent an outlier (by

Table 5.2. Rucinski Magnitudes and Distance Moduli for NGC 3201 W UMa-type Binaries

system	period (days)[a]	E_{V-I}[b]	$(V-I)_{0,bright}$[c]	$M_{V(Rucinski)}$	$V_0 - M_V$	distance (kpc)
V1[d]	0.303587(28)	0.131(55)	0.665	4.397	13.405	4.8
V2	0.345095(42)	0.202(34)	0.716	4.336	13.513	5.0
V3	0.377114(43)	0.183(38)	0.654	3.940	12.898	3.8
V4	0.44179(55)	0.183(38)	0.702	3.810	12.689	3.4
V5	0.276216(31)	0.305(65)	1.162	6.383	12.878	3.8
V6	0.37307(39)	0.366(42)	0.305	2.694	13.873	5.9
V7	1.0800(90)	0.352(81)	1.242	4.050	13.932	6.1
V8	0.30642(75)	0.275(61)	0.972	5.494	12.802	3.6
V9	0.33248(61)	0.368(67)	0.758	4.560	14.343	7.4

[a] As in Table 5.1, errors in parentheses indicate the uncertainty in last two digits. The period errors are the same as in Table 5.1.

[b] E_{V-I} contains the reddening zero point, calculated in Section 3.3.2 to be 0.15 mag. As mentioned above, this value assumes that the binary suffers the full extinction along the line of sight to the GC (which is not necessarily correct if the binary is not a cluster member). The errors for E_{V-I} are the random errors in the determination of the *differential reddening*. That is, a possible systematic error in the determination of the reddening zero point (described in Section 3.3.2) is not included in this estimate.

[c] $(V-I)_{0,bright}$ is the dereddened color at maximum light.

[d] V1 is located in a region whose differential reddening along the line of sight is lower than the one of the fiducial region whose overall E_{V-I} is 0.15 mag. Its total E_{V-I} is therefore calculated to be lower than the reddening zero point.

Note. — Rucinski quotes the scatter in his relation (Rucinski 1994, 1995) to be 0.29 mag in the calculation of the absolute V magnitudes (corresponding to an uncertainty of approximately 13% in distance). Since this uncertainty is far larger than the quadratic sum of all our random errors, we refrain from a detailed error analysis for the Rucinski magnitudes and distance moduli.

about 1-2σ) in Rucinski's empirically determined relation.

5.1.5 NGC 3201 Spectroscopy Follow-Up & Cluster Membership of the Variables

Based on the CMD of NGC 3201 (see Figure 5.3), V5, V7, V8, V10, V13 and V14 are not associated with the cluster. Furthermore, based on their distance moduli, the W UMa systems V3, V4, V5, and V8 seem to be foreground stars while V9 seems to be a background star. V1, V2, and V6, however, seem promising cluster member candidates within error estimates, with the only difference being that the reddening calculated for V1 and V2 is significantly lower than the one for V6 (see Table 5.2).

The final verdict on membership, however, can only be provided by spectroscopic observations. NGC 3201 has a distinct systemic velocity of approximately 500 km/s (Harris 1996; Côté et al. 1994), so a single spectrum of a binary system with sufficient resolution and signal-to-noise ratio can be used to establish cluster membership.

During the nights of March 2 – 5, 2001, we performed spectroscopic follow-up

observations of our eclipsing binary star candidates at the CTIO 4m Telescope with Arcon and the RC Spectrograph. Our setup included a 3k x 1k Loral CCD and the KPGLG grating (860 l/mm; 1st order blaze = 11000 Å) in second order. The wavelength coverage extended from 3800 to 5100 Å, with a resolution of about 0.4 Å/pixel. Our observing targets were V1, V2, V3, V4, V6, V11 and V12. V9, a potential cluster member given its location in the CMD, was too faint to observe with our setup at CTIO.

In order to check the cluster membership of V9, we obtained three spectra during the night of March 19, 2001, using the Magellan 1 Telescope with the Boller & Chivens Spectrograph and a setup similar to the one at the CTIO 4m Telescope but with lower resolution (approximately 1.4 Å/pix). Our wavelength coverage extended from 3900 to 5300 Å.

To our great disappointment during the first night of the CTIO spectroscopy run, one spectrum after the next eliminated our candidates from cluster membership consideration. The only system with a systemic velocity equal to that of NGC 3201 is V6, a blue straggler candidate (see Figure 5.3) with a very small amplitude (see Figure 5.5).

Figure 5.7 shows the spectra of the W UMa non-member binaries V1 – V4, and Figure 5.8 shows the spectra of V6, a cluster-member blue straggler W UMa binary, V9, a W UMa binary we observed at Magellan (note the lower resolution), of V11, the Algol binary, and of V12, the detached binary system. The smaller windows in the panels of Figures 5.7 and 5.8 illustrate in more detail the location of the $H\beta$ lines with λ_{rest} of 4861Å. V6 in Figure 5.8 is clearly redshifted, whereas all the other binary systems are not.

Our spectroscopy results are summarized in Table 5.3. The systemic velocities of

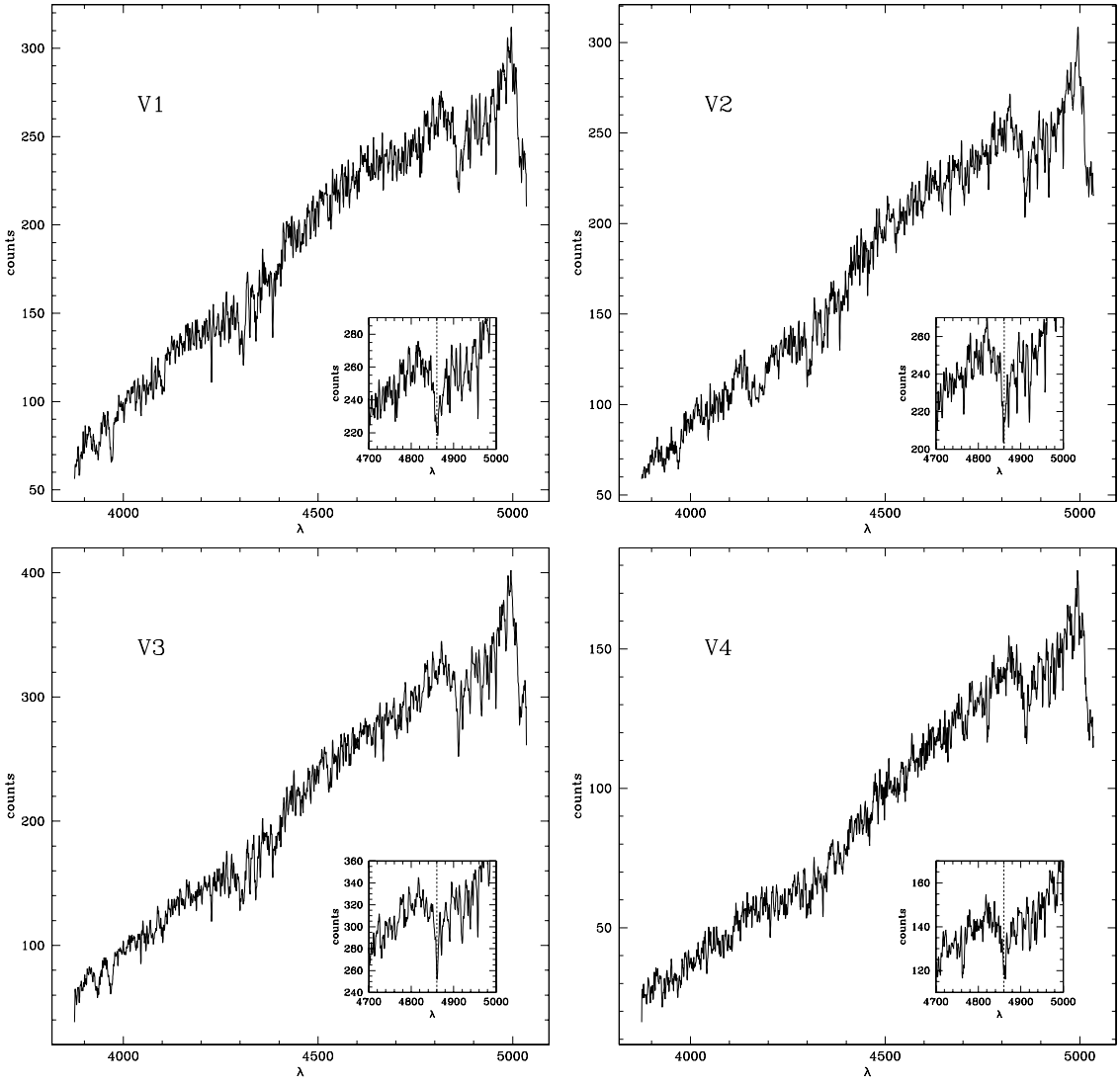

Figure 5.7 This figure shows the non-flux-calibrated spectra of the binaries V1, V2, V3, & V4 (all non-member W UMa systems) in the field of NGC 3201. λ is given in units of Å. The smaller window in each of the four panels shows the location of the $H\beta$ spectral line ($\lambda_{rest} = 4861$Å) in the form of a dashed line. All spectra in this figure were obtained at the CTIO 4m Telescope.

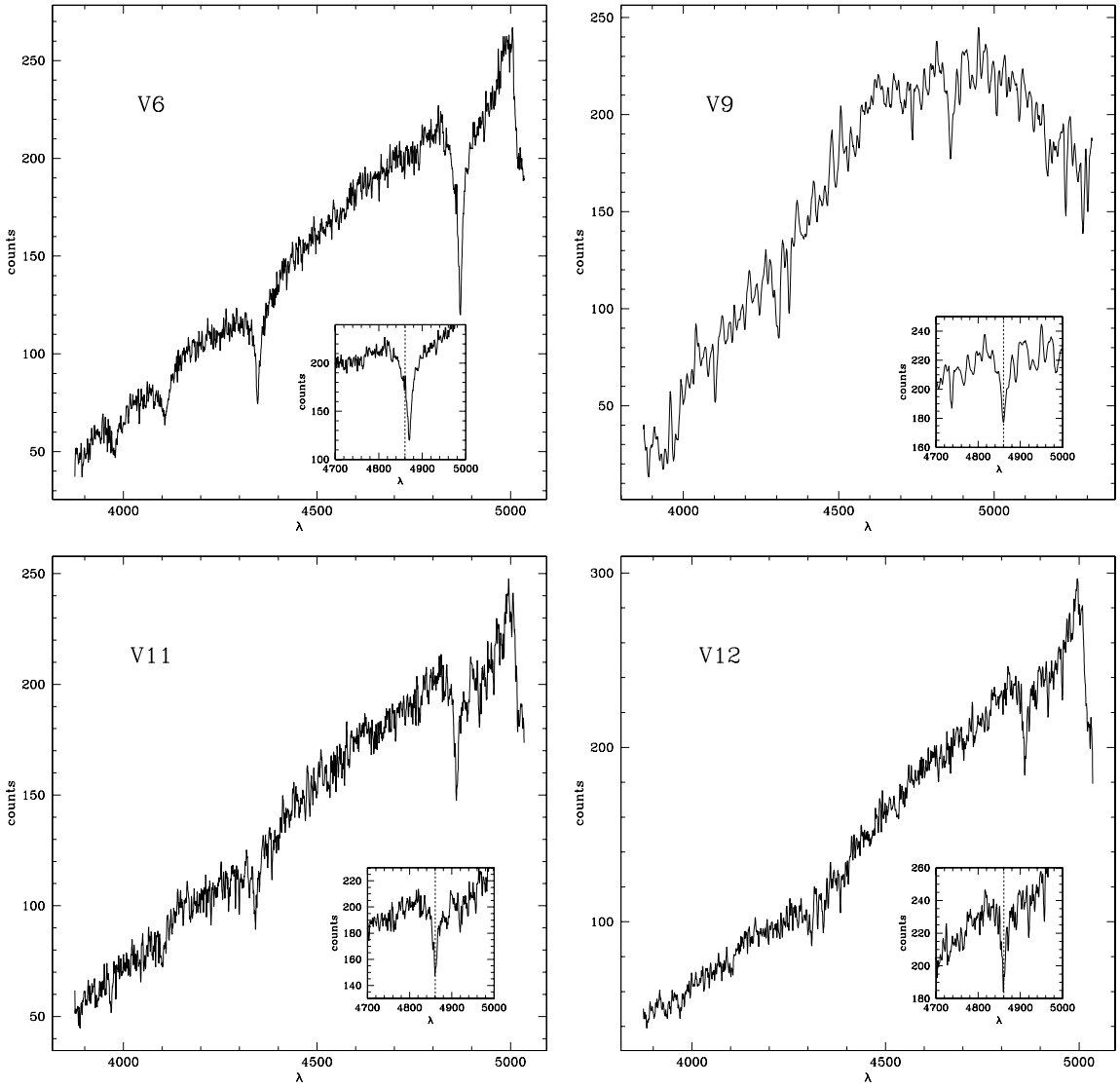

Figure 5.8 This figure shows the non-flux-calibrated spectra of the binaries V6 (GC-member blue straggler W UMa binary), V9 (non-member W UMa binary), V11 (Algol type non-member binary), and V12 (detached non-member binary system) in the field of NGC 3201. λ is given in units of Å. The smaller window in each of the four panels shows the location of the $H\beta$ spectral line (λ_{rest} = 4861Å) in the form of a dashed line. The spectra for V6, V11, & V12 in this figure were obtained at the CTIO 4m Telescope. V9's spectrum was observed at Magellan at lower resolution.

the binaries were determined using the IRAF FXCOR package, using radial velocity standards as templates. We estimate our random error in the velocity determinations of the candidates to be around 20 km/s for the CTIO data (except V6, see below), based on measurements performed on the velocity standards we used. Due to the lower resolution of the spectrum we obtained at Magellan, we estimate V9's velocity uncertainty to be approximately 50 km/s.

We show the radial velocity Fourier cross-correlation profiles (FXCOR output) of the variables (except V6, see below) in Figures 5.9 through 5.15. The top panel in each of these Figures is the continuum-subtracted spectrum of the variable under investigation (wavelength in Å). The bottom two panels represent the shape of the cross-correlation function in different resolutions. The numbers inside the bottom panel are the shift in pixels due to the radial velocity of the variable, the amplitude of the correlation function, the calculated heliocentric velocity and associated rms in km/s, the width of the peak in km/s, and the TonryDavis R value (see Tonry & Davis 1979). Results for the individual binary systems were calculated by using three different radial velocity standards (spectral types G and K) and averaging the values for heliocentric velocity.

The lower-resolution spectrum of V9 shows a double peak in the correlation function which might be due to the two individual binary components. Since we did not know the phase of the system during the observation, it is possible that we caught the system right at quadrature (maximum radial velocity of the two components). In this case, the systemic velocity of the binary system would be around 75 km/s and the velocities of the components about their center of mass around 120 km/s.

The difference in spectral types between V6 and our radial velocity standards (V6's spectral type is much earlier/bluer) made it impossible to determine its velocity

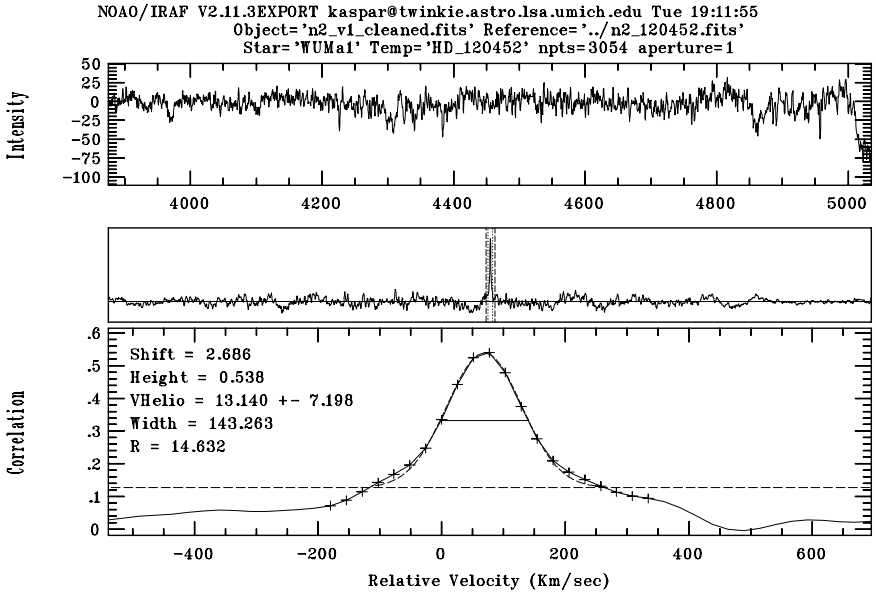

Figure 5.9 Radial Cross Correlation Profile of V1 in NGC 3201. The top panel is the continuum-subtracted spectrum of the variable. The bottom two panels show the radial velocity cross correlation profile.

.

using FXCOR. Instead, we calculated its Doppler velocity from line profile fitting using IRAF's SPLOT package. The error quoted for that star is simply the rms of ~ 10 individual line measurements from different observed spectra of the star.

We further note that for all of our variables, except for our CTIO photometry targets (V7-9 as well as V11 and V12), we do not have phase information obtained more recently than three years prior to the spectroscopy run. The propagation of the period determination error (see Tables 5.1 and 5.2) therefore makes it impossible to constrain the precise phasing of most of our candidates. The uncertainty in the calculation of the systemic velocities of the binary candidates due to the radial motion of the two components is not accounted for in our estimates.[3]

Since NGC 3201's systemic velocity is so high (500 km/s), cluster membership

[3]A binary's period may, of course, also be calculated from the radial velocity curve. Since we were able to eliminate our observing targets (except V6) from cluster membership consideration after obtaining only a few spectra for each system, we refrained from re-observing them and can therefore not determine the phase of the binary at the time of observation.

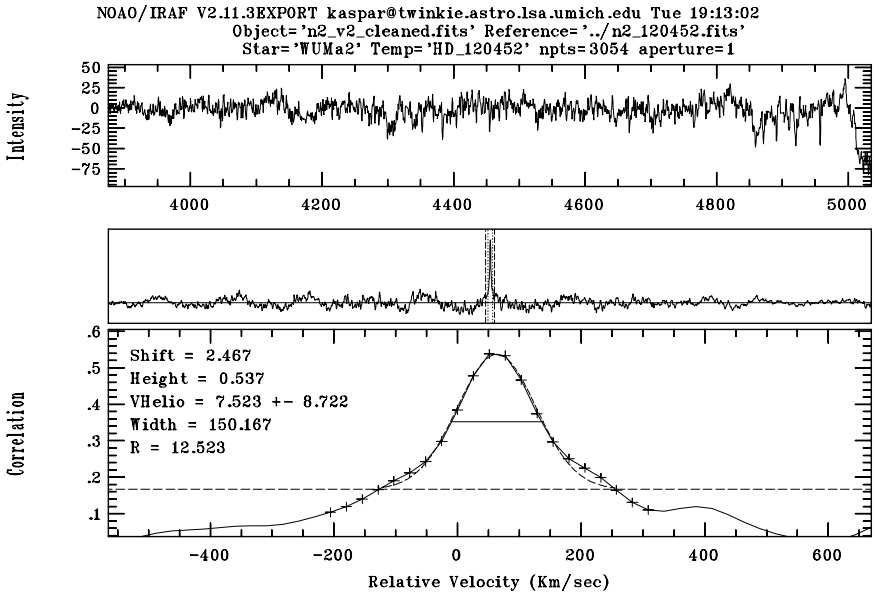

Figure 5.10 Radial Cross Correlation Profile of V2 in NGC 3201. The top panel is the continuum-subtracted spectrum of the variable. The bottom two panels show the radial velocity cross correlation profile.

.

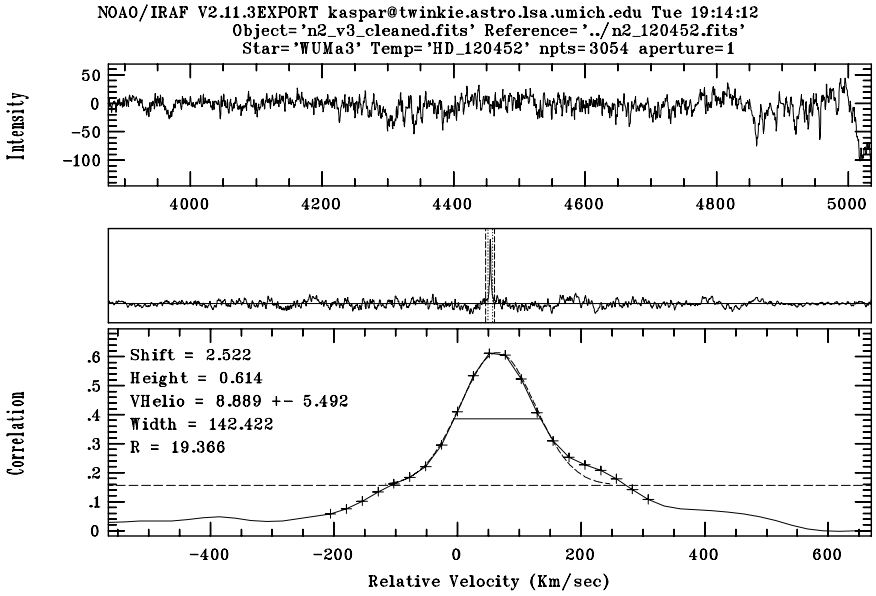

Figure 5.11 Radial Cross Correlation Profile of V3 in NGC 3201. The top panel is the continuum-subtracted spectrum of the variable. The bottom two panels show the radial velocity cross correlation profile.

.

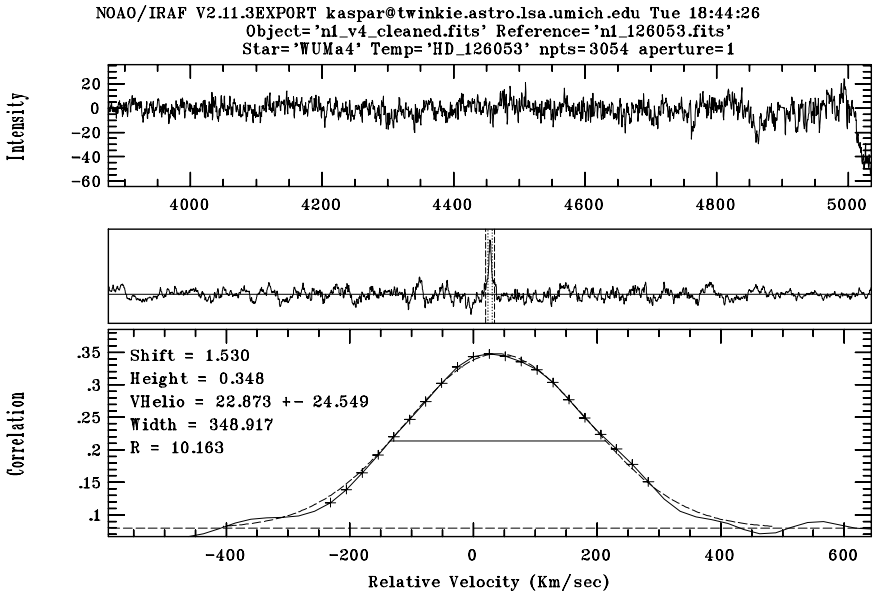

Figure 5.12 Radial Cross Correlation Profile of V4 in NGC 3201. The top panel is the continuum-subtracted spectrum of the variable. The bottom two panels show the radial velocity cross correlation profile.

.

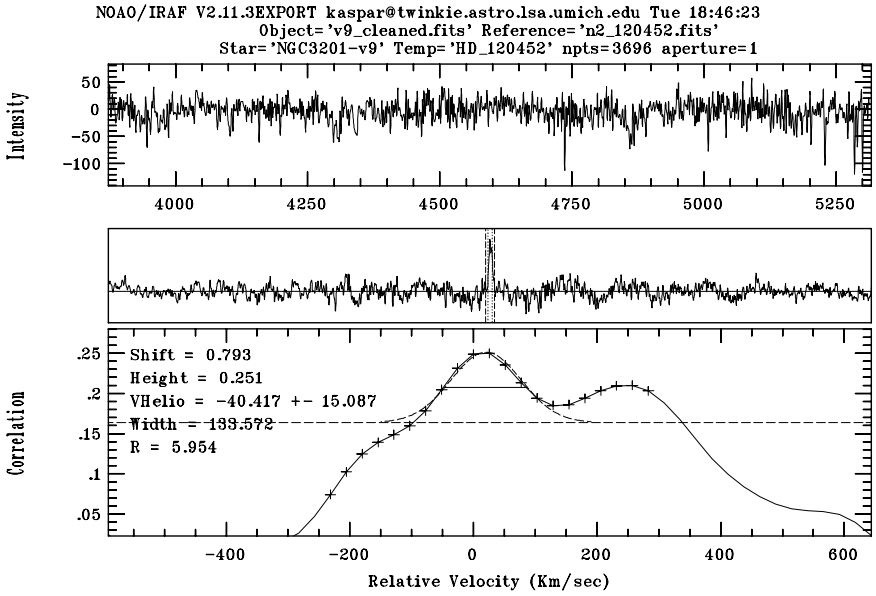

Figure 5.13 Radial Cross Correlation Profile of V9 in NGC 3201. The top panel is the continuum-subtracted spectrum of the variable. The bottom two panels show the radial velocity cross correlation profile. Note the apparent double peak. Data for this plot were taken at Magellan.

.

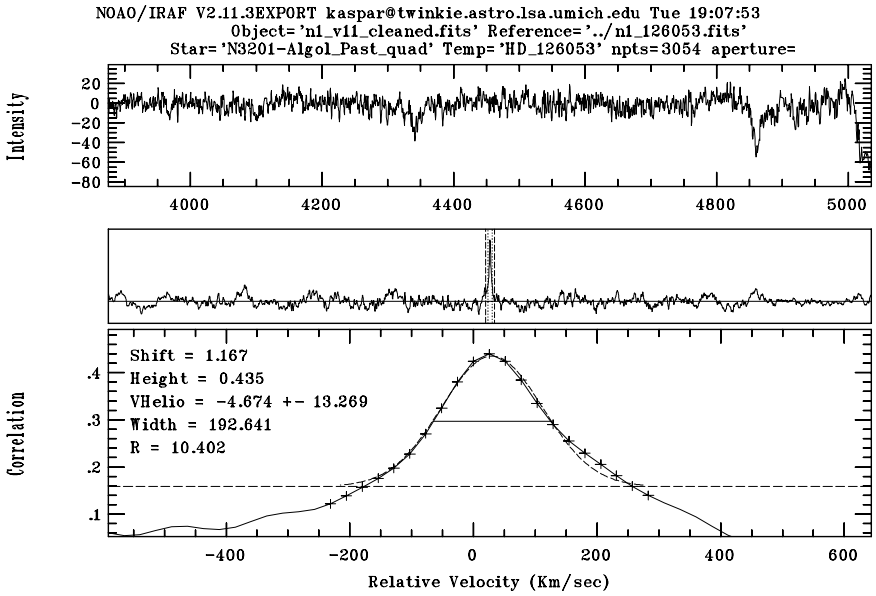

Figure 5.14 Radial Cross Correlation Profile of V11 in NGC 3201. The top panel is the continuum-subtracted spectrum of the variable. The bottom two panels show the radial velocity cross correlation profile.

.

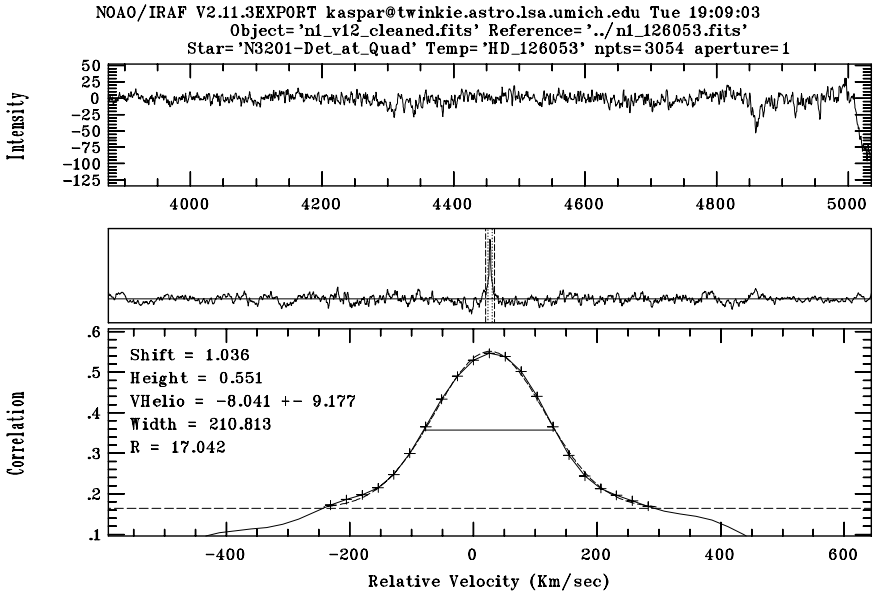

Figure 5.15 Radial Cross Correlation Profile of V12 in NGC 3201. The top panel is the continuum-subtracted spectrum of the variable. The bottom two panels show the radial velocity cross correlation profile.

.

based on the comparison between systemic velocity of the variable and the cluster may be determined without phasing information. The velocity amplitudes of the components of a binary system relate to the masses and the period of the system as follows (Paczyński 1996):

$$\frac{K_1 + K_2}{\sin i} = 386.4\,\mathrm{km/s} \left(\frac{M_1 + M_2}{3M_\odot} \frac{0.5\,\mathrm{days}}{P_{orb}} \right)^{\frac{1}{3}}. \tag{5.1}$$

If one assumes that the orbits of the W UMa systems V1-4 and V9 are circular (which is evidenced by the fact that the minima of the lightcurves are separated by half a period), that $\sin i = 1$ (the system is seen edge-on), and that the masses and thus velocity amplitudes of the two components are equal, one needs only the sum of the masses and the orbital period to get an estimate of the velocity amplitudes. From the VDB isochrones for a cluster age of anywhere inbetween 14 and 18 Gyrs and [Fe/H]=–1.41, one obtains masses for main-sequence stars of $(V - I)_0 \sim 0.7$ of approximately 0.7 $M_\odot$ (for each component). Finally, given the average period of these systems of $\sim$ 0.36 days, we estimate the typical velocity amplitude to be $K_j \sim 165$ km/s. We note, of course, that non-member binaries might have a different metallicity and thus mass for a given color, but since $K \propto M^{1/3}$, this difference would not significantly alter this rough estimate. A deviation from an edge-on configuration would decrease the calculated velocity amplitudes, i.e., the value given above may be regarded as an upper limit.

For V11 and V12, the masses of the individual components are probably slightly larger (bluer $V - I$ color), but the periods are much larger, especially in the case of V12. Retaining the same assumptions as for the W UMa systems, one obtains velocity amplitudes closer to 150 km/s for V11, and 80 km/s for V12.

In order for a binary system to be a member of NGC 3201, its systemic velocity would have to fall within (165 km/s + σ) of 500 km/s (NGC 3201's velocity). As

Table 5.3. Systemic Velocities of NGC 3201 Member Candidates

variable	systemic velocity (km/s)	error (km/s)
V1	12	20
V2	6	20
V3	9	20
V4	20	20
V6	513	44
V9	24[a]	50
V11	1	20
V12	0	20

[a]As can be seen in Figure 5.13, V9's cross- correlation profile has a double peak. We discuss in the text that this could be due to the fact that we are seeing the two individual binary components of the system at quadrature. If this is the case, the systemic velocity of the system would be 75 km/s and the velocity of the motion of the two components around the common center of mass is around 120 km/s.

Note. —

- The variables not listed in this table but listed in Tables 5.1 and 5.2 were considered to be non-members based on their location in the CMD.
- For an explanation on how velocities and errors were determined, see text.
- The systemic velocity of NGC 3201 is $\sim$ 500 km/s (Harris 1996; Côté et al. 1994).

one may easily see in Table 5.3, only V6 survives this criterion.

We obtained approximately 25 spectra of V6 at various phase angles. These results, combined with our photometry data, may be used to calculate the component masses of the binary BS system. The analysis of the radial velocity curve and subsequent calculation of the stellar masses will be addressed in a future publication.

5.1.6 Comment on the Velocities of and Distances to the Binaries in the Field of NGC 3201

The binaries we find in the field of NGC 3201 are located approximately toward the anti-direction of the solar motion through the Galaxy. Upon first inspection, one might therefore expect to see the solar reflex velocity of $\sim$ 220 km/s as the systemic velocities of the binaries.

Assuming the distances in Table 5.2 are correct, then the binaries are located between 500 pc and 1 kpc above the Galactic disk. Using scale heights for the

thin and thick disk of $z_{0,thin} = 325$ pc and $z_{0,thick} = 1.4$ kpc and a stellar density profile of the form $e^{-\frac{z}{z_0}}$ (Carroll & Ostlie 1996), we find that the binaries are very plausibly members of the Galactic disk population. The observed radial velocity of a star located toward the anti-direction of the solar motion, and moving at 220 km/s around the Galactic center, should be

$$v_{observed} = 220\,\mathrm{km/s}\left[1 - \cos\left(\arctan\frac{\mathrm{d}}{8.5\,\mathrm{kpc}}\right)\right]. \tag{5.2}$$

Consequently, a system with d = 4 kpc should have $v_{observed} \sim 20$ km/s, whereas a system with d = 7 kpc should return $v_{observed} \sim 50$ km/s. To first order, the observed velocities (Table 5.3) and calculated distances (Table 5.2) therefore make sense from a Galactic kinematics point of view.

One potential source of error in the determination of the systemic velocity of a binary system is, of course, the motion of the binary components (typically between 100 km/s and 200 km/s for short-period contact systems) which could mimic a different systemic velocity if a system is spectroscopically single-lined at our resolution. Some of the spectra in Figures 5.7 and 5.8 appear to have split lines (see especially the spectra of V1–V4) around $H\beta$. One could therefore argue that the binary's systemic velocity is much higher than the observed velocity since the split is due to the motions of the binary components about their center of mass. In this case, the systemic velocity of the binary would correspond to the wavelength shift of the middle between the split spectral lines. The observed split, however, is on the order of 15 Å, corresponding to velocities of over 450 km/s for each component, which is not possible for these binary systems. Instead, the apparent line split is most likely due to neighboring spectral features.

Table 5.4. Variable Stars in the Fields of M10 & M12

Var. No.	type	RA (2000)	Dec (2000)	period (days)	V_{bright}	I_{bright}
M10-V1	W UMa	16:57:39.15	–4:16:03.9	0.263366(28)	18.890(17)	17.620(19)
M10-V2	RR Lyrae	16:57:41.57	–4:08:24.8	0.61438(23)	18.170(14)	17.650(19)
M10-V3	SX Phe	16:56:48.63	–3:58:35.9	0.0637(41)*	19.538(18)	19.013(33)
M12-V1	W UMa	16:47:22.89	–1:55:35.8	0.243183(15)	18.818(19)	17.949(19)
M12-V2	W UMa	16:47:32.58	–2:03:10.1	0.25212(25)*	18.238(12)	16.750(19)

Note. —

- Errors in parentheses indicate the uncertainty in last two digits.
- Photometry errors are the result of adding in quadrature the DoPHOT photometry error for the instrumental magnitude and the rms of the standard star solution.
- The random error in the period corresponds to the full width at half maximum (fwhm) of the peak in the AoV power spectrum corresponding to the correct frequency. For the determination of this error, only V data were used. For the variables M10-V3 and M12-V2, the peak in the power spectrum corresponding to the correct period was assigned essentially the same power as the directly neighboring peak (i.e., it would be hard to pick "by eye" which one is the correct one). In these instances, we estimated the period rms to be the distance between these two neighboring peaks. The two cases are marked by an asterisk.

5.2 M10 & M12

5.2.1 Locations of Variable Stars in Fields and in CMDs of M10 & M12

Table 5.4 gives the basic information about the variable stars we detected in the fields of M10 and M12. V_{bright} and I_{bright} are the V and I magnitudes at maximum light. Figures 5.16 and 5.17 show the locations of the respective variable stars in the fields of M10 and M12 plus the locations of the fiducial regions used for the calculation of the differential extinction values (see Section 3.1.2). In Section 6.2.2 we discuss the loss of effective field area due to crowding toward the cluster core, see also Fig. 6.1. Figures 5.18 and 5.19 indicate where the variables fall within the CMDs of the two clusters. The data shown in Figures 5.18 and 5.19 are differentially dereddened to the fiducial region within the respective cluster, as described above. No reddening zero point is applied. The variables are plotted at maximum brightness.

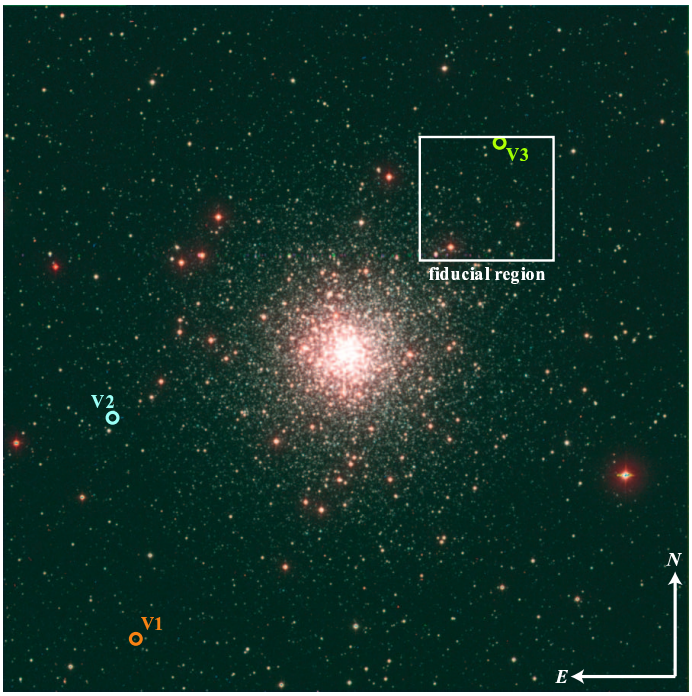

Figure 5.16 CCD Field of view of M10 with the locations of the variables. The fiducial region is shown for reference. The size of the field of view is 81% (23.5 arcmin on the side) of the area shown in Figures 3.9, 3.11, 3.20, and 3.21.

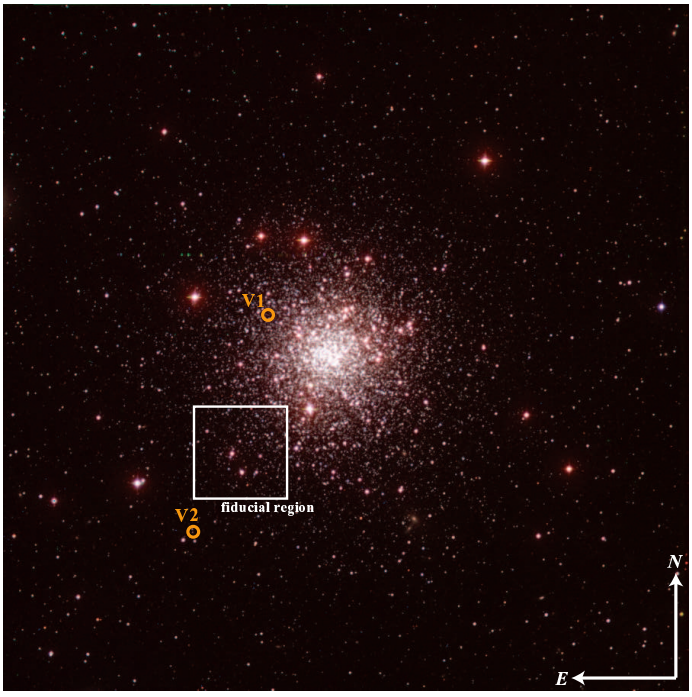

Figure 5.17 CCD Field of view of M12 with the locations of the variables. The fiducial region is shown for reference. The size of the field of view is 81% (23.5 arcmin on the side) of the area shown in Figures 3.10, 3.12, 3.23, and 3.24.

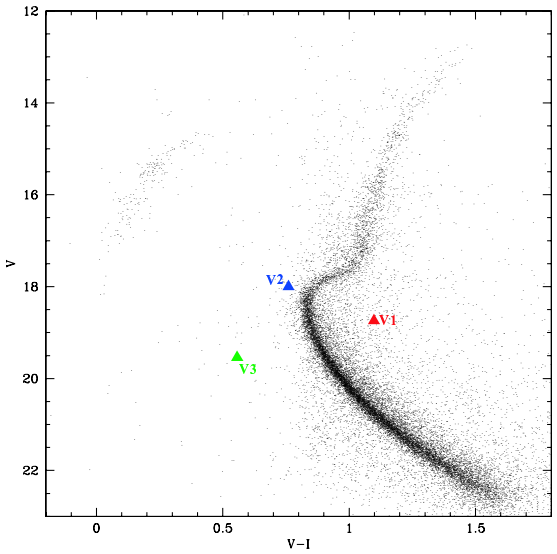

Figure 5.18 The locations of the variable star candidates in the CMD of M10. The data presented, including the variable stars, are dereddened to the M10 fiducial region. No reddening zero point is applied. The variables are plotted at maximum brightness. From this figure alone, it seems that none of the variables we found in the field of M10 are members of the cluster. It should be noted that since we only use our 600s data for binary detection, we are not sensitive to variables brighter than $V \sim 16.5$.

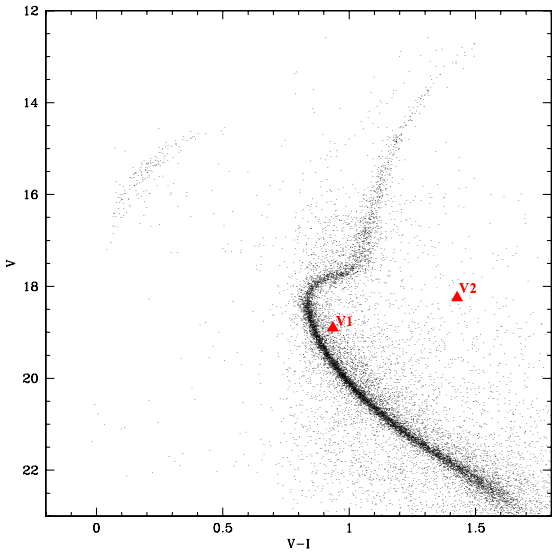

Figure 5.19 The locations of the variable star candidates in the CMD of M12. The data presented, including the variable stars, are dereddened to the M12 fiducial region. No reddening zero point is applied. The variables are plotted at maximum brightness. From this figure alone, it seems that the variable V1 is a cluster member whereas V2 is not. It should be noted that since we only use our 600s data for binary detection, we are not sensitive to variables brighter than $V \sim 16.5$.

5.2.2 Phased Photometry Lightcurves

The phased lightcurves for the variable stars are presented in Figures 5.20 through 5.22. In particular, Figure 5.20 shows the lightcurve of M10-V1 (period = 0.263366 days) which is a W UMa type contact binary system. M10-V2 is a background RR Lyrae (ab type) variable with a period of 0.61438 days; its lightcurve is displayed in the left panel of Figure 5.21. M10-V3 appears to be a field δ Scuti or more likely an SX Phoenicis-type (SX Phe) variable with a period of 0.0637 days. As mentioned Section 4.3.2 these stars are rapidly pulsating Pop I (δ Scuti) or Pop II (SX Phe) stars commonly found toward the faint end of the instability strip in the CMD (Rodríguez et al. 2000)) in the BS region. M10-V3's lightcurve is shown in the right panel of Figure 5.21. M12-V1, another W UMa binary, seems to be the only variable in our data set which is physically associated with its respective parent GC. Its period is 0.243183 days, and its lightcurve is displayed in the left panel of Figure 5.22. M12-V2, another W UMa binary, but not associated with M12, has a period of 0.25212 days; its lightcurve is in the right panel of Figure 5.22. In all of these Figures, V data are in the bottom panel, I data in the top panel. The error bars represent the DoPHOT photometric errors associated with that particular measurement of the star's magnitude.

As for NGC 3201 we did not apply any reddening correction to the lightcurves (see Section 5.1.3). In order to apply any reddening correction to a lightcurve, one needs to "select" and apply a reddening zero point (we discuss the calculation of this zero point in Sections 3.3.3 and 3.3.4), and correct for differential extinction by locating the variable under investigation on the extinction map (Figure 3.9 for M10 and Figure 3.10 for M12) and read off the differential E_{V-I} from the grids of Figs. 3.11 (M10) and 3.12 (M12).

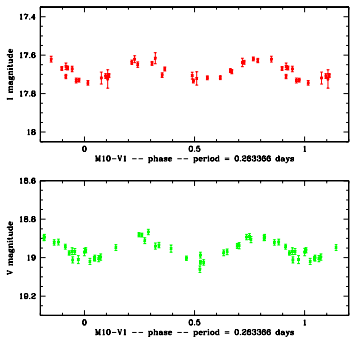

Figure 5.20 The binary star V1 in the field of M10, a W UMa system with a period of 0.263366 days. I data are in the top panel, V data in the bottom panel. No reddening correction is applied to the lightcurve data. M10-V1 is not a member of M10.

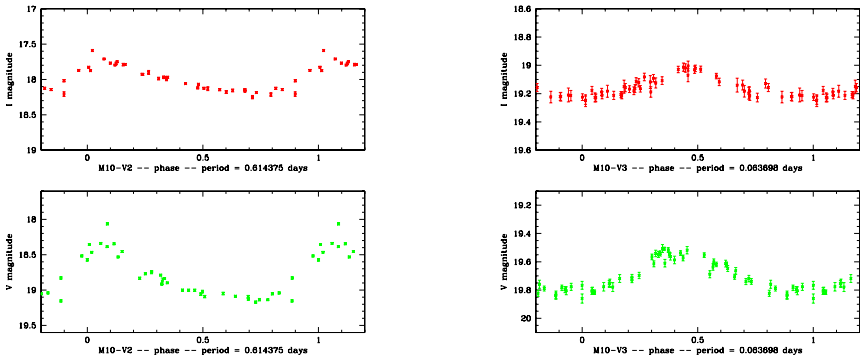

Figure 5.21 The pulsating variables V2 (left) and V3 (right) in the field of M10. V2 is a background RR Lyrae system (distance 40 kpc) with a period of 0.61438 days. V3 is a background SX Phe pulsating variable (distance 16 kpc) with a period of 0.0637 days. I data are in the top panel, V data in the bottom panel. No reddening correction is applied to the lightcurve data.

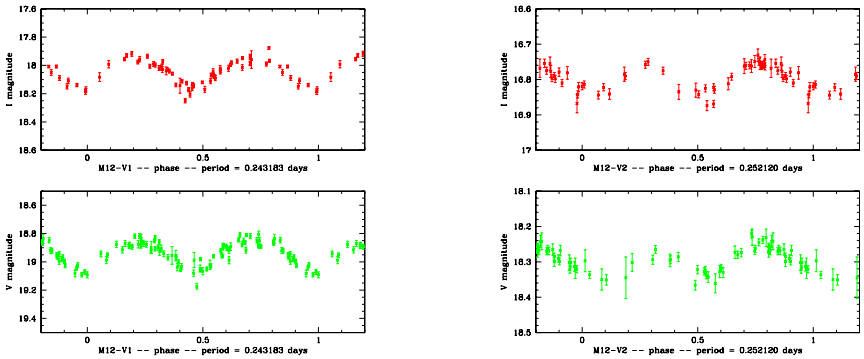

Figure 5.22 The binaries V1 (left) and V2 (right) in the field of M12. V1 is a W UMa system with a period of 0.243183 days and the only variable which is most likely physically associated with a GC. V2 is a W UMa binary system with a period of 0.25212 days, not a member of M12. I data are in the top panel, V data in the bottom panel. No reddening correction is applied to the lightcurve data.

5.2.3 Cluster Membership of the Variables in M10 & M12

Binaries (in M10 and M12)

All the binary systems we detect in the fields of M10 and M12 are of the W Ursa Majoris type. As explained in Section 4.3.1 W UMa binaries are systems in which the two components are in physical contact with each other. Their absolute magnitude can be calculated with equation 4.3 in Section 4.3.1.

Table 5.5 shows the absolute magnitudes and distance moduli for the W UMa binaries in the fields of M10 and M12 based on equation 4.3. The distances to the clusters were calculated in Sections 3.3.3 and 3.3.4 to be 5.1 kpc (M10) and 4.9 kpc (M12). The corresponding true distance moduli (apparent distance moduli corrected for extinction) are $V_0 - M_V = 13.55$ and 13.46, respectively. As for NGC 3201, we note that the absolute magnitudes and distance moduli in Table 5.5 were calculated under the assumption that the W UMa system under investigation is suffering the full extinction between us and the cluster. Since the absolute magnitudes for some of the variables indicate that they are foreground stars, this assumption might be incorrect in some cases.

The tidal radii of M10 and M12 are 21.48 and 17.6 arcmin, respectively (Harris 1996). Thus, all the binary systems we find are well within the tidal radii. Based on the CMDs of M10 and M12 (see Figures 5.18 & 5.19), M10-V1 and M12-V2 are not associated with their respective parent cluster. M12-V1, however, appears to be a cluster member from its location in M12's CMD. The estimates of distance moduli to the various W UMa binaries in Table 5.5 confirm what the GC-CMDs suggest: M10-V1 and M12-V2 are foreground stars, but M12-V1 is most likely a member of M12 (it falls well within one $\sigma_{Rucinski}$ of the calculated distance to the GC).

Table 5.5. Rucinski Magnitudes and Distance Moduli for W UMa-type Binaries in the Fields of M10 & M12

system	period (days)[a]	E_{V-I}[b]	$(V-I)_{0,bright}$[c]	$M_{V(Rucinski)}$[d]	$V_0 - M_V$[e]	distance (kpc)
M10-V1	0.263366(28)	0.323(07)	0.947	5.695	12.576	3.3
M12-V1	0.243183(15)	0.249(04)	0.620	4.661	13.679	5.4
M12-V2	0.25212(25)	0.259(03)	1.229	6.802	10.939	1.5

[a] As in Table 5.4, errors in parentheses indicate the uncertainty in last two digits. The period errors are the same as in Table 5.4.

[b] E_{V-I} contains the reddening zero points for the two clusters, calculated in Section 3.2.1. As mentioned above, this value assumes that the binary suffers the full extinction along the line of sight to the GC (which is not necessarily correct if the binary is not a cluster member). The errors for E_{V-I} are the random errors in the determination of the *differential reddening*. That is, any possible systematic error in the determination of the reddening zero point is not included in this estimate.

[c] $(V-I)_{0,bright}$ is the dereddened color at maximum light.

[d] $M_V = -4.43 \log P + 3.63\,(V-I)_0 - 0.31$ (see Section 4.3.3)

[e] The true distance modulus to M10 is $V_0 - M_V = 13.55$ and the one to M12 is 13.46. These values represent the apparent distance moduli corrected for extinction.

Note. — Rucinski quotes the scatter in his relation (Rucinski 1994, 1995) to be 0.29 mag in the calculation of the absolute V magnitudes (corresponding to an uncertainty of approximately 13% in distance). Since this uncertainty is far larger than the quadratic sum of all our random errors, we refrain from a detailed error analysis for the Rucinski magnitudes and distance moduli.

Pulsating Variables (in M10)

The two pulsating variable stars we detected in M10 are M10-V2, an ab-type RR Lyrae star, and M10-V3, either a δ Scuti or an SX Phe star. From their locations in M10's CMD, it is apparent that neither of them is associated with the cluster.

Since GC-members RR Lyraes are typically found on the horizontal branch, M10-V2 is clearly a background star. Application of the P-L-[Fe/H] relation (equation 4.4) from Section 4.3.2 (Nemec et al. 1994) and assuming that [Fe/H] ~ -1.5, M10-V2's distance is around 40 kpc, putting it into the Milky Way halo beyond the bulge.

As mentioned above, GC-member SX Phe stars are frequently found in the blue straggler region of the CMD. Since M10-V3 is not inside this region, we conclude that it is not a member of the GC. Instead, the photometry results for M10-V3 ($\Delta V \sim 0.32$, P ~ 0.064 days, $(V-I)_0 \sim 0.29$[4]) quite exactly correspond to the modes in the distributions of the catalog of field δ Scuti and SX Phe stars of Rodríguez et al.

[4] From comparison with the CMD of M10 by Hurley et al. (1989), this approximately corresponds to $(B-V)_0 \sim 0.3$, i.e., a spectral type of about F0.

(2000); see their figures 1, 3, & 4. Since the number of known field SX Phe stars is very low (Rodríguez et al. 2000; Rodríguez & López-González 2000; Jeon et al. 2001) we cannot say for sure whether M10-V3 is a field δ Scuti or SX Phe variable (see for example figure 5 in Jeon et al. 2001). Since M10-V3 is a background variable, however, and thus located in the halo, we will assume that it is an SX Phe variable. Using the appropriate P-L-[Fe/H] relations (equation 4.5) in Section 4.3.2 (Nemec et al. 1994, 1995) with an assumed [Fe/H] $\sim$ –1.5, we obtain a distance to M10-V3 of approximately 16 kpc.

CHAPTER VI

Conclusion

6.1 Brief Summary of Results

6.1.1 NGC 3201

In the process of finding eclipsing binary stars in the low-latitude GC NGC 3201, we noticed the existence of variable reddening of up to 0.2 mag in E_{V-I} on a scale of arcminutes. Using our internal dereddening method outlined in Section 3.1.1, we created an extinction map which is shown in Figures 3.3 and 3.4. Applying the map to our raw data significantly improved the appearance of the CMD (Fig. 3.8). Comparison between our extinction map and the SFD map of the same region (Fig. 3.6) showed that the same larger-scale features exist in both maps. Our map displays some additional, smaller-scale features which are absent in the SFD maps (see Fig. 3.7).

The E_{V-I} zero point which needs to be added to the numbers in Fig. 3.4 in order to get absolute E_{V-I} values was determined by isochrone fitting to the differentially dereddened data. Its value is 0.15 mag, giving an average $E_{V-I} \sim 0.24$. This estimate is below literature results (Cacciari 1984; Harris 1996) by approximately 1σ, but produces by far the best VDB isochrone fit to the data (Figure 3.15). The zero point determined with the SFD maps gives $E_{V-I} \sim 0.34$ as the average value across NGC 3201 which is higher than literature values, supporting the statement

by Arce & Goodman (1999) that the SFD maps tend to overestimate the reddening in regions of high extinction.

Our search for photometrically variable stars in the magnitude range of approximately $16.5 < V < 20$ and for periods between roughly 0.1 and 5 days in NGC 3201 resulted in 14 variable star candidates in the field of which nine are eclipsing binaries of the W UMa type, one is an Algol-type EB, and another one is a detached binary system. Spectroscopic follow-up observations revealed that only one of the variables, a blue straggler W UMa EB, is associated with the cluster itself, despite the promising locations of a number of binaries within the CMD of NGC 3201 (Fig. 5.3). Due to the low-latitude location of the GC, the high contamination of Galactic disk stars in the field of NGC 3201 seems to have manifest itself 13 times in our analysis.

6.1.2 M10 & M12

The GCs M10 and M12 were monitored for the existence of photometrically variable EBs in the magnitude range of approximately $16.5 < V < 20$ and for periods between roughly 0.1 and 5 days. Observations were conducted over a span of about four years with only relatively few epochs per observing run due to the equatorial locations of the clusters.

During the search for variables, we noticed strong differential reddening effects across the field of M10 (Figure 2.2) and a similar, but weaker signature across M12 (Figure 2.3). We correct for this differential reddening by creating the extinction maps shown in Figures 3.9 (M10) and 3.10 (M12). The features visible in these maps are very well spatially correlated with the ones detected by SFD in their dust emissivity maps of the same regions – see Figures 3.20 (M10) and 3.23 (M12). Applications of our differential extinction maps to our data significantly improves the

appearance of the GC CMDs (Figures 3.13 and 3.14), especially in the case of M10.

The E_{V-I} zero points for M10 and M12, which need to be added to the differential E_{V-I} values in the grids of Figures 3.11 and 3.12, are 0.23 mag and 0.24 mag, respectively, determined by fitting VDB isochrones to the differentially dereddened data. The resulting estimates for the average E_{V-I} values are 0.28 mag for M10, and 0.25 mag for M12. Since previous reddening estimates for these two GCs vary, especially for M10, our results agree with some literature values but not with others. Specifically, our reddening estimate for M12 agrees well with the SFD maps, whereas our value for M10 falls below the one quoted in SFD ($E_{V-I} \sim 0.389$), but produces by far the best VDB isochrone fit.

Our search for variable stars in M10 and M12 produced five candidates: a W UMa binary, an RR Lyrae, and an SX Phe field variable for M10. None of these three systems appears to be physically associated with M10, given their locations in the CMD (Figure 5.18) and their estimated distances (Table 5.5 and Section 5.2.3). In M12, we detected two W UMa binary systems, one of which (M12-V1) is most likely a cluster member. Again, we base this estimate on CMD location (Figure 5.19) and calculated distance moduli (Table 5.5).

6.2 Implications

6.2.1 Differential Extinction Maps

The unique nature of GCs enabled us to create maps which show the distribution and amount of dust located along the lines of sight to the clusters studied in this work. Such reddening studies may be useful in determining properties of the interstellar medium such as a dependence of R_V and temperature upon position in the field of view. In addition, they may give insight into the properties and the distribution of the dust along the line of sight. Furthermore, reddening maps such as the ones

presented here can give a sense of how small a scale differential extinction in general may vary on, and by how much, perhaps as a function of position in the sky or Galactic latitude.

Obviously, a first use of our extinction maps is a means of direct comparison with the SFD maps of the same regions. Since the SFD maps are based on dust IR emissivity, the two sets of maps provide entirely independent results. Since the difference maps for all three studied GCs spatially agree very well (see Chapter III and specifically Figures 3.7, 3.21, and 3.24), both sets of reddening maps (SFD and ours) independently confirm each other's results on a larger scale. The smaller-scale structure we detected in the field of NGC 3201, but which did not show up in the SFD maps, is an example of how the two sets of maps may complement each other. Most likely, the temperature of these dust features, located at $(x, y) = (9.5, 9.5)$ and $(x, y) = (17, 16)$ in Figures 3.3 and 3.4, was below the sensitivity of the SFD $COBE/DIRBE$ instruments (as evidenced by the clumpy, "cold" structure of the features, see Figure 3.7).

Estimating the angular diameter of both these clouds to be about 5 arcminutes and a height above the Galactic plane of $z \sim 100$ pc gives a distance to the features of 700 pc and a diameter of 1 pc. The average differential E_{V-I} across the features is around 0.15 mag, which, combined with the reddening zero point calculated in Section 3.3.2 of 0.15 mag, yields a total $E_{V-I} \sim 0.3$. Using table 6 in SFD produces the relation

$$A_V = 2.463\, E_{V-I}, \tag{6.1}$$

resulting in $A_V \sim 0.75$ mag due to the dust along the line of sight to the clouds. The

relation between extinction and the column density of dust causing the extinction is

$$m_\lambda - m_{\lambda,0} = 1.086\, N_d\, \sigma_\lambda, \tag{6.2}$$

where m_λ is the observed apparent magnitude in a given filter, $m_{\lambda,0}$ the same apparent magnitude, corrected for extinction, N_d the dust column density, and σ_λ the wavelength-dependent cross section of the dust grains (Carroll & Ostlie 1996). Assuming that $\sigma_\lambda \sim 2 \times 10^{-9}\mathrm{cm}^2$ ($r_{dustgrain} \sim 0.25\,\mu m$) gives a column density of $N_d \sim 3.4 \times 10^8 \mathrm{cm}^{-2}$. Multiplying N_d by $\pi \times (0.5\mathrm{pc})^2$ returns a total of $\sim 2.5 \times 10^{45}$ dust particles. If the average weight per dust particle is around 10^{-11} g (Spitzer 1978), the mass of the total dust in the cloud is around 2.5×10^{34} g. Under the assumption that dust makes up roughly 1% in weight of the gas in the cloud, one obtains a total mass of the cloud of around 1000 $M_\odot$, theoretically enough to collapse into a Bok globule (Kane et al. 1994; Carroll & Ostlie 1996; Moreira et al. 1999) or even form a number of low-mass field protostars if the star formation efficiency is on the order of a few percent (Shu et al. 1987; Vazquez-Semadeni et al. 2002).

In order to get an idea about the star-forming prospects of these clouds, one may alternatively apply the virial theorem to obtain the equation

$$\frac{GM^2}{5R} = NkT, \tag{6.3}$$

where G is the gravitational constant, M is the total mass of the cloud, R is its radius, k the Boltzmann constant, and T the temperature of the cloud. N, the total number of particles, is

$$N = \frac{M}{\mu\, m_H}, \tag{6.4}$$

where m_H is the mass of a Hydrogen atom and μ is the mean molecular weight of a particle in the cloud, assumed to be roughly 2. For $T \sim 10$K, the resulting

cloud mass is around 50 $M_{\odot}$, an order of magnitude below (within the errors due to uncertainties in the assumptions) to the results of the calculation above, indicating that the cloud is virialized, and, indeed, should collapse under its own weight. The existence of the cloud, however, indicates that an additional mechanism is supporting it against collapse. This mechanism is most likely a magnetic field (Shu et al. 1987). Equating the terms for hydrostatic and magnetic pressure gives

$$G \frac{3\,M^2}{4\,\pi\,R^4} = \frac{B^2}{8\,\pi}. \tag{6.5}$$

If we assume that the mass not supported by the kinetic motions of the particles is 950 $M_{\odot}$, that the density in the cloud is uniform, and that $R = 0.5$ pc, then the magnetic field strength in the cloud is on the order of $B \sim 10^{-4}$ gauss.

Clouds with properties as discussed here are practically not detectable in the visual and infrared bands due to their small sizes and low densities and temperatures, except by the extinction they cause. Studies like our dereddening work in the GC fields therefore provide a unique opportunity to probe the interstellar medium, though only in very small regions, for the existence of small, virialized clouds such as the ones described above.

Furthermore, in the case of the dust features along the line of sight to M10 and M12, one may argue that, since the GCs are so close to each other in the sky, they may lie behind a common, larger scale layer of dust which accounts for the practically identical reddening zero points. M10 then seems to fall behind an additional dust ridge (suggested by, e.g., Kennedy et al. 1996) causing the strong differential reddening which varies on arcmin (or smaller) scales by up to tenths of magnitudes across its field. The combination of two separate components of interstellar dust would thus be responsible for the extinction along the line of sight to M10. Two other neighboring clusters in our sample (M53 and NGC 5053; see Table 1.1) will give us

another opportunity of probing for a similar effect, although these two clusters suffer much less extinction than M10 and M12 (Table 1.1 and Harris 1996).

Finally, our extinction estimates are lower than the SFD values by around 0.1 mag for NGC 3201 and M10, both of which showed signs of strong differential reddening across their fields. The two E_{V-I} estimates for M12, on the other hand, which does not show much differential reddening, agree to ~ 1 mmag. Though any extrapolation of these results is based on three clusters only, one may argue that a change in R_V as a function of position on the sky could be reason for this discrepancy (D. Finkbeiner, private communication 2002). However, our results tend to fall *below* the SFD values, yet we are more likely to pick up components missed by the SFD method (see above). In order to "force" our values and SFD values to agree one could vary the conversion factor between E_{B-V} and E_{V-I}. For a standard reddening law,

$$E_{B-V} = 0.7273 \times E_{V-I} \tag{6.6}$$

for an I filter with $\lambda_{central} \sim 8100$Å (Schlegel et al. 1998). To make the SFD E_{V-I} estimates for M10 and NGC 3201 agree with the ones calculated in Chapter III, this factor would have to be increased to approximately 1.0 (i.e., $E_{B-V} = E_{V-I}$, which would consequently make the two estimates for M12 disagree). Alternatively, it may be true that for whatever reason, the SFD maps tend to overestimate reddening in regions of strong differential reddening. We may be able to shed more light on this question with the analysis of the remainder of our cluster sample.

6.2.2 Variable Stars

As in the case of NGC 3201, we detect a number of foreground and background variables in M10 and M12 but only one (likely) GC member binary. Both M10 and M12 are at higher Galactic latitude ($\sim 25°$) than NGC 3201 ($\sim 8.5°$), so the

disk contamination is not as significant. The number of total stars which were monitored was only slightly different (27000 for NGC 3201 and 34000 for M10 and M12 combined, see Table 4.1)[1], but in the case of NGC 3201, we found 14 variables (11 binaries, one member), whereas for M10 and M12 combined we find five variables (three binaries, one probable member). In all three fields, cluster-member stars outnumber non-member stars, as may easily be seen in the CMDs of the clusters and as we show below. Yet the number of non-member binaries we find is much higher than the number of member binaries[2].

According to Tables 5.2 and 5.5, all 10 non-member EBs for which we determined distances have heights above the Galactic plane between 500 pc and 1300 pc. V11 and V12 in NGC 3201 have zero systemic velocities, indicating that they are most likely nearby systems[3]. As neither of the three GCs is located toward the Galactic bulge, the 12 non-GC-member EBs are therefore very plausibly members of the Galactic thin or thick disk.

Estimates for the ratio of observable main-sequence, short-period ($P \leq$ 1–2 days) eclipsing binaries in the disk to disk main-sequence (MS) stars vary in the literature. Mateo (1996) quotes one observable EB per 500 MS stars in the solar neighborhood. Binney & Merrifield (1998) give an estimate of one EB with $P \leq 1$ day for every 1000 observed MS stars in the disk. Rucinski (2001) quotes OGLE results of one EB per 130 FGK dwarfs (uncorrected for inclination effects).

The equivalent EB frequency for GCs, i.e., the number of observed short-period,

[1]These are all stars below the saturation limit of approximately $V \sim 16 - 16.5$ in the 600s exposures. Since the noise in the photometry data makes it difficult to detect and classify variables fainter than $V \sim 20$, the number of stars from which we draw our sample of binaries is actually below the numbers quoted above, as we describe below in this Section.

[2]It should be noted that we are not sensitive to cluster-member pulsating variables since almost all of them are saturated in the data we analyze for the existence of binaries. A comparison between GC member and non-member pulsating variables is therefore not meaningful.

[3]It is possible, though unlikely, that they could be halo-members whose systemic velocities happen to be zero, or that the motions of the individual components disguise a non-zero systemic radial velocity.

MS, GC-member EBs per observed MS, GC-member star, is even more uncertain due to the lack of spectroscopically confirmed GC-member EBs (Rucinski 2000; Clement et al. 2001). As we showed in this work (see Section 5.1.5), the determination of GC membership based on CMD location and/or Rucinski distances alone does not necessarily reflect the results derived from spectroscopic follow-up work which is not available for a large fraction of the known EBs in GCs (Rucinski 2000; Clement et al. 2001). Mateo (1996) quotes one observed GC-member EB per 1300 monitored MS stars in GCs. Binney & Merrifield (1998) quote a ratio of 1/1000 for the same number, very close to Mateo (1996). Alternatively, one could attempt to estimate this frequency from the catalog of Clement et al. (2001). In this catalog, approximately 100 short-period EBs are found in a total of 102 GCs. The majority of these EB systems are of the W UMa type, and most of them are found in ω Cen, 47 Tuc, M4 and M71. However, since a large fraction of these GCs were monitored for pulsating member variables, and since it is not certain what fraction of the detected EBs in GCs are actually member stars, we cannot use the information in Clement et al. (2001) to provide an alternative estimate of the ratio of observed short-period, GC-member EBs to observed GC stars.

In order to estimate the number of non-member stars in our fields for NGC 3201, M10, and M12, we used software written by John Bahcall, available at `http://www.sns.ias.edu/~jnb/Html/galaxy.html` which is based on the Bahcall-Soneira Galaxy model (described in Bahcall 1986) and calculates the expected number of stars within a user-defined magnitude interval per square degree. To obtain a value for the GC-members stars which we used to mine for the existence of EBs, we simply counted the stars within the range $16.5 < V < 20$ in our cluster fields. Although these cluster fields are 23.5 arcmin on the side, their effective area is smaller due

to the effect of obliteration regions which DoPHOT places around saturated stars, CCD defects, and crowding towards the GC core. In Figure 6.1 we show the radial distribution of stars in our GC fields, along with core and half-mass radii of the clusters. We estimate that we lose about 20% of the field of view, mostly due to crowding, and apply this correction when we calculate the number of non-member stars in the fields (i.e., we reduce the number of stars returned by the Bahcall-Soneira model by 20%).

For a range of $16.5 < V < 20$, we find around 3000 Galactic foreground or background stars for the field of NGC 3201, according to the Bahcall-Soneira model. The total number of stars in our database in that magnitude range which we used for the detection of binary systems is around 10000, i.e., the number of GC-member stars used for binary detection is around 7000.[4]

For M10, the Bahcall-Soneira model predicts 1700 non-member stars. We find a total of 8000 stars in the field. Thus, the number of GC-members we mined for EBs is approximately 6300. For M12, there are 1300 non-members and a total of 6500 stars in the field, i.e., 5200 GC-members were monitored for the existence of EBs.

For all three clusters, we thus obtain a frequency of observed EBs with the properties described above of 1/9000 for GC-members and 1/500 for Galactic disk stars. The calculated field frequency is consistent with literature estimates, whereas the frequency for GCs is an order of magnitude below previously quoted values. It will be interesting to see whether this trend continues in the rest of the GCs in our sample which will be analyzed using the same methods as outlined in this work, or whether NGC 3201, M10, and M12 are merely "special cases". If one assumes that the true frequency of observed EBs in GCs is around one EB per 1000 monitored stars and

[4]It should be noted that the Bahcall-Soneira model is not as accurate for low Galactic latitudes ($< 20°$) as it is for high latitudes due to the patchy obscuration by low-latitude dust along the line of sight (Bahcall 1986).

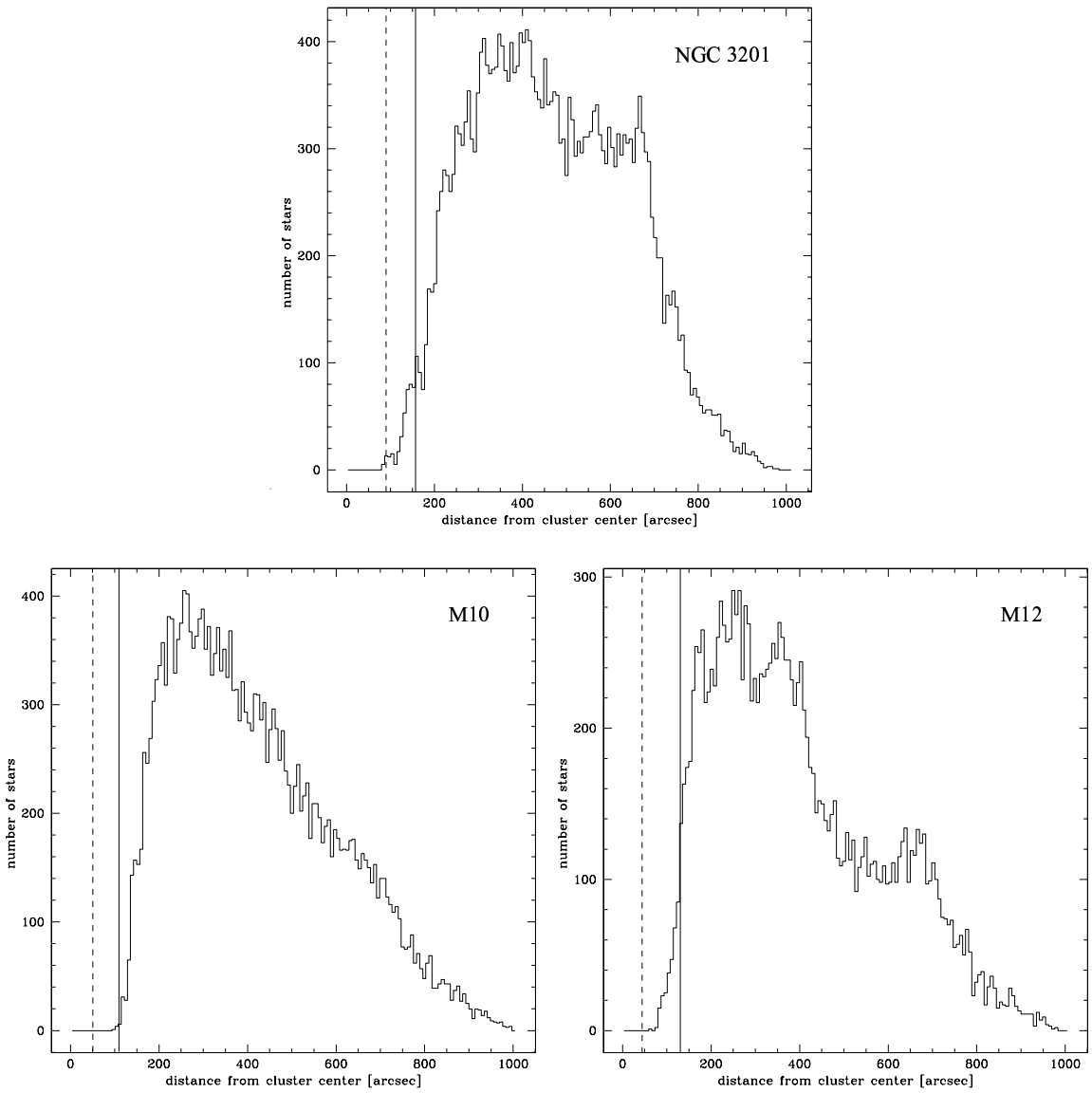

Figure 6.1 This figure shows how the number of stars we find in the GCs changes with radial distance from the respective cluster center and demonstrates how close to the core we can obtain stellar magnitudes with out current data and data reduction pipeline. We estimate that we lose approximately 20% of the CCD area to crowding, and, to a minor extent, saturated stars and CCD defects. The dashed lines indicate the locations of the GC core radii, and the solid ones the half-mass radii (Harris 1996). All the stellar magnitudes we measure and all the binaries we find are well outside the core radii of the GCs. The stars in the three panels have magnitudes of $16 < V < 23$, i.e., they represent the non-saturated stars in the 600s exposures.

that the numbers follow a Poisson distribution of the form

$$p(x;\lambda) = \frac{e^{-\lambda}\,\lambda^{x}}{x!} \tag{6.7}$$

where p represents the probability that a value x is observed when the expectation value is λ, then the probability of our detecting 2 GC-member EBs among 18000 monitored stars, when we *should have found* 18, is

$$p(x \leq 2;18) = \sum_{x=0}^{2} \frac{e^{-18}\,18^{x}}{x!} \approx 3 \times 10^{-6}, \tag{6.8}$$

i.e., 0.0003%. If, however, this true frequency of observable EBs is more on the order of one EB per 1500 monitored MS stars (a value consistent with literature estimates), then the probability of our detecting only two systems increases to around 0.05%.

This discrepancy between our results and previous studies may, in part, be due to an overestimate of the EB frequency in the literature as a result of only assuming, but not spectroscopically confirming, the GC-membership of detected EBs. If we had based our estimate of the EB frequency on only CMD locations of the EBs in our sample, especially for NGC 3201, our results would be much closer to literature values.

A more significant effect, however, results from our inability to probe the GC centers for binaries due to crowding effects. Binary stars will tend to be more frequent toward the cluster centers, as we describe below. The literature studies used to obtain the EB frequency estimate were able to resolve binary systems within the center of the clusters and will therefore calculate a higher value for the binary frequency than our work will permit.

In general, binaries may form primordially (out of a protostellar cloud with excess angular momentum), through three-body encounters, and as a result of inelastic collisions between individual stars (Binney & Tremaine 1987). Since the stellar density

in a GC increases rapidly toward the center, the probability of binary formation through three-body encounters and inelastic collisions, and consequently the binary fraction, will be higher closer to the GC center. In a GC with a collapsing core, the fraction of tidally captured binaries may be as high as 10% (Binney & Tremaine 1987). One may argue, of course, that the probability for the disruption of binary systems should equally increase with higher stellar density. As shown in Binney & Tremaine (1987), however, binaries whose components are sufficiently close are very stable with respect to stellar encounters. Indeed, they actually tend to "harden" as a result of such encounters and become even more stable by converting part of the kinetic energy of the incoming star into additional binding energy of the binary system.

Furthermore, any close binary system will, as a result of its higher mass, gradually "sink" toward the bottom of the potential well, i.e., toward the center of the GC. To estimate whether this mass segregation constitutes an additional effect accounting for the discrepancy between our estimate for the EB fraction among MS stars and the corresponding literature values, we need to examine whether the GCs in our sample have had enough time for the heavier binaries to drift towards the cluster core (which will happen over the course of a few cluster relaxation times). In Binney & Tremaine (1987), a generic formula to calculate the relaxation time of a GC is given as

$$t_{relax} = t_{cross} \frac{0.1\,N}{\ln N}, \tag{6.9}$$

where T_{cross} is the cluster crossing time, and N is the number of stars in the cluster. We estimate t_{cross} be on the order of 10^5 years and assume that we detect approximately half of the stars in the GCs. Consequently, our GCs contain between 30000 and 50000 stars (see Table 4.1). For 30000 stars, t_{relax} is around $3{\times}10^7$ years,

whereas for 50000 stars, it is approximately 5×10^7 years. The GCs in our sample are therefore well relaxed[5], and mass segregation has had ample time to occur, causing an increase in EB frequency toward the cluster center which we are not able to resolve in our data.

Finally, our confirmation of V6 in NGC 3201 as a member increases the number of known binary blue stragglers in GCs. Mateo et al. (1990) predicted that 3%-15% of all BSs in GCs should be photometrically observable binaries. Rucinski (2000) estimates this number to be 2–3%. In the case of NGC 3201 there are nine total BSs (Sarajedini 1993). Our detection of one BS member binary is therefore consistent with these predictions. Thus, the membership of V6 supports the basic Mateo et al. (1990) model that BSs evolve from primordial or, at least, long-lived binaries which coalesce after a lifetime of slow angular momentum loss.

6.3 Future Work

6.3.1 Remainder of GC Sample

Table 1.1 shows all the GCs of our survey for which we have more than 100 epochs taken between June 1994 and May 1999 (evenly divided between V and I, exposure time 600s). Most of the data were taken at the MDM 1.3m telescope and the LCO 1m telescope, with some M15 and M53 data obtained at the Palomar 60 inch telescope. Observers include Kaspar von Braun, Mario Mateo, Kristin Chiboucas, Alex Athey, Denise Hurley-Keller, Ian Thompson, and Lin Yan. The GCs in our survey were chosen mainly based on proximity and low central concentration in order to maximize the number of monitored GC-member stars. Other considerations included a) how much the clusters had already been studied for binaries, and b) the location of the

[5]It should be noted that the relaxation time of a GC depends on stellar density and thus radial distance from the cluster center. It will be higher in the GC halo and shorter toward the core. Our calculated values are rough estimates for the cluster as a whole.

clusters (to optimize our observing, we required multiple GCs which were observable throughout the course of one night). In the near future, we will apply the methods and techniques outlined in this work to perform a similar analysis to the rest of the GCs as we did for NGC 3201, M10, & M12. Preliminary photometric results already exist for M15 and NGC 6752 (von Braun et al. 1996). In both clusters we found promising variable star candidates. In addition, we obtained spectra of the some of the candidates in NGC 6752 using the CTIO 4m Telescope with the Argus Fiber Spectrograph, though that observing run suffered from bad weather and bad seeing.

Despite the fact that we did not identify a large number of member binaries in NGC 3201, M10, & M12, we have nevertheless shown the potential to do just that for the other globular clusters in our survey by detecting and classifying the variables in the GC fields. We successfully identified a BS EB with an V amplitude of around 0.07 mag (see Figure 5.5) and a detached system with duty cycle of around 0.1 (see Figure 5.6). We determined periods to a precision of seconds or better (see Section 5.1.3) and detected systems and of short (0.064 days) and long periods (2.85 days), even when using very different observing techniques for the individual GCs. Using our existing 1m-class telescope photometry data set of the rest of the GCs in our sample, we should be able to identify binaries and other variables in these clusters (provided they exist) and determine their periods. With the spectroscopic capabilities of modern 8m-class telescopes for follow-up observations, we will determine cluster membership for these variables in the near future, and do the necessary follow-up to create radial velocity curves for distance and mass calculations.

Finally, we plan to examine the core regions of all 10 of our GCs using the increasingly popular image subtraction method (described in Alard & Lupton 1998; Alard 1999, 2000). As we show in Figure 6.1, crowding represents a serious obstacle

for our current data reduction pipeline out to 3–5 arcmin from the cluster center. By using the image subtraction method on our existing photometry data, however, we should be able to identify EBs closer to the core (if they exist).

6.3.2 Other Applications of Methods and Techniques

Differential Extinction Correction

Currently, age estimates are available only for part of the Milky Way GCs (Sarajedini et al. 1997). Differentially dereddened GC CMDs allow much better the use of empirical age-dating techniques which rely on CMD features. In addition to the standard isochrone fitting, two popular age-dating methods are the "vertical" and "horizontal" method. The vertical method measures the average magnitude offset between the MSTO and the HB branch, whereas the horizontal method uses the color-distance between the MSTO and the base of the RGB (Sarajedini et al. 1997). Since

$$\frac{\delta age}{age} \sim \delta M_V, \tag{6.10}$$

a 0.1 mag error in the determination of the location of any CMD feature due to differential extinction would correspond to a 10% error in age determination based on methods such as the horizontal and vertical method.

For age estimates based on standard isochrone fitting, the biggest uncertainty in the age calculation is, as mentioned above, the determination of the distance to the GC based on L_{MSTO} (Krauss 2000) since for a given observed flux:

$$\frac{\delta age}{age} \sim 2\frac{\delta d}{d}, \tag{6.11}$$

corresponding to a 10% error in age for a 5% distance uncertainty (VDB isochrones and Paczyński 1996).

Using our differential dereddening technique could therefore be used to reduce measurement uncertainties of features in the GC CMDs and obtain more reliable empirical values for cluster age and distance, especially in Milky Way GCs with very high absolute and differential extinction.

It is straightforward to modify our existing observing strategy, aimed at detecting variable stars in GCs, such that its primary target is the study of differential extinction across the fields of a number of GCs, some of which might suffer very high extinction ($E_{V-I} > 1$). The only observational requirement is deep ($V > 21$), high-quality VI photometry. Only a few epochs per cluster would suffice to use the methods outlined in Chapter III in order to correct for differential extinction across the cluster field and subsequently perform isochrone fitting to obtain estimates for age, distance, and reddening zero point of the cluster under investigation. The detection of small dust clouds, as discussed in Section 6.2.1, may be an additional side product of a program like this. The Mosaic CCD Cameras at both the CTIO and Kitt Peak National Observatory 4m Telescopes feature large fields of view (36 arcmin on the side) and a relatively small pixel scale (0.27 arcsec/pixel). They thus provide an ideal setup for this kind of project.

The dereddening technique outlined in Chapter III relies on and makes use of the fact that GCs are a single-age population in which all stars are located at the same distance, which makes them a unique tool for doing a reddening analysis. These two assumptions (same age, same distance) are true for Galactic GCs in general (with the exception of a few clusters which seem to exhibit different-age populations such as ω Cen, see Hughes & Wallerstein 2000). An additional assumption we made for our method of correcting for differential extinction is a uniform value of the metallicity for the GC. As shown by, e.g., Brown & Wallerstein (1992) and Anthony-Twarog

et al. (1995), however, this assumption may not be quite as reliable for all Milky Way GCs.

In order to simultaneously account for both differential reddening effects and metallicity gradients within the field of view of a GC (such as M22, a member of our sample, see Anthony-Twarog et al. 1995; Peat et al. 2000), one would have to fit for additional parameters in the process and assume at least some aspects of stellar models which relate metallicity to intrinsic color, thereby requiring a fairly substantial revision of the technique as it exists now and was described above. As a first step, one could make use of the fact that, at fainter magnitudes, the reddening vector is nearly parallel to the main sequence. The slope of a VDB isochrone at $V > 21$, however, changes towards higher values (steeper slope) for lower metallicity. This region would therefore lend itself to determining metallicity effects without having to account for the the influence of differential extinction.

Variability Detection Methods

Our observing and data reduction methods of detecting variables and determining their periods are applicable in a variety of fields in astronomy which involve the detection and classification of periodic signals. One such area which is becoming very popular is the detection of extrasolar planet transits. Extrasolar planets may be discovered in a number of different ways, such as radial or proper motion (wobbling) of the parent star, direct photometric detection of reflected light off the planet's surface, or the transit method, based on a photometric detection of a minuscule dimming of the star as a result of the planet's passing in front of the stellar disk. The latter of these methods works best for the comparatively small terrestrial planets (Perryman 2000) and is based on very similar techniques as we use to detect EBs in GCs (described in Chapter IV).

Compared to binary eclipses, however, detecting planetary transits is a formidable task. Whereas amplitudes of binary eclipses are on the order of 0.05 to 0.5 mag, a dimming of a sun-like star due to a planetary occultation would be more on the order of 0.01 mag for Jupiter-sized planets down to 10^{-4} mag for terrestrial ones. Furthermore, the duty cycle of a detached EB system might be on the order of 0.1, while for planetary transits this number shrinks to around 0.05 for "hot Jupiters" (Brown et al. 2001), defined as gas giants with P_{orb} <5 days (Gilliland et al. 2000), and even as low as 1.5×10^{-3} for the earth-sun system seen edge-on. Finally, effects such as star spots might mimic the signal expected from of transiting planets. It is therefore clear that in order to have a chance of finding planets around other stars, one needs to simultaneously monitor a large number of main sequence stars[6] at a high signal-to-noise-ration (SNR) for extended periods of time.

If one assumes the use of a 2m telescope for the monitoring studies and an average $V \sim 14$, obtaining 10^6 electrons per stellar image will take a few minutes. In theory, a 3σ detection per image will then be on the order of 3 mmag, a precision which has been achieved in the past (Howell et al. 2000; Charbonneau et al. 2000). Since a transit will last on the order of hours, multiple measurements of a transit detection could be combined to increase the SNR so that a relative photometric precision of better than 10^{-3} is feasible, allowing detection of even Earth-sized planets around late-type (K, M) main-sequence stars (Howell et al. 2000). The number of stars actually harboring planets is very uncertain at this point, but has been estimated in the percent level (Gilliland et al. 2000). The number of stars (with planets) with inclination angles such that a transit can be detected is dependent on the semi-major axis of the planet's orbit and the size of the star. For hot Jupiters it falls into the 10%

[6]Since the detection probability of transiting planets is proportional to $(\frac{R_{planet}}{R_{star}})^2$, giant stars, though bright, are less desirable observing targets.

range (Gilliland et al. 2000). Effects such as star spots or flares could be eliminated from consideration due to their non-repetitiveness.

Finally, detected systems are ideal spectroscopic follow-up targets for large ground-based telescopes or HST. By summing over a range of wavelengths, spectroscopic data provide very high-precision photometry (better than 10^{-4} in Brown et al. 2001) of bright stars which permits the calculation of orbital periods to a precision of seconds and even a check for the existence of planetary rings or satellites and perhaps elements in the planet's atmosphere (Charbonneau et al. 2002). The spectroscopic information derived from measurements during ingress and egress of the planet can be used to calculate limb-darkening coefficients and thus increase the precision in the determination of the ratio of planetary to stellar radius.

Bibliography

Alard, C. 1999, A&A, 343, 10

—. 2000, A&AS, 144, 363

Alard, C. & Lupton, R. H. 1998, ApJ, 503, 325+

Andersen, J. 1991, A&A Rev., 3, 91

Anthony-Twarog, B. J., Twarog, B. A., & Craig, J. 1995, PASP, 107, 32

Arce, H. . G. & Goodman, A. A. 1999, ApJ, 512, L135

Arribas, S., Martinez Roger, C., Paez, E., & Caputo, F. 1990, Ap&SS, 169, 45

Bahcall, J. N. 1986, ARA&A, 24, 577

Beers, T. C., Flynn, K., & Gebhardt, K. 1990, AJ, 100, 32

Bertelli, G., Bressan, A., Chiosi, C., Fagotto, F., & Nasi, E. 1994, A&AS, 106, 275

Binney, J. & Merrifield, M. 1998, Galactic astronomy (Galactic astronomy / James Binney and Michael Merrifield. Princeton, NJ : Princeton University Press, 1998. (Princeton series in astrophysics) QB857 .B522 1998 ($35.00))

Binney, J. & Tremaine, S. 1987, Galactic dynamics (Princeton, NJ, Princeton University Press, 1987, 747 p.)

Brewer, J. P., Fahlman, G. G., Richer, H. B., Searle, L., & Thompson, I. 1993, AJ, 105, 2158

Brown, J. A. & Wallerstein, G. 1992, AJ, 104, 1818

Brown, T. M., Charbonneau, D., Gilliland, R. L., Noyes, R. W., & Burrows, A. 2001, ApJ, 552, 699

Burstein, D. & Heiles, C. 1982, AJ, 87, 1165

Cacciari, C. 1984, AJ, 89, 231

Cardelli, J. A., Clayton, G. C., & Mathis, J. S. 1989, ApJ, 345, 245

Carroll, B. W. & Ostlie, D. A. 1996, An introduction to modern astrophysics (Reading, MA: Addison-Wesley, —c1996)

Chaboyer, B. 1999, in ASSL Vol. 237: Post-Hipparcos cosmic candles, 111+

Charbonneau, D., Brown, T. M., Latham, D. W., & Mayor, M. 2000, ApJ, 529, L45

Charbonneau, D., Brown, T. M., Noyes, R. W., & Gilliland, R. L. 2002, ApJ, 568, 377

Clement, C. M., Muzzin, A., Dufton, Q., Ponnampalam, T., Wang, J., Burford, J., Richardson, A., Rosebery, T., Rowe, J., & Hogg, H. S. 2001, AJ, 122, 2587

Côté, P., Welch, D. L., Fischer, P., Da Costa, G. S., Tamblyn, P., Seitzer, P., & Irwin, M. J. 1994, ApJS, 90, 83

Covino, S. & Ortolani, S. 1997, A&A, 318, 40

Forte, J. C., Cellone, S. A., Mendez, M., & Vega, E. I. 1992, ApJ, 388, 383

Freedman, W. L. 2000, Phys. Rep., 333, 13

Fukugita, M. 2000, preprint (astro-ph/0005069)

Gallart, C., Freedman, W. L., Mateo, M., Chiosi, C., Thompson, I. B., Aparicio, A., Bertelli, G., Hodge, P. W., Lee, M. G., Olszewski, E. W., Saha, A., Stetson, P. B., & Suntzeff, N. B. 1999, ApJ, 514, 665

Gilliland, R. L., Brown, T. M., Guhathakurta, P., Sarajedini, A., Milone, E. F., Albrow, M. D., Baliber, N. R., Bruntt, H., Burrows, A., Charbonneau, D., Choi, P., Cochran, W. D., Edmonds, P. D., Frandsen, S., Howell, J. H., Lin, D. N. C., Marcy, G. W., Mayor, M., Naef, D., Sigurdsson, S., Stagg, C. R., Vandenberg, D. A., Vogt, S. S., & Williams, M. D. 2000, ApJ, 545, L47

Gnedin, O. Y., Lahav, O., & Rees, M. J. 2001, preprint (astro-ph/0108034)

Gonzalez, G. & Wallerstein, G. 1998, AJ, 116, 765

Harris, W. E. 1996, AJ, 112, 1487+

Hogg, H. S. 1973, Publications of the David Dunlap Observatory, 3, 1

Houdashelt, M. L., Bell, R. A., & Sweigart, A. V. 2000, AJ, 119, 1448

Howell, S. B., Everett, M., Davis, D. R., Weidenschilling, S. J., McGruder, C. H., & Gelderman, R. 2000, AAS/Division for Planetary Sciences Meeting, 32, 0+

Hughes, J. & Wallerstein, G. 2000, AJ, 119, 1225

Hurley, D. J. C., Richer, H. B., & Fahlman, G. G. 1989, AJ, 98, 2124

Hut, P. 1993, in ASP Conf. Ser. 53: Blue Stragglers, 44+

Hut, P., McMillan, S., Goodman, J., Mateo, M., Phinney, E. S., Pryor, C., Richer, H. B., Verbunt, F., & Weinberg, M. 1992, PASP, 104, 981

Jeon, Y., Kim, S., Lee, H., & Lee, M. G. 2001, AJ, 121, 2769

Jimenez, R. 1999, in Dark matter in Astrophysics and Particle Physics, 170+

Kallrath, J. & Milone, E. F., eds. 1999, Eclipsing binary stars : modeling and analysis

Kaluzny, J. & Krzeminski, W. 1993, MNRAS, 264, 785+

Kane, B. D., Clemens, D. P., & Myers, P. C. 1994, ApJ, 433, L49

Kaufmann, W. J. & Freedman, R. 1999, Universe (W. H. Freeman and Company, —c1999, 5th ed.)

Kennedy, D. C., Bates, B., & Kemp, S. N. 1996, A&A, 309, 109

Kraft, R. P., Sneden, C., Langer, G. E., Shetrone, M. D., & Bolte, M. 1995, AJ, 109, 2586+

Krauss, L. M. 2000, Phys. Rep., 333, 33

Lafler, J. & Kinman, T. D. 1965, ApJS, 11, 216+

Landolt, A. U. 1992, AJ, 104, 340

Leonard, P. J. T. & Linnell, A. P. 1992, AJ, 103, 1928

Livio, M. 1993, in ASP Conf. Ser. 53: Blue Stragglers, 3+

Mateo, M. 1993, in ASP Conf. Ser. 53: Blue Stragglers, 74+

Mateo, M. 1996, in ASP Conf. Ser. 90: The Origins, Evolution, and Destinies of Binary Stars in Clusters, 21+

Mateo, M., Harris, H. C., Nemec, J., & Olszewski, E. W. 1990, AJ, 100, 469

McVean, J. R., Milone, E. F., Mateo, M., & Yan, L. 1997, ApJ, 481, 782+

Monet, D. B. A., Canzian, B., Dahn, C., Guetter, H., Harris, H., Henden, A., Levine, S., Luginbuhl, C., Monet, A. K. B., Rhodes, A., Riepe, B., Sell, S., Stone, R., Vrba, F., & Walker, R. 1998, VizieR Online Data Catalog, 1252, 0+

Moreira, M. C., Yun, J. ., Torrelles, J. ., Afonso, J. ., & Santos, C. A. 1999, AJ, 118, 1315

Mould, J. 2000, Publications of the Astronomical Society of Australia, 17, 45

Nemec, J. M., Mateo, M., Burke, M., & Olszewski, E. W. 1995, AJ, 110, 1186+

Nemec, J. M., Nemec, A. F. L., & Lutz, T. E. 1994, AJ, 108, 222

Paczyński, B. 1996, preprint (astro-ph/9608094) (invited review talk at STScI)

Peat, D. W., Griffiths, W. K., & Morris, P. W. 2000, in The Galactic Halo : From Globular Cluster to Field Stars, 265+

Perryman, M. A. C. 2000, Reports of Progress in Physics, 63, 1209

Piotto, G. & Zoccali, M. 1999, A&A, 345, 485

Piotto, G., Zoccali, M., King, I. R., Djorgovski, S. G., Sosin, C., Rich, R. M., & Meylan, G. 1999, AJ, 118, 1727

Press, W. H., Teukolsky, S. A., Vetterling, W. T., & Flannery, B. P. 1992, Numerical recipes in C. The art of scientific computing (Cambridge: University Press, —c1992, 2nd ed.)

Reed, B. C., Hesser, J. E., & Shawl, S. J. 1988, PASP, 100, 545

Rodríguez, E. & López-González, M. J. 2000, A&A, 359, 597

Rodríguez, E., López-González, M. J., & López de Coca, P. 2000, A&AS, 144, 469

Rosenberg, A. 2000, PASP, 112, 575

Rosenberg, A., Aparicio, A., Saviane, I., & Piotto, G. 2000a, A&AS, 145, 451

Rosenberg, A., Piotto, G., Saviane, I., & Aparicio, A. 2000b, A&AS, 144, 5

Rubenstein, E. P. 1997, PASP, 109, 933+

Rucinski, S. 1995, PASP, 107, 648+

Rucinski, S. M. 1985, in NATO ASIC Proc. 150: Interacting Binaries, 13–49

Rucinski, S. M. 1994, PASP, 106, 462

—. 2000, AJ, 120, 319

—. 2001, AJ, 122, 1007

Sarajedini, A. 1993, in ASP Conf. Ser. 53: Blue Stragglers, 14+

Sarajedini, A., Chaboyer, B., & Demarque, P. 1997, PASP, 109, 1321

Sato, T., Richer, H. B., & Fahlman, G. G. 1989, AJ, 98, 1335

Schechter, P. L., Mateo, M., & Saha, A. 1993, PASP, 105, 1342

Schlegel, D. J., Finkbeiner, D. P., & Davis, M. 1998, ApJ, 500, 525+

Schwarzenberg-Czerny, A. 1989, MNRAS, 241, 153

Shu, F. H., Adams, F. C., & Lizano, S. 1987, ARA&A, 25, 23

Sills, A. & Bailyn, C. D. 1999, ApJ, 513, 428

Sills, A., Bailyn, C. D., Edmonds, P. D., & Gilliland, R. L. 2000, ApJ, 535, 298

Spitzer, L. 1978, Physical processes in the interstellar medium (New York Wiley-Interscience, 1978. 333 p.)

Stetson, P. B. 1996, PASP, 108, 851+

Tammann, G. A., Reindl, B., Thim, F., Saha, A., & Sandage, A. 2001, preprint (astro-ph/0112489)

Tonry, J. & Davis, M. 1979, AJ, 84, 1511

Vandenberg, D. A., Stetson, P. B., & Bolte, M. 1996, ARA&A, 34, 461

VandenBerg, D. A., Swenson, F. J., Rogers, F. J., Iglesias, C. A., & Alexander, D. R. 2000, ApJ, 532, 430

Vazquez-Semadeni, E., Ballesteros-Paredes, J., & Klessen, R. 2002, preprint (astro-ph/0206038)

von Braun, K. & Mateo, M. 2001, AJ, 121, 1522

—. 2002, AJ, 123, 279

von Braun, K., Mateo, M., Chiboucas, K., Athey, A., & Hurley-Keller, D. 2002, in preparation, 1, 1

von Braun, K., Mateo, M., & Yan, L. 1996, American Astronomical Society Meeting, 189, 71.12

Welch, D. L. & Stetson, P. B. 1993, AJ, 105, 1813

Yan, L. & Mateo, M. 1994, AJ, 108, 1810